

# UC Irvine

## UC Irvine Electronic Theses and Dissertations

### Title

The Diverse Roles of [4Fe-4S] Clusters in Nitrogenase Iron-Sulfur Cluster Assembly and Catalysis

### Permalink

<https://escholarship.org/uc/item/62s6790b>

### Author

Rettberg, Lee

### Publication Date

2020

### Copyright Information

This work is made available under the terms of a Creative Commons Attribution License, available at <https://creativecommons.org/licenses/by/4.0/>

Peer reviewed|Thesis/dissertation

UNIVERSITY OF CALIFORNIA,  
IRVINE

The Diverse Roles of [4Fe-4S] Clusters in Nitrogenase Iron-Sulfur Cluster Assembly and Catalysis

DISSERTATION

submitted in partial satisfaction of the requirements for the degree of

DOCTOR OF PHILOSOPHY

in Biological Sciences

by

Lee Alexander Rettberg

Dissertation Committee:  
Professor Markus W. Ribbe, Chair  
Associate Professor Yilin Hu  
Professor Celia W. Goulding

2020

Portions of Chapter 2 and 3 © 2018 Springer Nature Limited

Portions of Chapter 3 © 2020 Springer Nature Limited

Portions of Chapter 4 © 2019 Wiley-VCH Verlag GmbH & Co.

Portions of Chapter 5 © 2019 American Society for Microbiology

All other content © 2020 Lee Alexander Rettberg

## **DEDICATION**

*To my parents for their love and support.*

## TABLE OF CONTENTS

	Page
LIST OF FIGURES	ix
LIST OF TABLES	xi
LIST OF ABBREVIATIONS	xii
ACKNOWLEDGMENTS	xiv
VITA	xvi
ABSTRACT OF THE DISSERTATION	xx
CHAPTER 1: Introduction to Nitrogenase	1
1.1 Overview of Nitrogenase	2
1.2 Assembly of Nitrogenase Iron-Sulfur Clusters	5
1.2.1 Iron-Sulfur Cluster Overview	5
1.2.2 [Fe <sub>4</sub> S <sub>4</sub> ] Cluster Assembly	6
1.2.3 L-cluster Assembly	7
1.2.4 M-cluster Maturation and Delivery	9
1.3 NifB is a Unique Radical SAM Enzyme	10
1.4 Reductase Activities of NifH	13

1.5	Aims of Dissertation	15
1.5.1	Specific Aim 1: Characterization of the Iron-Sulfur Clusters of NifB	16
1.5.2	Specific Aim 2: Investigation of an Essential Nitrogen Ligand on NifB	16
1.5.3	Specific Aim 3: Structure of NifH from <i>Azotobacter vinelandii</i> in the All-Ferrous State	17
1.5.4	Specific Aim 4: Structure of NifH from <i>Methanosarcina acetivorans</i>	17
1.6	References	18
CHAPTER 2: Characterization of the Iron-Sulfur Clusters of NifB		26
2.1	Introduction	27
2.2	Materials and Methods	30
2.2.1	General Information	30
2.2.2	Cell Growth and Protein Purification	30
2.2.3	Cluster Reconstitution and Maturation	30
2.2.4	Iron Determination	32
2.2.5	Electron Paramagnetic Resonance (EPR) Analysis	32
2.2.6	SAM Cleavage Assay	33
2.2.7	Methanethiol Assay	33

2.3	Results and Discussion	34
2.3.1	Establishing the 4Fe Nature of Modules on NifB	34
2.3.2	Defining the Functions of NifB-associated [Fe <sub>4</sub> S <sub>4</sub> ] Modules	37
2.4	Summary and Conclusion	39
2.5	Acknowledgments	41
2.6	References	41
CHAPTER 3: Investigation of an Essential Nitrogen Ligand on NifB		44
3.1	Introduction	45
3.2	Materials and Methods	46
3.2.1	General Information	46
3.2.2	Cell Growth and Protein Purification	46
3.2.3	Iron-Sulfur Cluster Reconstitution	47
3.2.4	Iron Determination	48
3.2.5	M-Cluster Maturation Assay	49
3.2.6	SAM Cleavage Assay	49
3.2.7	Methanethiol Assay	50
3.2.8	Continuous-Wave Electron Paramagnetic Resonance (CW-EPR) Analysis	51

3.2.9	Pulse EPR Analysis	51
3.2.10	X-ray Absorption Spectroscopy (XAS) Analysis	53
3.3	Results and Discussion	55
3.3.1	Observation of N Coordination to the K1-Cluster	55
3.3.2	Identification of an Essential Nitrogen Ligand	58
3.3.3	Function of His <sup>43</sup> in L-Cluster Maturation	62
3.3.4	Roles of His <sup>43</sup> in Cluster Transformation	64
3.4	Summary and Conclusion	68
3.5	Acknowledgments	71
3.6	References	71
CHAPTER 4: Structure of NifH from <i>Azotobacter vinelandii</i> in an All-Ferrous State		75
4.1	Introduction	76
4.2	Materials and Methods	77
4.2.1	General Information	77
4.2.2	Protein Purification and Crystallization	77
4.2.3	Data Collection and Structure Determination	78
4.2.4	CO <sub>2</sub> Reduction Activity Analyses	79

4.2.5	Density Functional Theory (DFT) Calculations	80
4.3	Results and Discussion	82
4.3.1	The Structure of AvNifH in the All-Ferrous State	82
4.3.2	Mechanism of from CO <sub>2</sub> Activation from Density Functional Theory Calculations	87
4.4	Summary and Conclusion	89
4.5	Acknowledgments	91
4.6	References	91
CHAPTER 5: Structure of NifH from <i>Methanosarcina acetivorans</i>		95
5.1	Introduction	96
5.2	Materials and Methods	98
5.2.1	General Information	98
5.2.2	Protein Purification and Crystallization	99
5.2.3	Data Collection and Structure Determination	99
5.2.4	Mutant Strain Construction and Activity Analyses	100
5.2.5	EPR Spectroscopy Analyses	101
5.2.6	Density Functional Theory Calculations	101

5.3	Results and Discussion	102
5.3.1	Analysis of the Dithionite-Reduced <i>MaNifH</i> Structure	102
5.3.2	Modeling of Extra Electron Density in the Structure of the Dithionite-Reduced <i>MaNifH</i>	105
5.3.3	DFT Calculations of CO <sub>2</sub> Capture by Dithionite- Reduced <i>MaNifH</i>	105
5.3.4	Examining the Role of the Conserved Arg Pair of <i>MaNifH</i> in CO <sub>2</sub> Capture	107
5.3.5	Proposal of a Plausible Mechanism for the Initial Capture of CO <sub>2</sub> by <i>MaNifH</i>	108
5.4	Summary and Conclusion	110
5.5	Acknowledgments	112
5.6	References	112

## LIST OF FIGURES

	Page
Figure 1.1. Models of nitrogenase protein and metallocluster structures.	3
Figure 1.2. Iron-sulfur cluster assembly pathways catalyzed by Nif proteins.	7
Figure 1.3. Biosynthesis of L-cluster by NifB.	8
Figure 1.4. Maturation of L- to M-cluster.	9
Figure 1.5. Radical chemistry initiation by radical S-adenosylmethionine enzymes.	12
Figure 2.1. Assignment of three [Fe <sub>4</sub> S <sub>4</sub> ] cluster modules in <i>Ma</i> NifB.	36
Figure 2.2. Spectroscopic and functional properties of dual cluster <i>Ma</i> NifB variants.	38
Figure 3.1. Pulse EPR analysis of <i>Ma</i> NifB.	58
Figure 3.2. The primary sequence of <i>Ma</i> NifB.	59
Figure 3.3. Iron content and EPR spectra of dithionite-reduced <i>Ma</i> NifB proteins.	60
Figure 3.4. Three-pulse ESEEM spectra of dithionite reduced <i>Ma</i> NifB proteins.	61
Figure 3.5. Conversion of L-cluster to M-cluster on <i>Ma</i> NifB proteins.	63
Figure 3.6. Functional properties of <i>Ma</i> NifB proteins.	64
Figure 3.7. Fe K-edge XAS analysis of <i>Ma</i> NifB proteins.	67
Figure 4.1. CO <sub>2</sub> reduction by <i>Av</i> NifH.	82

Figure 4.2. Overall structure of AvNifH <sup>0</sup> and close-up view of the active site.	83
Figure 4.3. Structural comparison between AvNifH <sup>0</sup> and AvNifH <sup>1</sup> .	85
Figure 4.4. CO <sub>2</sub> capture and activation by NifH proteins.	87
Figure 4.5. Proposed mechanism of CO <sub>2</sub> activation by AvNifH <sup>0</sup> .	89
Figure 5.1. Structure of MaNiH and visualization of additional density.	103
Figure 5.2. Comparison of MaNifH crystal structure and DFT model.	107
Figure 5.3. Spectroscopic and catalytic features of the wild-type and variant MaNifH.	108
Figure 5.4. Model for CO <sub>2</sub> capture.	110

## LIST OF TABLES

	Page
Table 2.1. Iron content of wild-type <i>MaNifB</i> and single module variants.	37
Table 2.2. Iron content of double module variants.	38
Table 3.1. Best fits of the Fe K-edge EXAFS data.	68
Table 4.1. Data collection and refinement statistics for <i>AvNifH</i> <sup>0</sup> .	84
Table 5.1. Data collection and refinement statistics for <i>MaNifH</i> .	104

## LIST OF ABBREVIATIONS

5'-dAH	5'-deoxyadenosine
<i>Av</i>	<i>Azotobacter vinelandii</i>
C <sub>2</sub> H <sub>2</sub>	acetylene
C <sub>2</sub> H <sub>4</sub>	ethene
CO	carbon monoxide
CO <sub>2</sub>	carbon dioxide
Da	Dalton
DFT	density functional theory
DT	dithionite
E <sup>0'</sup>	standard electrode potential
e <sup>-</sup>	electron
EPR	electron paramagnetic resonance spectroscopy
ESEEM	electron spin echo envelope modulation
Eu <sup>II</sup> DTPA	europium(II) diethylenetriaminepentaacetate
EXAFS	Extended X-ray absorption fine structure
FeS	iron-sulfur
FFT	fast Fourier transform
FID	flame ionization detector
GC	gas chromatography
HPLC	high-performance liquid chromatography
HYSCORE	hyperfine sub-level correlation spectroscopy

IDS	5,5'-indigodisulfonic acid
<i>Ma</i>	<i>Methanosarcina acetivorans</i>
MS	mass spectrometry
MgATP	magnesium - adenosine triphosphate
OD <sub>λ</sub>	optical density at wavelength λ [nm]
PDB	Protein Data Bank
rpm	rotations per minute
RS	radical <i>S</i> -adenosyl-L-methionine
SAH	<i>S</i> -adenosyl-L-homocysteine
SAM	<i>S</i> -adenosyl-L-methionine
SDS-PAGE	sodium dodecyl sulfate polyacrylamide gel electrophoresis
Tris	tris-(hydroxymethyl)-aminomethane
UV/Vis	ultra violet and visible spectral regions of light
v/v	volume per volume
w/v	weight per volume
w/w	weight per weight
XAS	X-ray absorption spectroscopy

## ACKNOWLEDGMENTS

First, I would like to thank my advisor Markus Ribbe, and co-advisor, Yilin Hu, for the opportunities that they have provided for me. They welcomed me into their laboratories and provided me with several exciting projects. Their dedication to securing funding and disseminating research results made my research successes possible. Along the way, their vocal support led to me receiving awards for my work, for which I am incredibly grateful.

I am also grateful to Celia Goulding, who was another advocate for me, from the time that I rotated through her laboratory in my first year of graduate school, until the end, when she served on my dissertation committee.

My heartfelt thanks to the many students and staff members of the Ribbe and Hu laboratories that I worked with: Aaron Fay, Andrew Jasniewski, Caleb Hiller, Chi Chung Lee, Jared Wiig, Jasper Liedtke, Johannes Rebelein, Joseph Solomon, Kazuki Tanifuji, Martin Stiebritz, Matty Rasekh, Megan Newcomb, Nate Sickerman, and Wonchull Kang. They taught me many valuable lessons and provided needed encouragement.

My cohort was also an immeasurably helpful resource for information and emotional support as we navigated the graduate school system together. Before coming to UCI, I significantly benefited from the guidance of my scientific mentors, including Grant Jensen, Yi-Wei Chang, Scott Stagg, Suzanne Young, and others, for which I am deeply appreciative.

My dissertation research was made possible by generous financial support in the form of a National Science Foundation CAREER grant, award number CHE-1651398 to Dr. Yilin Hu, and by the National Institutes of Health – National Institute of General Medical Sciences under award

number GM67626 to Markus W. Ribbe and Yilin Hu. Additional thanks to Nature Publishing Group, Wiley-VCH Verlag GmbH & Co., and the American Society for Microbiology for publishing the results of my research and for giving me permission to reuse portions of those published works in my dissertation.

Finally, thank you to my family. I owe all my success to my wonderful parents, Elaine and Thomas. They have been part of every critical moment of my life. I must also recognize my siblings and extended family for their important influences on me and their support over the years. Having my sister Brianna nearby during my graduate studies helped to keep me grounded. I love you all.

## VITA

Lee Alexander Rettberg

### EDUCATION

---

**University of California, Irvine**

Ph.D. in Biological Sciences

2020

**University of Texas at Austin**

B.S. in Biochemistry

2012

### RESEARCH EXPERIENCE

---

**University of California, Irvine, Irvine, CA**

2015 – 2020

Graduate Research Assistant

*Advisors: Markus Ribbe, Ph.D. & Yilin Hu, Ph.D.*

Mechanisms of nitrogenase cofactor biosynthesis proteins

- Identified key amino acids of NifB protein that are essential for maturation of nitrogenase L-cluster
- Determined mechanistic steps cofactor maturation on NifB protein by complementary biochemical, structural, and spectroscopic techniques

Structural basis of CO<sub>2</sub> reduction by nitrogenase NifH protein

- Determined structures of nitrogenase NifH proteins by X-ray crystallography to examine structural determinants of its ability to reduce CO<sub>2</sub> to CO and hydrocarbons

**Howard Hughes Medical Institute, Pasadena, CA**

2013 – 2015

Research Technician

*Laboratory of Grant Jensen, Ph.D.*

Revealing *in vivo* structures of bacterial secretion systems and pili by whole-cell electron cryo-tomography and subtomogram averaging.

- Prepared samples of various bacterial species for imaging, processed micrographs into tomograms, picked particles and generated subtomogram averages of protein assemblies
- Analyzed symmetry and heterogeneity of protein complexes in their native context

Characterizing the self-assembly of COPII coat proteins

- Expressed proteins in *E. coli* and baculovirus-infected insect cells.
- Purified and characterized proteins through negative-stain EM and dynamic light scattering.

## PUBLICATIONS

---

15. **Rettberg LA**, Wilcoxon J, Jasniewski AJ, Lee CC, Tanifuji K, Hu Y, Britt RD, Ribbe MW. 2020. Identity and function of an essential nitrogen ligand of the nitrogenase cofactor biosynthesis protein NifB. *Nature Communications* **11**:1757.
14. Rupnik K, Tanifuji K, **Rettberg LA**, Ribbe MW, Hu Y, Hales BJ. 2020. Electron Paramagnetic Resonance and Magnetic Circular Dichroism Spectra of the Nitrogenase M Cluster Precursor Suggest Sulfur Migration upon Oxidation: A Proposal for Substrate and Inhibitor Binding. *ChemBioChem* **21**:1-7.
13. **Rettberg LA**, Kang W, Stiebritz MT, Hiller CJ, Lee CC, Liedtke J, Ribbe MW, Hu Y. 2019. Structural Analysis of a Nitrogenase Iron Protein from *Methanosarcina acetivorans*: Implications for CO<sub>2</sub> Capture by a Surface-Exposed [Fe<sub>4</sub>S<sub>4</sub>] Cluster. *mBio* **10**:e01497-19.
12. **Rettberg LA**, Stiebritz MT, Kang W, Lee CC, Ribbe MW, Hu Y. 2019. Structural and Mechanistic Insights into CO<sub>2</sub> Activation by Nitrogenase Iron Protein. *Chemistry – A European Journal* **25**:13078–13082.
11. Hiller CJ, Lee CC, Stiebritz MT, **Rettberg LA**, Hu Y. 2019. Strategies Towards Capturing Nitrogenase Substrates and Intermediates via Controlled Alteration of Electron Fluxes. *Chemistry – A European Journal* **25**:2389-2395.
10. **Rettberg LA**, Wilcoxon J, Lee CC, Stiebritz MT, Tanifuji K, Britt RD, Hu Y. 2018. Probing the coordination and function of Fe<sub>4</sub>S<sub>4</sub> modules in nitrogenase assembly protein NifB. *Nature Communications* **9**:2824.
9. Chang YW, Shaffer CL, **Rettberg LA**, Ghosal D, Jensen GJ. 2018. *In Vivo* Structures of the *Helicobacter pylori* cag Type IV Secretion System. *Cell Reports* **23**:673–681.
8. Hiller CJ, **Rettberg LA**, Lee CC, Stiebritz MT, Hu Y. 2019. Current Understanding of the Biosynthesis of the Unique Nitrogenase Cofactor Core, p. 15–31. *In* Ribbe, MW (ed.), *Metallocofactors that Activate Small Molecules: With Focus on Bioinorganic Chemistry*. Springer International Publishing, Cham.

7. **Rettberg LA**, Tanifuji K, Jasniewski A, Ribbe MW, Hu Y. 2018. Radical S-Adenosyl-L-Methionine (SAM) Enzyme Involved in the Maturation of the Nitrogenase Cluster, p. 341–361. *In Bandarian, V (ed.), Methods in Enzymology*. Academic Press.
6. Sickerman NS, **Rettberg LA**, Hu Y, Ribbe MW. 2017. Assembly of Nitrogenase FeMoco and P Cluster. *Encyclopedia of Inorganic and Bioinorganic Chemistry*, **61**:271-279.
5. Sickerman NS, **Rettberg LA**, Hu Y, Ribbe MW. 2017. Nitrogenase Metallocluster Assembly, p. 75-86. *In Johnson, MK, Scott, RA (eds.), Metalloprotein Active Site Assembly*. John Wiley & Sons.
4. Chang YW, **Rettberg LA**, Ortega DR, Jensen GJ. 2017. *In vivo* structures of an intact type VI secretion system revealed by electron cryotomography. *EMBO Reports* **18**:1090–1099.
3. Sickerman NS, **Rettberg LA**, Lee CC, Hu Y, Ribbe MW. 2017. Cluster assembly in nitrogenase. *Essays Biochem* **61**:271–279.
2. Chang YW, Kjær A, Ortega DR, Kovacikova G, Sutherland JA, **Rettberg LA**, Taylor RK, Jensen GJ. 2017. Architecture of the *Vibrio cholerae* toxin-coregulated pilus machine revealed by electron cryotomography. *Nature Microbiology* **2**:16269.
1. Chang YW, **Rettberg LA**, Treuner-Lange A, Iwasa J, Søggaard-Andersen L, Jensen GJ. 2016. Architecture of the type IVa pilus machine. *Science* **351**:aad2001.

## AWARDS

---

Howard A. Schneiderman Fellowship Award <i>UCI School of Biological Sciences</i>	2020
Krishna and Sujata Tewari Scholar Award <i>UCI School of Biological Sciences</i>	2019
Robert Warner Award for Outstanding Achievement in Nucleic Acid Biochemistry <i>UCI School of Biological Sciences</i>	2019

## SERVICE

---

Science Saturdays, Irvine, CA Co-founder and Organizer	2016 – 2020
<ul style="list-style-type: none"> <li>▪ Organized science and engineering laboratory tours and demonstrations for over 400 students across ten event dates</li> <li>▪ Arranged for food and transportation of students from Julia Lathrop Intermediate School and Carr Intermediate School in Santa Ana, CA to UCI main campus</li> </ul>	

**Dept. of Molecular Biology & Biochemistry, UCI, Irvine, CA**  
Student Research in Progress Seminar Organizer

2018

- Emailed department members regarding speaker schedule, introduced speakers and ordered food for talks

**Tech Trek, Irvine, CA**

Summer 2016 & 2017

Volunteer

- Introduced my research and led hands-on science demonstrations to middle-school-aged summer camp attendees

## **TEACHING**

---

**University of California, Irvine, Irvine, CA**

2017 – 2020

Graduate Teaching Assistant

- Courses: Microbiology (M 122), Microbiology Laboratory (M 188L), Biochemistry (Bio 98) Biochemistry Laboratory (M 114L)
- Led discussion groups and test reviews; ran laboratory sections; graded tests and reports

**University of Texas at Austin, Austin, TX**

Fall 2010

UTeach student instructor

- Designed and taught weekly one-hour STEM lessons to students at their middle school

## ABSTRACT OF THE DISSERTATION

The Diverse Roles of [4Fe-4S] Clusters in Nitrogenase Iron-Sulfur Cluster Assembly and Catalysis

By

Lee Alexander Rettberg

Doctor of Philosophy in Biological Sciences

University of California, Irvine, 2020

Professor Markus Walter Ribbe, Chair

Nitrogenase catalyzes the enzymatic reduction of dinitrogen ( $N_2$ ) into ammonia ( $NH_3$ ) at ambient temperatures and pressures.  $N_2$  reduction by molybdenum (Mo) nitrogenase requires the catalytic molybdenum-iron protein (NifDK) and its reductase, the iron protein (NifH). In addition to its role in  $N_2$  reduction, NifH proteins can independently reduce carbon dioxide ( $CO_2$ ) to carbon monoxide (CO) and short-chain hydrocarbons. Nitrogenase proteins contain iron-sulfur cluster cofactors that are crucial to these activities. NifH uses a  $[Fe_4S_4]$  cluster for transferring electrons to NifDK and for independently reducing  $C_1$ , whereas the site of  $N_2$  reduction on NifDK is the complex  $[MoFe_7S_9C\text{-homocitrate}]$  M-cluster. M-cluster, however, is synthesized ex-situ by other proteins from  $[Fe_4S_4]$  cluster precursors. The radical S-adenosylmethionine enzyme NifB uses  $[Fe_4S_4]$  cluster units for the biosynthesis of the  $[Fe_8S_9C]$  L-cluster, the immediate precursor to M-cluster. NifH and NifB rely on  $[Fe_4S_4]$  clusters to perform very different functions, mediated by their protein environments in ways that aren't well understood. The focus of this dissertation is on how the distinct protein environments of NifH and NifB proteins modulate the reactivity of their  $[Fe_4S_4]$  clusters.

Three  $[\text{Fe}_4\text{S}_4]$  cluster modules, and their amino acid ligands, were identified on NifB by spectroscopic and biochemical characterization of mutant proteins. Interestingly, a histidine residue that serves as a transient nitrogen ligand to a  $[\text{Fe}_4\text{S}_4]$  precursor cluster was crucial for L-cluster assembly. Mutation of this ligand was found to interfere with the structural transformations of iron-sulfur clusters of NifB.

To understand how the  $[\text{Fe}_4\text{S}_4]$  cluster at the active site of NifH catalyzes  $\text{C}_1$  substrate reductions, I solved the structures of two NifH proteins by X-ray crystallography. The first was NifH in the all-ferrous  $[\text{Fe}_4\text{S}_4]^0$  state from *Azotobacter vinelandii* (AvNifH). This form, produced by treating the protein with a strong reductant, is the most active in substrate reduction. The structure solved from a crystal in this form revealed two arginine residues that have an asymmetric arrangement that can serve to capture and protonate substrates. Another NifH protein, *Methanosarcina acetivorans* (MaNifH), can reduce  $\text{CO}_2$  and CO to short-chain hydrocarbons. MaNifH in the  $[\text{Fe}_4\text{S}_4]^{1+}$  state, produced by the presence of dithionite, demonstrates a similar asymmetric arrangement of a pair of arginines. These crystallization solution also contained bicarbonate, an alternative  $\text{CO}_2$  source. Excitingly, additional density, potentially a captured substrate, was observed near the  $[\text{Fe}_4\text{S}_4]$  cluster. These structures provided parameters for density functional theory (DFT) calculations provided details that enabled propose mechanisms for  $\text{CO}_2$  and CO reduction by  $[\text{Fe}_4\text{S}_4]$  clusters.

Together, these results contribute towards building a mechanistic model of a novel  $[\text{Fe}_4\text{S}_4]$ -based system for converting greenhouse gases into hydrocarbon fuels, and for understanding how  $[\text{Fe}_4\text{S}_4]$  clusters are used to synthesize more complex metallocofactors.

## **Chapter 1: Introduction to Nitrogenase**

## 1.1 Overview of Nitrogenase

Nitrogenase is an enzyme that catalyzes the reduction of dinitrogen ( $N_2$ ) into ammonia ( $NH_3$ ); this reduced form of nitrogen can then be incorporated into various biomolecules. Nitrogenase is found in diazotrophic bacteria and archaea and is a critical part of the global nitrogen cycle (1). Diazotrophs reduce  $N_2$  by nitrogenase under ambient conditions. In contrast, the industrial Haber-Bosch process requires high temperatures and pressures, and consumes large amounts of energy from fossil fuels, to carry out the same reduction. The advantages of the enzymatic system motivates research into how nitrogenase proteins perform this challenging reaction.

The best-characterized nitrogenase system is the molybdenum-dependent Mo-nitrogenase from the free-living soil bacterium, *Azotobacter vinelandii* (*Av*). Mo-nitrogenase requires two protein components: the molybdenum- and iron-containing MoFe protein (also called NifDK), and the iron-containing Fe protein (also called NifH)(2).  $N_2$  reduction also requires a reductant, MgATP, and strictly anaerobic conditions to occur in vitro. Our current understanding of nitrogenase, as outlined in this chapter, is built on decades of biochemical, spectroscopic, genetic, and structural studies of this system (3, 4).

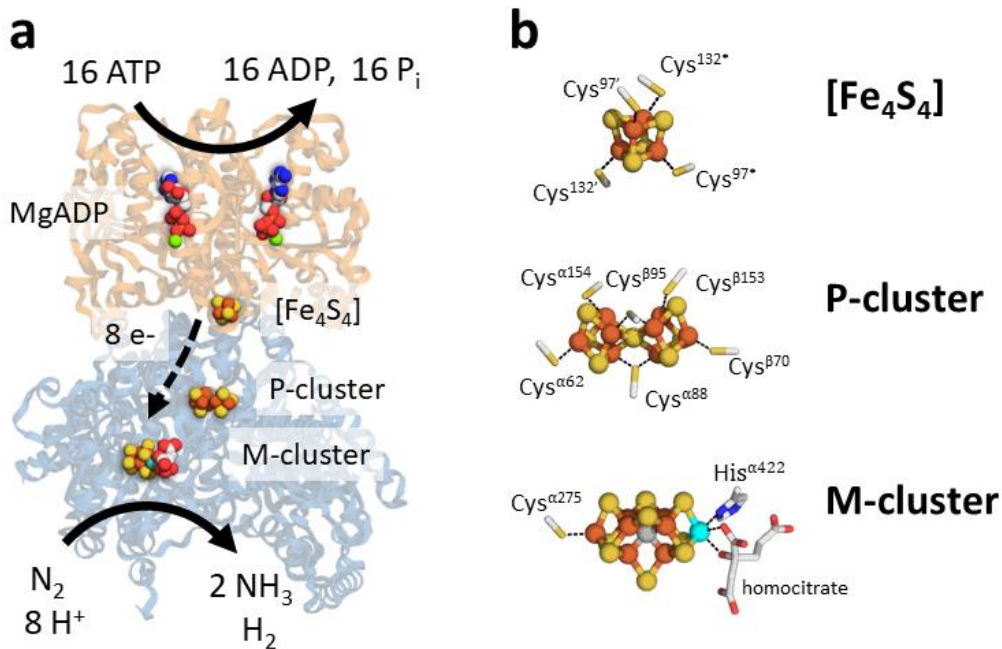
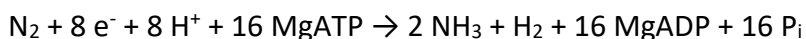


**Figure 1.1 Models of nitrogenase protein and metallocluster structures.** **a** Ribbons of NifH shown as orange ribbons; one  $\alpha\beta$  half of NifDK is depicted as blue ribbons. Electron transfer between clusters indicated by the dashed arrow. **b**  $[\text{Fe}_4\text{S}_4]$  (top), P-cluster (center), and M-cluster (bottom) models with amino acid ligands labeled. Atoms are colored as follows: Fe, rust; S, gold; Mo, cyan; C, light gray; O, red; N, blue; Mg, green. Created from the structure of the NifH-NifDK complex with MgADP bound; PDB 2AF1 (5).

Nitrogenase proteins contain complex metallocofactors that are key to their functions. In Mo-nitrogenase,  $\text{N}_2$  reduction occurs at a  $[\text{MoFe}_7\text{S}_9\text{C}-(R\text{-homocitrate})]$  M-cluster within the  $\alpha_2\beta_2$  heterotetrameric NifDK protein (*nifD* and *nifK* gene products) (Fig. 1.1 a) (6–8).  $\text{His}^{\alpha 443}$  and  $\text{Cys}^{\alpha 275}$  ligate M-cluster within the  $\alpha$  subunits of NifDK, 10 Å from the protein surface. The structure of M-cluster is of  $[\text{Mo-Fe}_3\text{S}_3]$  and  $[\text{Fe}_4\text{S}_4]$  sub-cubanes bridged by three  $\mu_2$  sulfides and a  $\mu_6$  central carbide (Fig. 1.1 b, bottom)(6, 9, 10). NifDK also contains two  $[\text{Fe}_7\text{S}_9]$  P-clusters that shuttle electrons to M-cluster. The arrangement of P-clusters is two  $[\text{Fe}_4\text{S}_4]$  cubanes with a bridging  $\mu_6$ -sulfide and six coordinating cysteine residues at the  $\alpha/\beta$  interfaces (Fig. 1.1 b, center)(6, 8). The reductase for NifDK is NifH: a homodimer of *nifH* gene products that has a MgATP binding site within each subunit and a  $[\text{Fe}_4\text{S}_4]$  cubane cluster at the subunit interface (Fig. 1.1 b, top) (11).

During N<sub>2</sub> reduction, NifH containing two MgATP molecules and a reduced [Fe<sub>4</sub>S<sub>4</sub>] cluster binds to NifDK (Fig. 1.1 a) (5, 7, 12, 13). Subsequently, the [Fe<sub>4</sub>S<sub>4</sub>] cluster of NifH transfers an electron to a P-cluster of NifDK (14). The two MgATP molecules on NifH are hydrolyzed to two MgADP and two inorganic phosphates (P<sub>i</sub>), causing conformational changes of NifH, which result in its dissociation from NifDK (15, 16). P-cluster transfers electrons to M-cluster, the site of substrate reduction. This electron transfer cycle is repeated eight times for reduction of N<sub>2</sub> to NH<sub>3</sub>, and obligate H<sub>2</sub> production, according to the scheme (4, 7):



The central feature of nitrogenase that underlies this reaction is the M-cluster, one of the most complex metallocofactors found in Nature (17, 18). M-cluster is assembled ex-situ by several additional nif (nitrogen fixation)-proteins before being delivered to NifDK. One of these cofactor biosynthesis proteins, NifB, is responsible for supplying perhaps the most interesting features of M-cluster, the interstitial carbide. Insertion of the interstitial carbide, a μ<sub>6</sub>-coordinated carbon within the cluster, occurs via a novel radical S-adenosylmethionine (SAM)-dependent mechanism on NifB (19, 20). This process fuses two [Fe<sub>4</sub>S<sub>4</sub>] clusters, with the concomitant insertion of the carbide and a 9<sup>th</sup> sulfur atom, to form the [Fe<sub>8</sub>S<sub>9</sub>C] L-cluster (20, 21). Other proteins further mature L-cluster into M-cluster (22). A better understanding of nitrogenase M-cluster biosynthesis could lead to more efficient NH<sub>3</sub> production by informing the design of a better industrial catalyst or revealing how functional nitrogenase genes can be incorporated into crop plants.

M-cluster is not the only nitrogenase FeS cluster that can directly reduce substrates. The [Fe<sub>4</sub>S<sub>4</sub>] cluster of NifH can also independently interconvert CO<sub>2</sub> and CO (23). Some NifH proteins can also reduce CO and perform C-C coupling to produce small hydrocarbons (23, 24). CO<sub>2</sub> and CO activation by NifH resembles the activity of carbon monoxide dehydrogenase (CODH) enzymes, however, NifH and its heterometallic iron-sulfur cofactor do not resemble characterized CODH proteins. This implies that NifH has a novel mechanism for C<sub>1</sub> substrate activation that is not well-understood. Unraveling this mechanism could lead to exciting new technologies for carbon capture and fossil fuels synthesis.

Clearly, [Fe<sub>4</sub>S<sub>4</sub>] clusters on NifB and NifH proteins have multiple important functions that demand further investigation. The following sections will review the current understanding of the role of [Fe<sub>4</sub>S<sub>4</sub>] clusters on NifB and NifH.

## **1.2 Assembly of Nitrogenase Iron-Sulfur Clusters**

### **1.2.1 Iron-Sulfur Cluster Overview**

Iron-sulfur clusters, consisting of one or more iron ions bridged by sulfides (S<sup>2-</sup>), are among the most common cofactors found in proteins (18, 25). Simple [Fe<sub>2</sub>S<sub>2</sub>], [Fe<sub>3</sub>S<sub>4</sub>], and [Fe<sub>4</sub>S<sub>4</sub>] clusters are ubiquitous across all domains in life. Some enzymes also use more specialized and complex iron-sulfur cofactors: including the H-clusters of [FeFe] hydrogenases, the C-cluster of Ni,Fe-carbon monoxide dehydrogenase (CODH), and P-cluster and M-cluster of nitrogenase (17). The diversity of cluster compositions and the protein scaffolds that hold them allow for the tuning of the cluster reduction potentials to span a wide range, from roughly -700 mV to +500 mV,

making them especially useful for electron transfer reactions (26–28). FeS clusters are also used by enzymes for substrate binding, catalyzing substrate dehydrogenations and transformations, redox sensing, iron and sulfide storage, and regulation of gene expression (18, 29–33).

Nitrogenase proteins use various types of FeS clusters to carry out many of the functions just mentioned.

### 1.2.2 [Fe<sub>4</sub>S<sub>4</sub>] Cluster Assembly

All organisms have at least one system for assembling the [Fe<sub>2</sub>S<sub>2</sub>] and [Fe<sub>4</sub>S<sub>4</sub>] clusters found as cofactors in enzymes (33). The synthesis of small FeS clusters for nitrogenase proteins is carried out by a dedicated system consisting of NifU and NifS (Fig. 1.2). Bacterial strains with *nifU* or *nifS* genes knocked out results in strains that have a much lower diazotrophic growth rate (34, 35). NifU serves as a scaffold for assembling [Fe<sub>2</sub>S<sub>2</sub>] and [Fe<sub>4</sub>S<sub>4</sub>] clusters from iron and sulfur mobilized by the cysteine desulfurase NifS (36–39). [Fe<sub>4</sub>S<sub>4</sub>] clusters assembled on NifU can then be transferred to NifH and NifB proteins (Fig. 1.2) (40).

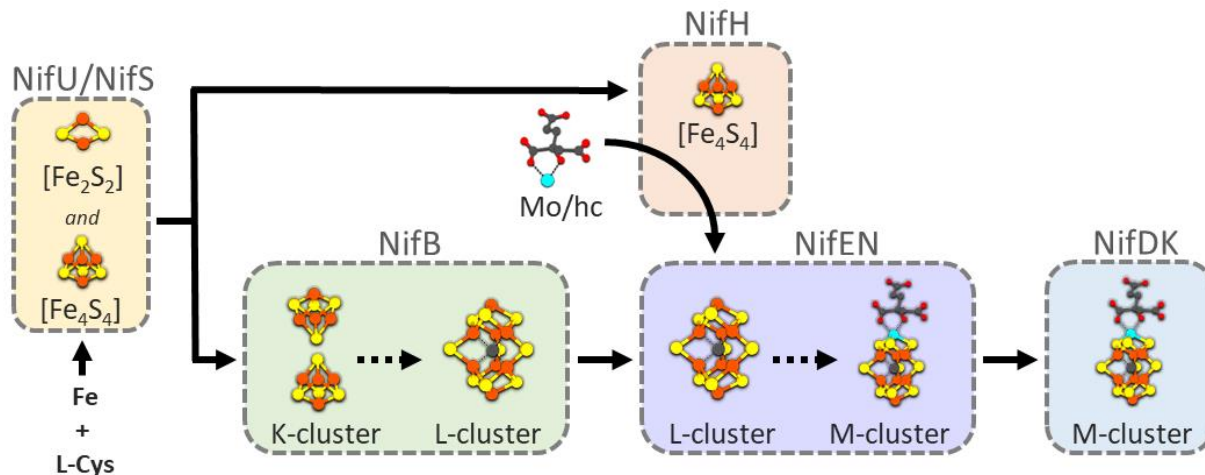


**Figure 1.2 Iron-sulfur cluster assembly pathways catalyzed by Nif proteins.** Schematic representation of Nif proteins and FeS clusters that are transformed. Solid lines represent a transfer of clusters between proteins, and dashed lines represent cluster transformations within a protein. Atoms of clusters are colored as follows: Fe, rust; S, gold; Mo, cyan; C, light gray; O, red.

NifH contains a single [Fe<sub>4</sub>S<sub>4</sub>] cluster supplied by NifU. NifH isolated from NifU/NifS knockout strains lack the cluster, but it can be reconstituted in vitro in a reaction containing NifU, NifS, iron, and cysteine(37).

NifU can also provide the three [Fe<sub>4</sub>S<sub>4</sub>] clusters that are thought to reside on NifB (21, 41). Two of them collectively termed the K-cluster, become fused into the L-cluster shown in Fig 1.2. The third [Fe<sub>4</sub>S<sub>4</sub>] cluster, called the SAM-cluster, binds to and reductively cleaves S-adenosylmethionine to effect K- to L-cluster conversion.

### 1.2.3 L-cluster Assembly

NifB transforms the two putative [Fe<sub>4</sub>S<sub>4</sub>] units of the K-cluster into the [Fe<sub>8</sub>S<sub>9</sub>C] L-cluster.

Forming this all-iron precursor to M-cluster on NifB requires two equivalents of SAM to generate the interstitial carbide (Fig. 1.3) (20). The role of the carbide is unknown but has been

proposed to stabilize M-cluster during catalysis (9, 10, 42, 43). The first step of cluster transformation on NifB is the transfer of a methyl group from SAM (*S*-adenosyl methionine) to a bridging sulfide of the K-cluster (Fig. 1.3, (1)) (20, 44). Then, a second SAM molecule, bound to the SAM-cluster of NifB, undergoes reductive homolytic cleavage that produces methionine and a 5'-deoxyadenosyl radical (5'-dA•) (Fig. 1.3, (2)) (20). 5'-dA• abstracts a hydrogen atom from the cluster-bound methyl group, creating a methylene radical. The subsequent loss of two more protons by an unknown process (Fig. 1.3, (3)) and cluster rearrangements result in an 8Fe core containing an interstitial carbide with a  $\mu_6$  coordination called the L\* cluster (21). Incorporation of a ninth sulfur atom, supplied *in vitro* in the form of sulfite ( $\text{SO}_3^{2-}$ ), (Fig. 1.3, (4)) in the presence of a reductant, completes L-cluster formation. L\* and L-cluster are nearly indistinguishable by EPR and EXAFS spectroscopies, indicating a similar structure and electronic properties (21, 45).

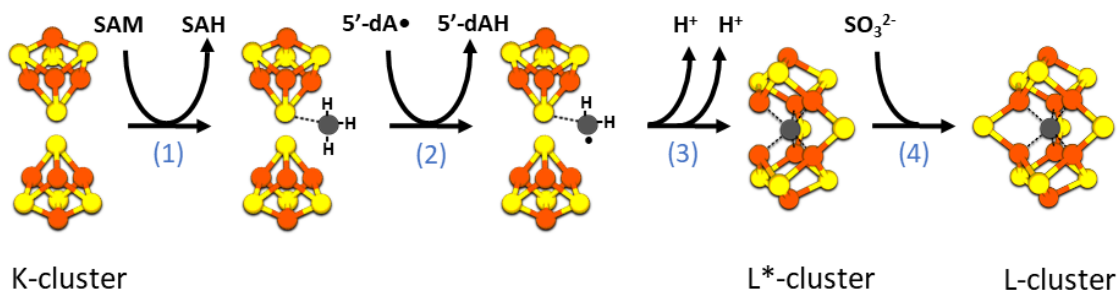


**Figure 1.3 Biosynthesis of L-cluster by NifB.** Proposed pathway for K- to L-cluster conversion. 1) First, a methyl group is transferred from SAM to a sulfide of the K-cluster; 2) then 5'-dA• radical produced from another equivalent of SAM abstracts a hydrogen from the cluster-bound methyl; 3) cluster rearrangement and loss of remaining hydrogen atoms generate L\*-cluster; 4) sulfite provides the final sulfur required to form L-cluster. Atom colors are Fe, rust; S, gold; Mo, cyan; C, dark gray.

### 1.2.4 M-cluster Maturation and Delivery

NifB then transfers L-cluster to NifEN (Fig. 1.2) (19). NifEN is an  $\alpha_2\beta_2$  heterotetramer that is homologous to NifDK (46). NifEN works in concert with NifH, acting in its capacity as a Mo/homocitrate insertase, to convert the iron-only precursor to the matured form of M-cluster (Fig. 1.4) (47–50). NifH binds to NifEN in a similar mode as NifH binds to NifDK during catalysis. (5, 13, 51) NifEN isolated from a  $\Delta nifHDK$  strain accumulates L-cluster on the surface of the protein that can be matured to M-cluster in vitro (47, 48, 52). The M-cluster resembles L-cluster that has had one terminal Fe replaced with Mo that is coordinated by (R)-homocitrate (Fig. 1.4) (6, 8, 49).

M-cluster is then delivered from NifEN to apoNifDK (NifDK protein containing two P-clusters but no M-clusters) to generate the active holoenzyme (3). M-cluster deficient NifDK can be isolated from  $\Delta nifB$  knockout strains (53). NifDK has a positively charged insertion funnel that the cofactor traverses to get to its binding site, and bulky amino acids sterically enclose it (54, 55). M-cluster binds within the alpha subunit of the protein, where the thiolate of Cys<sup>α275</sup> thiolate ligates to the terminal Fe and the imidazole group of His<sup>α442</sup> ligates to Mo (6, 8). The fully active form of NifDK contains two P-clusters and two M-clusters.

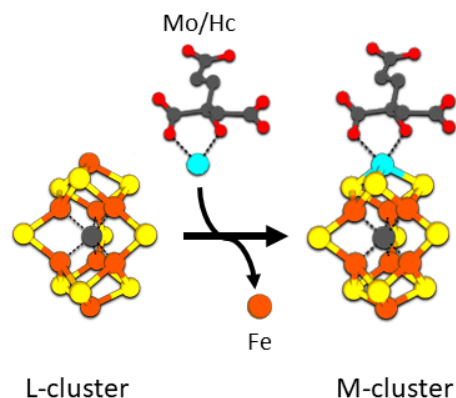


**Figure 1.4 Maturation of L- to M-cluster.** NifEN and NifH work together to convert the 8 Fe core of L-cluster into the heterometallic M-cluster by incorporation of Mo and homocitrate. Atom colors are Fe, rust; S, gold; Mo, cyan; C, dark gray.

### 1.3 NifB is a Unique Radical SAM Enzyme

NifB is a member of the large and functionally diverse radical S-adenosylmethionine (RS) enzyme superfamily (56). NifB is unique among RS enzymes for its role in inserting a carbide into an iron-sulfur cluster, even so, comparison to other RS enzymes can be useful for identifying mechanistic similarities. Proteins in this family use SAM to initiate a wide array of radical initiated reactions, including glyceryl radical formation, antibiotic biosynthesis, post-translational modification, rRNA/tRNA modifications, and cofactor biosynthesis (57). Starting in 1970, researchers began finding enzymes that required iron(II), SAM, a reductant, and strictly anaerobic reaction conditions for activity (58–65). Some of these systems, including pyruvate-formate lyase (PFL)/PFL activating enzyme (PFL-AE), anaerobic ribonucleotide reductase (aRNR)/aRNR activating enzyme, and lysine 2,3-aminomutase (LAM), were associated with the formation of catalytically important organic radicals that could be observed by EPR (61, 62, 66–68). Comparisons of the sequences of several of these proteins found that they shared a CXXXCXXC motif, recognized as a potential metal cofactor binding site (69). In combination, these results hinted that an iron-sulfur cluster ligated by a conserved motif was involved in organic radical formation. The similarity between SAM and the catalytic 5'-dA radical formed by coenzyme B<sub>12</sub> (adenosylcobalamin) dependent enzymes, which catalyze bond rearrangements via substrate H-atom abstraction by the 5'-dA radical, did not escape the notice of researchers (59). Moss and Frey used tritium labeled SAM to demonstrate that the 5' position of the adenosyl moiety is involved in hydrogen transfer in the substrate of LAM. These results provided strong evidence for substrate H-atom abstraction by a 5'-dA radical generated from SAM. Finally, the same group used an allylically stabilized SAM analog, anSAM, to observe the

formation of a radical on anSAM under turnover conditions (70). A bioinformatic analysis by Sofia and colleagues in 2001 formally united these enzymes as members of the radical SAM (RS) superfamily (56). This seminal study identified the defining CXXXCXXC motif, and NifB was later experimentally confirmed to use an FeS cluster for cleavage of SAM (19, 20).

Crystal structures of RS enzymes have a full  $(\beta\alpha)_8$  or partial  $(\beta\alpha)_6$  (71) TIM barrel protein fold. This fold consists of alternative beta strands that form a barrel, where the FeS cluster and substrates bind, and alpha helices that surround the exterior of the barrel. The conserved CXXXCXXC motif binds to three irons of a  $[\text{Fe}_4\text{S}_4]$  cluster, and the remaining site-differentiated iron has an open coordination site that can form a chelate with the carboxyl and amino moieties of SAM (Fig. 1.5, left) (71). The cluster is reduced from the 2+ resting state to the catalytically active 1+ state (67) when treated with a reductant, such as dithionite ( $\text{S}_2\text{O}_4^{2-}$ ) in vitro or flavodoxin in vivo (72). One-electron reduction of SAM causes homolytic cleavage of the S-5'C bond, generating a 5'-deoxyadenosyl radical and methionine (Fig. 1.5, center). Then, 5'-dA typically abstracts hydrogen from an unactivated C-H bond to form a substrate radical (Fig. 1.5, right). This reactive substrate radical can then initiate diverse reactions that are under the control of the protein matrix. The 5'-deoxyadenosyl radical has only recently been observed experimentally (73, 74). The structure of NifB has not been determined, but it is assumed to have the same TIM barrel fold that houses the SAM cluster and to initiate radical chemistry by a similar mechanism.

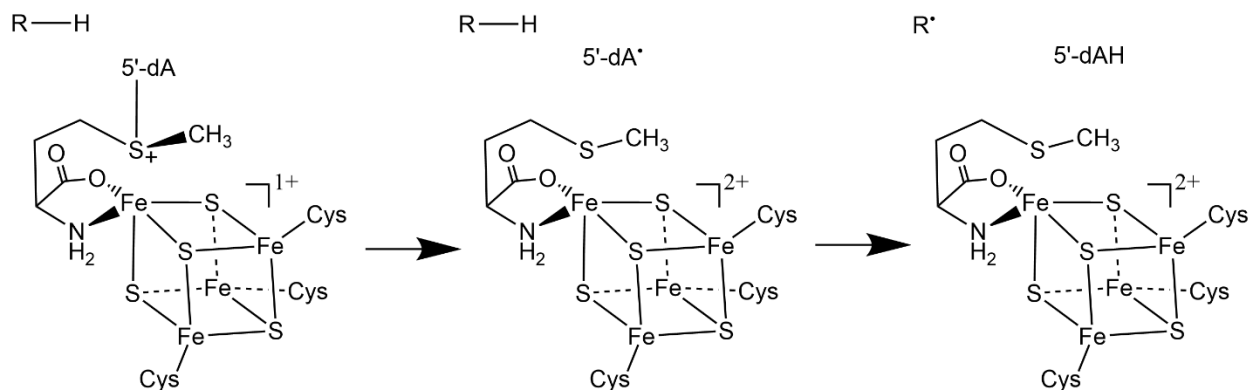


**Figure 1.5 Radical chemistry initiation by radical S-adenosylmethionine enzymes.** S-adenosyl methionine binds to the unique iron of the  $[\text{Fe}_4\text{S}_4]$  cluster. Electron transfer from  $[\text{Fe}_4\text{S}_4]^{1+}$  cluster to SAM triggers reductive homolytic cleavage. The resulting 5'-deoxyadenosyl radical abstracts a hydrogen from the substrate (depicted as R-H) to create a substrate radical. 5'-deoxyadenosyl is abbreviated as 5'-dA.

NifB is part of a subset of RS enzymes that have additional domains that contain auxiliary iron-sulfur clusters (75, 76). Auxiliary clusters can bind substrates or serve as a source of sulfur that is insertion into unactivated C-H bonds (75–78). NifB is most functionally similar to RS-dependent methyltransferases and methylthiotransferases. These enzymes are a subset of enzymes that use SAM both as a methyl donor and a radical generator (81). In RS-dependent methyltransferases, one SAM molecule transfers a methyl group ( $-\text{CH}_3$ ) to a methyl carrier in a polar nucleophilic substitution  $\text{S}_{\text{N}}2$  reaction. A second SAM molecule undergoes homolytic cleavage to create the 5'-dA radical, which abstracts a hydrogen from the transferred methyl to create a methylene radical that attacks a substrate carbon. Bond rearrangements result in a methylated product. The methyl transfer to a carrier, followed by radical dependent transfer to a substrate, has been described as a ping-pong mechanism (82).

RS methylthiotransferases catalyze the attachment of a methylthio group ( $-\text{SCH}_3$ ) to a substrate in a similar manner, except the initial polar methyl transfer is not to a cysteine thiol but a persulfide or cluster-bound bridging sulfide. This cluster is sacrificed during the reaction. The

subsequently generated substrate radical forms a new C-S bond, giving a new thioether group on the product (83). The mechanism of NifB is distinctive because methylated  $[\text{Fe}_4\text{S}_4]$  cluster is the target of the radical attack, and the product, a FeS cluster with an interstitial carbide, is not found in any other enzyme.

#### 1.4 Reductase Activities of NifH

NifH is a multifunctional reductase. Best known as the obligate electron donor for  $\text{N}_2$  reduction by NifDK, NifH also has roles in the maturation of the P-cluster and M-clusters (45). Moreover, NifH was recently discovered to reduce  $\text{CO}_2$  to CO and hydrocarbons (23, 24). These reactivities all depend on the subunit bridging  $[\text{Fe}_4\text{S}_4]$  cluster. NifH is unusual among  $[\text{Fe}_4\text{S}_4]$  binding proteins because its cluster can access three different oxidation states: the oxidized 2+ state can be generated upon treatment with IDS, the reduced 1+ state can be generated upon treatment with dithionite, and the "super-reduced" all-ferrous 0 state can be generated by treatment with a strong reductant, such as  $\text{Ti}^{\text{III}}$  citrate or  $\text{Eu}^{\text{II}}$ -diethylenetriaminepentaacetic acid (DTPA) (84). The 1+/2+ pair is thought to be used in the reduction of  $\text{N}_2$  by nitrogenase, but the 0/1+ pair could be biologically relevant as well (84–86). When AvNifH or the homologous reductase for V-nitrogenase (AvVnfH) were treated with dithionite to generate the 1+ state, they could reduce  $\text{CO}_2$  to CO (23). Addition of ATP, known to induce conformational changes in NifH, causes a decrease in the redox potential of  $\sim 100\text{mV}$ , and 30% increase in  $\text{CO}_2$  reduction rate. When treated with  $\text{Eu}^{\text{II}}$ -DTPA, the reduction of  $\text{CO}_2$  became catalytic and ATP-independent. Both dithionite and  $\text{Eu}^{\text{II}}$ -DTPA treated AvNifH display a  $g = 1.99$  signal in

perpendicular-mode EPR in the presence of CO<sub>2</sub>, indicating an interaction between CO<sub>2</sub> and the cluster. These proteins were also found to be operative in CO<sub>2</sub> to CO conversion in vivo (23). Further, the reverse process, oxidation of CO to CO<sub>2</sub>, was accomplished by using IDS in reactions to oxidize the cluster. These results demonstrated the ability of NifH and homologs to interconvert CO<sub>2</sub> and CO under ambient conditions.

This process catalyzed by NifH recalls the reversible interconversion of CO<sub>2</sub> and CO by CODH. Carboxydrotrophs use CODH to obtain energy from CO or for fixing carbon into organic molecules (87). Two types of CODH exist, the oxygen-tolerant Mo/CU and anaerobic Ni-FeS. NifH is not homologous or structurally like either of these. The Ni-FeS CODH does contain an iron-sulfur cluster, but its binding of substrates within an open heterometallic site is not possible within NifH, so a distinct mechanism must be at play.

The unique mechanism used by NifH is further supported by the fact that it can, amazingly, reduce CO<sub>2</sub> beyond CO to hydrocarbons. NifH from *Methanosarcina acetivorans* was found to reduce CO<sub>2</sub> to small hydrocarbons in the presence of Eu<sup>II</sup>-DTPA. *Ma*NifH can produce small amounts of hydrocarbons in the presence of dithionite, or larger quantities with a stronger reductant such as Eu<sup>II</sup>-DTPA. *Ma*NifH has a lower redox potential ([Fe<sub>4</sub>S<sub>4</sub>]<sup>1+/2+</sup>: E<sup>0</sup> = -395 mv) than *Av*NifH ([Fe<sub>4</sub>S<sub>4</sub>]<sup>1+/2+</sup>: E<sup>0</sup> = -301 mv) (24). Synthetic 4Fe-4S clusters can also reduce CO<sub>2</sub> and CO to hydrocarbons in a solvent with strong reductants. This result indicates that C<sub>1</sub> substrate reduction is inherent to [Fe<sub>4</sub>S<sub>4</sub>] clusters (23). The better reducing abilities of *Ma*NifH compared to *Av*NifH could be useful for understanding this process.

The biological relevance of hydrocarbon production is known, but some organisms can break down methane and/or ethene to supply energy and carbon (88–90).

## 1.5 Aims of Dissertation

The goal of this dissertation is to investigate how NifB and NifH proteins use  $[\text{Fe}_4\text{S}_4]$  clusters for diverse functions. Many steps of L-cluster formation by NifB have been determined biochemically (19–21, 42, 44). It has been assumed that NifB contains a  $[\text{Fe}_4\text{S}_4]$  cluster cofactor, and two additional  $[\text{Fe}_4\text{S}_4]$  clusters that are cosubstrates for L-cluster formation, but this has not been proven. Without this information, it has been impossible to answer questions about the specific role of each putative  $[\text{Fe}_4\text{S}_4]$  cluster. Additionally, no amino acid residues involved in the carbide insertion pathway have been identified. We set out to determine the amino acid and iron-sulfur cluster components of NifB and their contribution to the M-cluster maturation pathway.

NifH uses a single  $[\text{Fe}_4\text{S}_4]$  cluster cofactor to reduce substrates. NifH has several reductase activities, but perhaps the most interesting is the reduction of  $\text{C}_1$  substrates (23, 24). The specific activity of these reductions depends on the NifH homolog being investigated and the redox state of the cluster.  $\text{C}_1$  substrate reductions by NifH were only recently, and no structural analyses have been performed on NifH proteins to understand these reactions. We endeavored to solve structures of NifH proteins under varying reaction conditions to develop a mechanistic understanding of this process.

### **1.5.1 Specific Aim 1: Characterization of the Iron-Sulfur Clusters of NifB**

NifB contains a  $[\text{Fe}_4\text{S}_4]$  cluster binding motif that is conserved in radical SAM enzymes. Genetic and biochemical evidence also suggests that NifB contains additional FeS cluster precursors used to generate the 8 Fe L-cluster. Based on this, it has been assumed that NifB contains three  $[\text{Fe}_4\text{S}_4]$  clusters. Targeted mutations of putative cluster binding motifs could unveil the precise location of each FeS module, and functional assays can determine the function of each. Identifying the cluster species and their ligands on NifB will give us a new framework for studying nitrogenase cofactor assembly and mechanism. Spectroscopic and biochemical characterization of NifB cluster-binding mutants are presented in Chapter 2 (91).

### **1.5.2 Specific Aim 2: Investigation of an Essential Nitrogen Ligand on NifB**

In our investigation of the amino acids that ligate FeS cluster modules of NifB, we found that one of the  $[\text{Fe}_4\text{S}_4]$  clusters, called K1, also has a nitrogen ligand donated by a conserved histidine. The presence of this histidine suggests that it might have a unique role in the process of L-cluster formation. Moreover, mutation of a functionally important ligand can enable trapping of intermediates that can be very instructive for refining the mechanism of an enzyme. In Chapter 3, the histidine is identified, and functional and structural perturbations caused by mutation of this residue are reported (92).

### 1.5.3 Specific Aim 3: Structure of NifH from *Azotobacter vinelandii* in the All-Ferrous State

NifH from *Azotobacter vinelandii* interconverts CO<sub>2</sub> and CO. Reversibility depends on the redox state of the [Fe<sub>4</sub>S<sub>4</sub>] cluster on NifH. NifH is unusual for having a cluster that can populate 0, 1+, or 2+ states. The most active form for CO<sub>2</sub> reduction is in the "super-reduced" all-ferrous [Fe<sub>4</sub>S<sub>4</sub>]<sup>0</sup> state produced by a strong reductant such as Ti<sup>III</sup>-citrate or Eu<sup>II</sup>-DTPA. A high-resolution crystal structure of NifH in the all-ferrous form could give insights into how the cluster and protein reduce CO<sub>2</sub>. In Chapter 4, a crystal structure of NifH from *Azotobacter vinelandii* is presented, the highest resolution NifH protein to date, revealing asymmetric Arg<sup>100</sup> positions at the putative active site. A model for CO<sub>2</sub> binding and activation by NifH proteins is proposed based on the asymmetric functionality of these conserved Arg residues (93).

### 1.5.4 Specific Aim 4: Structure of NifH from *Methanosarcina acetivorans*

NifH from *Methanosarcina acetivorans* can reduce CO<sub>2</sub> to CO, and also reduce CO and perform C-C coupling to make small hydrocarbons. This process presents a novel way to produce hydrocarbon fuels. Although all NifH proteins are highly homologous and predicted to have the same overall structure, the observed differences in reactivity point to protein structural factors that control substrate reduction. A crystal structure could reveal the structural factors that give *Methanosarcina acetivorans* NifH an extended substrate and product profile. In Chapter 5, a crystal structure of NifH from *Methanosarcina acetivorans* obtained in the presence of dithionite and bicarbonate is presented and analyzed to understand the beginning of the substrate reduction process: capture of CO<sub>2</sub> (94).

## 1.6 References

1. Dos Santos PC, Fang Z, Mason SW, Setubal JC, Dixon R. 2012. Distribution of nitrogen fixation and nitrogenase-like sequences amongst microbial genomes. *BMC Genomics* 13:162.
2. Bulen WA, LeComte JR. 1966. The nitrogenase system from *Azotobacter*: two-enzyme requirement for N<sub>2</sub> reduction, ATP-dependent H<sub>2</sub> evolution, and ATP hydrolysis. *Proc Natl Acad Sci USA* 56:979–986.
3. Ribbe MW, Hu Y, Hodgson KO, Hedman B. 2014. Biosynthesis of Nitrogenase Metalloclusters. *Chem Rev* 114:4063–4080.
4. Seefeldt LC, Yang Z-Y, Lukoyanov DA, Harris DF, Dean DR, Raugei S, Hoffman BM. 2020. Reduction of Substrates by Nitrogenases. *Chem Rev*.
5. Tezcan FA, Kaiser JT, Mustafi D, Walton MY, Howard JB, Rees DC. 2005. Nitrogenase complexes: multiple docking sites for a nucleotide switch protein. *Science* 309:1377–1380.
6. Kim J, Rees DC. 1992. Structural models for the metal centers in the nitrogenase molybdenum-iron protein. *Science* 257:1677–1682.
7. Burgess BK, Lowe DJ. 1996. Mechanism of Molybdenum Nitrogenase. *Chem Rev* 96:2983–3012.
8. Kirn J, Rees DC. 1992. Crystallographic structure and functional implications of the nitrogenase molybdenum-iron protein from *Azotobacter vinelandii*. *Nature* 360:553–560.
9. Lancaster KM, Roemelt M, Ettenhuber P, Hu Y, Ribbe MW, Neese F, Bergmann U, DeBeer S. 2011. X-ray Emission Spectroscopy Evidences a Central Carbon in the Nitrogenase Iron-Molybdenum Cofactor. *Science* 334:974–977.
10. Spatzal T, Aksoyoglu M, Zhang L, Andrade SLA, Schleicher E, Weber S, Rees DC, Einsle O. 2011. Evidence for interstitial carbon in nitrogenase FeMo cofactor. *Science* 334:940.
11. Georgiadis MM, Komiya H, Chakrabarti P, Woo D, Kornuc JJ, Rees DC. 1992. Crystallographic structure of the nitrogenase iron protein from *Azotobacter vinelandii*. *Science* 257:1653–1659.
12. Chiu H, Peters JW, Lanzilotta WN, Ryle MJ, Seefeldt LC, Howard JB, Rees DC. 2001. MgATP-Bound and nucleotide-free structures of a nitrogenase protein complex between the Leu 127 Delta-Fe-protein and the MoFe-protein. *Biochemistry* 40:641–650.

13. Schindelin H, Kisker C, Schlessman JL, Howard JB, Rees DC. 1997. Structure of ADP·AlF<sub>4</sub> – stabilized nitrogenase complex and its implications for signal transduction. 6631. *Nature* 387:370–376.
14. Rutledge HL, Tezcan FA. 2020. Electron Transfer in Nitrogenase. *Chem Rev*.
15. Duval S, Danyal K, Shaw S, Lytle AK, Dean DR, Hoffman BM, Antony E, Seefeldt LC. 2013. Electron transfer precedes ATP hydrolysis during nitrogenase catalysis. *PNAS* 110:16414–16419.
16. Danyal K, Mayweather D, Dean DR, Seefeldt LC, Hoffman BM. 2010. Conformational Gating of Electron Transfer from the Nitrogenase Fe Protein to MoFe Protein. *J Am Chem Soc* 132:6894–6895.
17. Drennan CL, Peters JW. 2003. Surprising cofactors in metalloenzymes. *Current Opinion in Structural Biology* 13:220–226.
18. Beinert H, Holm RH, Münck E. 1997. Iron-Sulfur Clusters: Nature’s Modular, Multipurpose Structures. *Science* 277:653–659.
19. Wiig JA, Hu Y, Ribbe MW. 2011. NifEN-B complex of *Azotobacter vinelandii* is fully functional in nitrogenase FeMo cofactor assembly. *Proc Natl Acad Sci USA* 108:8623–8627.
20. Wiig JA, Hu Y, Lee CC, Ribbe MW. 2012. Radical SAM-Dependent Carbon Insertion into the Nitrogenase M-Cluster. *Science* 337:1672–1675.
21. Tanifuji K, Lee CC, Sickerman NS, Tatsumi K, Ohki Y, Hu Y, Ribbe MW. 2018. Tracing the ‘9th Sulfur’ of the Nitrogenase Cofactor via a Semi-Synthetic Approach. *Nat Chem* 10:568–572.
22. Sickerman N, Ribbe MW, Hu Y. 2017. Nitrogenase Cofactor Assembly: An Elemental Inventory. *Acc Chem Res* 50:2834–2841.
23. Rebelein JG, Stiebritz MT, Lee CC, Hu Y. 2017. Activation and reduction of carbon dioxide by nitrogenase iron proteins. *Nat Chem Biol* 13:147–149.
24. Stiebritz MT, Hiller CJ, Sickerman NS, Lee CC, Tanifuji K, Ohki Y, Hu Y. 2018. Ambient conversion of CO<sub>2</sub> to hydrocarbons by biogenic and synthetic [Fe<sub>4</sub>S<sub>4</sub>] clusters. *Nature Catalysis* 1:444–451.
25. Beinert H. 2000. Iron-sulfur proteins: ancient structures, still full of surprises. *JBIC* 5:2–15.
26. Imlay JA. 2006. Iron-sulphur clusters and the problem with oxygen. *Molecular Microbiology* 59:1073–1082.

27. Bian S, Cowan JA. 1999. Protein-bound iron–sulfur centers. Form, function, and assembly. *Coordination Chemistry Reviews* 190–192:1049–1066.
28. Hosseinzadeh P, Lu Y. 2016. Design and fine-tuning redox potentials of metalloproteins involved in electron transfer in bioenergetics. *Biochimica et Biophysica Acta (BBA) - Bioenergetics* 1857:557–581.
29. Beinert H, Kiley PJ. 1999. Fe-S proteins in sensing and regulatory functions. Current Opinion in *Chemical Biology* 3:152–157.
30. Grove TL, Ahlum JH, Sharma P, Krebs C, Booker SJ. 2010. A Consensus Mechanism for Radical SAM-Dependent Dehydrogenation? BtrN Contains Two [4Fe–4S] Clusters. *Biochemistry* 49:3783–3785.
31. Rouault TA. 2006. The role of iron regulatory proteins in mammalian iron homeostasis and disease. *Nature Chemical Biology* 2:406–414.
32. Haile DJ, Rouault TA, Harford JB, Kennedy MC, Blondin GA, Beinert H, Klausner RD. 1992. Cellular regulation of the iron-responsive element binding protein: disassembly of the cubane iron-sulfur cluster results in high-affinity RNA binding. *Proc Natl Acad Sci USA* 89:11735–11739.
33. Johnson DC, Dean DR, Smith AD, Johnson MK. 2005. Structure, Function, and Formation of Biological Iron-Sulfur Clusters. *Annual Review of Biochemistry* 74:247–281.
34. Dos Santos PC, Johnson DC, Ragle BE, Unciuleac M-C, Dean DR. 2007. Controlled expression of nif and isc iron-sulfur protein maturation components reveals target specificity and limited functional replacement between the two systems. *J Bacteriol* 189:2854–2862.
35. Ayala-Castro C, Saini A, Outten FW. 2008. Fe-S Cluster Assembly Pathways in Bacteria. *Microbiol Mol Biol Rev* 72:110–125.
36. Yuvaniyama P, Agar JN, Cash VL, Johnson MK, Dean DR. 2000. NifS-directed assembly of a transient [2Fe–2S] cluster within the NifU protein. *Proc Natl Acad Sci USA* 97:599–604.
37. Smith AD, Jameson GNL, Dos Santos PC, Agar JN, Naik S, Krebs C, Frazzon J, Dean DR, Huynh BH, Johnson MK. 2005. NifS-Mediated Assembly of [4Fe–4S] Clusters in the N- and C-Terminal Domains of the NifU Scaffold Protein. *Biochemistry* 44:12955–12969.
38. Agar JN, Krebs C, Frazzon J, Huynh BH, Dean DR, Johnson MK. 2000. IscU as a Scaffold for Iron–Sulfur Cluster Biosynthesis: Sequential Assembly of [2Fe–2S] and [4Fe–4S] Clusters in IscU. *Biochemistry* 39:7856–7862.
39. Zheng L, White RH, Cash VL, Jack RF, Dean DR. 1993. Cysteine desulfurase activity indicates a role for NIFS in metallocluster biosynthesis. *Proc Natl Acad Sci* 90:2754–2758.

40. Santos PCD, Smith AD, Frazzon J, Cash VL, Johnson MK, Dean DR. 2004. Iron-Sulfur Cluster Assembly NifU-Directed Activation Of The Nitrogenase Fe Protein. *J Biol Chem* 279:19705–19711.
41. Wilcoxon J, Arragain S, Scandurra AA, Jimenez-Vicente E, Echavarri-Erasun C, Pollmann S, Britt RD, Rubio LM. 2016. Electron Paramagnetic Resonance Characterization of Three Iron–Sulfur Clusters Present in the Nitrogenase Cofactor Maturase NifB from *Methanocaldococcus infernus*. *J Am Chem Soc*. 138:7468-71
42. Wiig JA, Lee CC, Hu Y, Ribbe MW. 2013. Tracing the Interstitial Carbide of the Nitrogenase Cofactor during Substrate Turnover. *J Am Chem Soc* 135:4982–4983.
43. Grunenberg J. 2017. The Interstitial Carbon of the Nitrogenase FeMo Cofactor is Far Better Stabilized than Previously Assumed. *Angewandte Chemie International Edition* 56:7288–7291.
44. Wiig JA, Hu Y, Ribbe MW. 2015. Refining the pathway of carbide insertion into the nitrogenase M-cluster. *Nat Commun* 6:8034.
45. Jasniewski AJ. 2019. Spectroscopic characterization of an eight-iron nitrogenase cofactor precursor that lacks the '9th sulfur.' *Angew Chem Int Ed Engl* 58.
46. Brigle KE, Weiss MC, Newton WE, Dean DR. 1987. Products of the iron-molybdenum cofactor-specific biosynthetic genes, nifE and nifN, are structurally homologous to the products of the nitrogenase molybdenum-iron protein genes, nifD and nifK. *Journal of Bacteriology* 169:1547–1553.
47. Hu Y, Fay AW, Ribbe MW. 2005. Identification of a nitrogenase FeMo cofactor precursor on NifEN complex. *Proc Natl Acad Sci USA* 102:3236–3241.
48. Hu Y, Corbett MC, Fay AW, Webber JA, Hodgson KO, Hedman B, Ribbe MW. 2006. FeMo cofactor maturation on NifEN. *Proc Natl Acad Sci USA* 103:17119–17124.
49. Fay AW, Blank MA, Rebelein JG, Lee CC, Ribbe MW, Hedman B, Hodgson KO, Hu Y. 2016. Assembly scaffold NifEN: A structural and functional homolog of the nitrogenase catalytic component. *Proc Natl Acad Sci USA* 113:9504–9508.
50. Yoshizawa JM, Blank MA, Fay AW, Lee CC, Wiig JA, Hu Y, Hodgson KO, Hedman B, Ribbe MW. 2009. Optimization of FeMoco Maturation on NifEN. *J Am Chem Soc* 131:9321–9325.
51. Wenke BB. 2019. The Many Roles of the Nitrogenase Iron Protein. Dissertation (Ph.D.), California Institute of Technology.
52. Kaiser JT, Hu Y, Wiig JA, Rees DC, Ribbe MW. 2011. Structure of precursor bound NifEN: a nitrogenase FeMo cofactor maturase/insertase. *Science* 331:91–94.

53. Christiansen J, Goodwin PJ, Lanzilotta WN, Seefeldt LC, Dean DR. 1998. Catalytic and Biophysical Properties of a Nitrogenase Apo-MoFe Protein Produced by a *nifB*-Deletion Mutant of *Azotobacter vinelandii*. *Biochemistry* 37:12611–12623.
54. Hu Y, Fay AW, Lee CC, Yoshizawa J, Ribbe MW. 2008. Assembly of nitrogenase MoFe protein. *Biochemistry* 47:3973–3981.
55. Schmid B, Ribbe MW, Einsle O, Yoshida M, Thomas LM, Dean DR, Rees DC, Burgess BK. 2002. Structure of a Cofactor-Deficient Nitrogenase MoFe Protein. *Science* 296:352–356.
56. Sofia HJ, Chen G, Hetzler BG, Reyes-Spindola JF, Miller NE. 2001. Radical SAM, a novel protein superfamily linking unresolved steps in familiar biosynthetic pathways with radical mechanisms: functional characterization using new analysis and information visualization methods. *Nucleic Acids Res* 29:1097–1106.
57. Frey PA, Hegeman AD, Ruzicka FJ. 2008. The Radical SAM Superfamily. *Crit Rev Biochem Mol Biol* 43:63–88.
58. Chirpich TP, Zappia V, Costilow RN, Barker HA. 1970. Lysine 2,3-Aminomutase Purification and Properties of a Pyridoxal Phosphate and S-adenosylmethionine-activated enzyme. *J Biol Chem* 245:1778–1789.
59. Moss M, Frey PA. 1987. The role of S-adenosylmethionine in the lysine 2,3-aminomutase reaction. *J Biol Chem* 262:14859–14862.
60. Birch OM, Fuhrmann M, Shaw NM. 1995. Biotin synthase from *Escherichia coli*, an investigation of the low molecular weight and protein components required for activity in vitro. *J Biol Chem* 270:19158–19165.
61. Sun X, Harder J, Krook M, Jörnvall H, Sjöberg BM, Reichard P. 1993. A possible glycine radical in anaerobic ribonucleotide reductase from *Escherichia coli*: nucleotide sequence of the cloned *nrdD* gene. *PNAS* 90:577–581.
62. Mulliez E, Fontecave M, Gaillard J, Reichard P. 1993. An iron-sulfur center and a free radical in the active anaerobic ribonucleotide reductase of *Escherichia coli*. *J Biol Chem* 268:2296–2299.
63. Knappe J, Schacht J, Möckel W, Höpner T, Vetter H, Edenharder R. 1969. Pyruvate Formate-Lyase Reaction in *Escherichia coli*. *European Journal of Biochemistry* 11:316–327.
64. Busby RW, Schelvis JPM, Yu DS, Babcock GT, Marletta MA. 1999. Lipoic Acid Biosynthesis: LipA Is an Iron–Sulfur Protein. *J Am Chem Soc* 121:4706–4707.
65. Sanyal I, Cohen G, Flint DH. 1994. Biotin synthase: purification, characterization as a [2Fe-2S]cluster protein, and in vitro activity of the *Escherichia coli* *bioB* gene product. *Biochemistry* 33:3625–3631.

66. Knappe J, Neugebauer FA, Blaschkowski HP, Gänzler M. 1984. Post-translational activation introduces a free radical into pyruvate formate-lyase. *Proc Natl Acad Sci USA* 81:1332–1335.
67. Henshaw TF, Cheek J, Broderick JB. 2000. The [4Fe-4S]<sub>1+</sub> Cluster of Pyruvate Formate-Lyase Activating Enzyme Generates the Glycyl Radical on Pyruvate Formate-Lyase: EPR-Detected Single Turnover. *J Am Chem Soc* 122:8331–8332.
68. Ballinger MD, Reed GH, Frey PA. 1992. An organic radical in the lysine 2,3-aminomutase reaction. *Biochemistry* 31:949–953.
69. Reed KE, Cronan JE. 1993. Lipoic acid metabolism in Escherichia coli: sequencing and functional characterization of the lipA and lipB genes. *J Bacteriol* 175:1325.
70. Magnusson OTh, Reed GH, Frey PA. 1999. Spectroscopic Evidence for the Participation of an Allylic Analogue of the 5'-Deoxyadenosyl Radical in the Reaction of Lysine 2,3-Aminomutase. *J Am Chem Soc* 121:9764–9765.
71. Vey JL, Drennan CL. 2011. Structural Insights into Radical Generation by the Radical SAM Superfamily. *Chem Rev* 111:2487–2506.
72. Bruender NA, Young AP, Bandarian V. 2015. Chemical and Biological Reduction of the Radical SAM Enzyme 7-Carboxy-7-deazaguanine Synthase. *Biochemistry* 54:2903–2910.
73. Yang H, McDaniel EC, Impano S, Byer AS, Jodts RJ, Yokoyama K, Broderick WE, Broderick JB, Hoffman BM. 2019. The Elusive 5'-Deoxyadenosyl Radical: Captured and Characterized by Electron Paramagnetic Resonance and Electron Nuclear Double Resonance Spectroscopies. *J Am Chem Soc* 141:12139–12146.
74. Sayler RI, Stich TA, Joshi S, Cooper N, Shaw JT, Begley TP, Tantillo DJ, Britt RD. 2019. Trapping and Electron Paramagnetic Resonance Characterization of the 5'dAdo• Radical in a Radical S-Adenosyl Methionine Enzyme Reaction with a Non-Native Substrate. *ACS Cent Sci* 5:1777–1785.
75. Mulliez E, Duarte V, Arragain S, Fontecave M, Atta M. 2017. On the Role of Additional [4Fe-4S] Clusters with a Free Coordination Site in Radical-SAM Enzymes. *Front Chem.* 5:17
76. Lanz ND, Grove TL, Gogonea CB, Lee K-H, Krebs C, Booker SJ. 2012. RlmN and AtsB as models for the overproduction and characterization of radical SAM proteins. *Meth Enzymol* 516:125–152.
77. Hänzelmann P, Schindelin H. 2006. Binding of 5'-GTP to the C-terminal FeS cluster of the radical S-adenosylmethionine enzyme MoaA provides insights into its mechanism. *Proc Natl Acad Sci USA* 103:6829–6834.

78. Ugulava NB, Sacanell CJ, Jarrett JT. 2001. Spectroscopic changes during a single turnover of biotin synthase: destruction of a [2Fe-2S] cluster accompanies sulfur insertion. *Biochemistry* 40:8352–8358.
79. Jameson GNL, Coper MM, Hernández HL, Johnson MK, Huynh BH. 2004. Role of the [2Fe-2S] cluster in recombinant *Escherichia coli* biotin synthase. *Biochemistry* 43:2022–2031.
80. Booker SJ, Cicchillo RM, Grove TL. 2007. Self Sacrifice in Radical S-adenosylmethionine Proteins. *Curr Opin Chem Biol* 11:543–552.
81. Bauerle MR, Schwalm EL, Booker SJ. 2015. Mechanistic Diversity of Radical S-Adenosylmethionine (SAM)-dependent Methylation. *J Biol Chem* 290:3995–4002.
82. Boal AK, Grove TL, McLaughlin MI, Yennawar NH, Booker SJ, Rosenzweig AC. 2011. Structural Basis for Methyl Transfer by a Radical SAM Enzyme. *Science* 332:1089–1092.
83. Landgraf BJ, Arcinas AJ, Lee K-H, Booker SJ. 2013. Identification of an Intermediate Methyl Carrier in the Radical SAM Methylthiotransferases, RimO and MiaB. *J Am Chem Soc* 135:15404–15416.
84. Watt GD, Reddy KRN. 1994. Formation of an all ferrous Fe<sub>4</sub>S<sub>4</sub> cluster in the iron protein component of *Azotobacter vinelandii* nitrogenase. *Journal of Inorganic Biochemistry* 53:281–294.
85. Watt GD, Wang ZC, Knotts RR. 1986. Redox reactions of and nucleotide binding to the iron protein of *Azotobacter vinelandii*. *Biochemistry* 25:8156–8162.
86. Angove HC, Yoo SJ, Burgess BK, Münck E. 1997. Mössbauer and EPR Evidence for an All-Ferrous Fe<sub>4</sub>S<sub>4</sub> Cluster with S = 4 in the Fe Protein of Nitrogenase. *J Am Chem Soc* 119:8730–8731.
87. Robb FT, Techtmann SM. 2018. Life on the fringe: microbial adaptation to growth on carbon monoxide. *F1000Res* 7.
88. Roslev P, Iversen N, Henriksen K. 1997. Oxidation and assimilation of atmospheric methane by soil methane oxidizers. *Appl Environ Microbiol* 63:874–880.
89. Coleman NV, Spain JC. 2003. Distribution of the Coenzyme M Pathway of Epoxide Metabolism among Ethene- and Vinyl Chloride-Degrading Mycobacterium Strains. *Appl Environ Microbiol* 69:6041–6046.
90. Hanson RS, Hanson TE. 1996. Methanotrophic bacteria. *Microbiol Mol Biol Rev* 60:439–471.

91. Rettberg LA, Wilcoxon J, Lee CC, Stiebritz MT, Tanifuji K, Britt RD, Hu Y. 2018. Probing the coordination and function of Fe<sub>4</sub>S<sub>4</sub> modules in nitrogenase assembly protein NifB. *Nature Communications* 9:1–8.
92. Rettberg LA, Wilcoxon J, Jasniewski AJ, Lee CC, Tanifuji K, Hu Y, Britt RD, Ribbe MW. 2020. Identity and function of an essential nitrogen ligand of the nitrogenase cofactor biosynthesis protein NifB. *Nature Communications* 11:1–8.
93. Rettberg LA, Stiebritz MT, Kang W, Lee CC, Ribbe MW, Hu Y. 2019. Structural and Mechanistic Insights into CO<sub>2</sub> Activation by Nitrogenase Iron Protein. *Chemistry – A European Journal* 25:13078–13082.
94. Rettberg LA, Kang W, Stiebritz MT, Hiller CJ, Lee CC, Liedtke J, Ribbe MW, Hu Y. 2019. Structural Analysis of a Nitrogenase Iron Protein from *Methanosarcina acetivorans*: Implications for CO<sub>2</sub> Capture by a Surface-Exposed [Fe<sub>4</sub>S<sub>4</sub>] Cluster. *mBio* 10.

## **Chapter 2: Characterization of the Iron-Sulfur Clusters of NifB**

## 2.1 Introduction

The structure-function relationships of nitrogenase, especially relating to the M-cluster, are crucial to understanding the mechanism of N<sub>2</sub> reduction. However, despite decades of research into nitrogenase, it was not until 2011 that the complete structure of M-cluster was determined (1, 2). In that year, X-ray crystallography and X-ray emission spectroscopy studies identified a  $\mu_6$  carbide in the center of M-cluster. Soon after, the source of this carbide was traced to NifB (3). NifB plays a crucial role in M-cluster biosynthesis by transforming small, putative 4Fe units (K-cluster) into an 8Fe entity (L-cluster) that has the complete FeS core structure in place, as well as the interstitial carbide. NifB carries the signature CXXXCXXC radical SAM motif that ligates a [Fe<sub>4</sub>S<sub>4</sub>] cluster in members of the radical S-adenosyl-L-methionine (SAM) enzyme family (4, 5). NifB also contains additional amino acids that could potentially coordinate Fe atoms of the L-cluster precursor (6–9). NifB from the nitrogenase model organism, *Azotobacter vinelandii* (Av), proved to be unstable and difficult to isolate, a problem that was overcome by fusing AvNifB to AvNifEN, to form a NifEN-B chimera, a naturally occurring protein architecture in some diazotrophs (10). Experiments with NifEN-B demonstrated many of the fundamental biochemical functionalities of NifB, including proving that NifB was a radical SAM enzyme and that the interstitial carbide originates from a SAM-derived methyl group. A limitation of the NifEN-B fusion protein is that it contains a multitude of FeS clusters, complicating determination of the spectroscopic and functional contribution of each. Furthermore, AvNifB has an additional domain that is not essential for function but contributes to instability and could potentially bind to extra clusters (6, 10). NifB proteins from methanogenic archaea,

including *Methanosarcina acetivorans* (*Ma*), lack the extra domain and can be expressed heterologously from *E. coli* (6, 11), overcoming the limitations of NifEN-B. NifB heterologously expressed in *E. coli* does not contain the requisite FeS clusters needed to function, so it must be reconstituted with FeS clusters, a process recently perfected (12).

Characterization of the NifB proteins from *Azotobacter vinelandii* (3, 10, 13) and *Methanosarcina acetivorans* (6) has unveiled a radical SAM-dependent mechanism employed by NifB for carbide insertion, which begins with methyl transfer in an SN<sub>2</sub>-type mechanism from SAM to a putative [Fe<sub>4</sub>S<sub>4</sub>] cluster (13). Subsequently, the methyl group undergoes hydrogen abstraction by a SAM-derived 5'-deoxyadenosyl (5'-dA•) radical. Further deprotonation and/or dehydrogenation of the resultant carbon radical occurs concomitantly with the coupling of the putative [Fe<sub>4</sub>S<sub>4</sub>] clusters pair and rearrangement into an [Fe<sub>8</sub>S<sub>9</sub>C] core. Previous studies suggest that NifB contains three [Fe<sub>4</sub>S<sub>4</sub>] clusters modules: two that form the [Fe<sub>4</sub>S<sub>4</sub>] modules (designated K1 and K2) that become coupled into the [Fe<sub>8</sub>S<sub>9</sub>C] cofactor precursor and a third that binds to SAM and triggers radical SAM-dependent carbide insertion. However, despite progress in elucidating the mechanism of NifB (3, 8, 11, 13–16), questions remain as to the 4Fe nature of the building blocks used to generate the 8Fe core, the identity of coordinating ligands of the cluster modules, and the biosynthetic events that occur on each of these NifB-associated cluster modules.

Here, we used continuous-wave electron paramagnetic resonance spectroscopy to show that K1- and K2-modules are 3-cysteine-coordinated [Fe<sub>4</sub>S<sub>4</sub>] clusters (17). Further, we demonstrate that the coexistence of SAM and K2-modules are a prerequisite for methyl transfer to K2 and

hydrogen abstraction from the K2-associated methyl by a 5'-deoxyadenosyl radical. These results establish an important framework for mechanistic explorations of NifB while highlighting the utility of a synthetic-cluster-based reconstitution approach employed herein in functional analyses of iron-sulfur (FeS) enzymes.

Here, we demonstrate that NifB variants carrying the individual K1-, K2- and SAM-modules can be reconstituted with synthetic  $[\text{Fe}_4\text{S}_4]$  clusters, thereby providing conclusive evidence that NifB consists of three distinct 4Fe modules. Continuous-wave electron paramagnetic resonance (CW-EPR) analysis reveals that 3 Cys ligands coordinate both the K1- and K2- modules.

Biochemical experiments further demonstrate that coexistence of the SAM- and K2-modules is a prerequisite for methylation of the K2-derived sulfide atom and the subsequent hydrogen abstraction from the K2-associated methyl group by a 5'-dA• radical. These results not only lay a necessary foundation for further mechanistic investigations of the NifB-catalyzed reactions but also point to the utility of the synthetic-cluster-based reconstitution protocol in functional analyses of other FeS systems.

Together, these results suggest the presence and concerted action of three 4Fe modules, namely, the two 4Fe modules (designated the K1- and K2-modules) that give rise to the K-cluster and a third 4Fe module that is ligated by the radical SAM motif (designated the SAM-module), on NifB. Knowledge of the biosynthetic mechanism of M-cluster could facilitate the development of biomimetic catalysts for ambient conversion of  $\text{N}_2$  into valuable chemical commodities.

## 2.2 Materials and Methods

### 2.2.1 General Information

Unless otherwise specified, all chemicals were purchased from Sigma-Aldrich (St. Louis, MO) and Thermo-Fisher Scientific (Waltham, MA).

### 2.2.2 Cell Growth and Protein Purification

*E. coli* strains expressing His-tagged *MaNifB*<sup>wt</sup> (strain YM114EE), *MaNifB*<sup>SAM</sup> (strain YM163EE), *MaNifB*<sup>K1</sup> (strain YM165EE), *MaNifB*<sup>K2</sup> (strain YM166EE), *MaNifB*<sup>SAM+K1</sup> (strain YM180EE), and *MaNifB*<sup>SAM+K2</sup> (strain YM181EE) were grown in Difco LB medium containing 100 mg L<sup>-1</sup> ampicillin (BD Biosciences) in a BIOFLO 415 fermenter (New Brunswick Scientific) at a temperature of 37 °C, an agitation of 200 rpm and an airflow of 10 L min<sup>-1</sup>. When the cell density (measured at OD<sub>600</sub>) reached 0.5, 25 μM IPTG was added to the cell culture to induce protein expression at 25 °C for 16 h. Subsequently, cells were harvested by centrifugation and stored at -79 °C until the day of purification. His-tagged *MaNifB* proteins were purified using previously published methods (6, 10).

### 2.2.3 Cluster Reconstitution and Maturation

As-isolated *MaNifB* contains some FeS-cluster species that are removed before reconstitution with synthetic [Fe<sub>4</sub>S<sub>4</sub>] clusters. The as-isolated wild-type or variant *MaNifB* protein was treated with 20 mM bathophenanthroline disulfonate, an iron chelator, in a buffer containing 5 mM

MgATP, 2 mM sodium dithionite (DT; Na<sub>2</sub>S<sub>2</sub>O<sub>4</sub>), 50 mM Tris–HCl (pH 8) and 500 mM NaCl, followed by incubation at room temperature for 1 h to remove the endogenous FeS clusters associated with the protein. Subsequently, this mixture was diluted with a buffer containing 50 mM Tris–HCl (pH 8) and loaded on a Q Sepharose column (GE Healthcare). The column was then washed with a buffer containing 2 mM DT, 50 mM Tris–HCl (pH 8) and 100 mM NaCl prior to elution of the *MaNifB* protein with a buffer containing 50 mM Tris–HCl (pH 8). Reconstitution of the wild-type or variant *MaNifB* protein with synthetic [Fe<sub>4</sub>S<sub>4</sub>] clusters (designated [Fe<sub>4</sub>S<sub>4</sub>]<sup>Syn</sup>) (12) was carried out by adding a dimethylformamide (DMF) solution of [Fe<sub>4</sub>S<sub>4</sub>]<sup>Syn</sup> dropwise at a molar ratio of 5:1 to the *MaNifB* protein in a buffer containing 2 mM DT, 20 mM β-mercaptoethanol, 50 mM Tris–HCl (pH 8), and 500 mM NaCl, with continuous stirring on ice. After incubation on ice for 1 h, the reaction mixture was diluted with a buffer containing 2 mM DT and 50 mM Tris–HCl (pH 8) and loaded onto a Q Sepharose column. The column was then washed with a buffer containing 2 mM DT, 50 mM Tris–HCl, and 100 mM NaCl before elution of the reconstituted *MaNifB* with a buffer containing 2 mM DT, 50 mM Tris–HCl (pH 8), and 500 mM NaCl. The *MaNifB*<sup>SAM</sup>, *MaNifB*<sup>K1</sup>, *MaNifB*<sup>K2</sup>, *MaNifB*<sup>SAM+K1</sup>, and *MaNifB*<sup>SAM+K2</sup> variants were used as they were for EPR analysis. In contrast, *MaNifB*<sup>wt</sup> was incubated with SAM using an established protocol (6), which process its K-cluster was matured into an L-cluster, prior to EPR analysis of the resultant protein species (designated *MaNifB*<sup>L</sup>).

#### **2.2.4 Iron Determination**

Each protein sample was mixed with 100  $\mu\text{L}$  concentrated sulfuric acid ( $\text{H}_2\text{SO}_4$ ) and 100  $\mu\text{L}$  concentrated nitric acid ( $\text{HNO}_3$ ), and the mixture was heated at 250  $^\circ\text{C}$  for 30 min. This procedure was repeated until the mixture became colorless, followed by cooling of the mixture to room temperature and dilution of the mixture to a total volume of 10 mL with 2%  $\text{HNO}_3$  before sample analysis. The iron concentrations of the wild-type and variant *MaNifB* proteins were determined by inductively coupled plasma optical emission spectroscopy (ICP-OES) analysis using a Thermo Scientific iCAP7000. Calibration curves were created by making standard solutions from dilutions of a 1  $\text{mg mL}^{-1}$  stock solution of elemental iron (Inorganic Ventures, Christiansburg, VA).

#### **2.2.5 Electron Paramagnetic Resonance (EPR) Analysis**

Samples were prepared in a Vacuum Atmospheres glove box with  $< 1$  ppm  $\text{O}_2$  and flash-frozen in liquid nitrogen before analysis. Reduced samples contained 50 mM Tris-HCl (pH 8), 500 mM NaCl, and 2 mM DT. CW EPR spectra were recorded by an ESP 300  $E_z$  spectrophotometer (Bruker) interfaced with an ESR-9002 liquid-helium continuous-flow cryostat (Oxford Instruments) using a microwave power of 5 mW, a gain of  $5 \times 10^4$ , a modulation frequency of 100 kHz, and a modulation amplitude of 5 G. Five scans of perpendicular-mode EPR were recorded at 20 K using a microwave frequency of 9.62 GHz.

### 2.2.6 SAM Cleavage Assay

Each SAM cleavage reaction contained 25 mM Tris–HCl (pH 8), 5% glycerol (v/v), 40  $\mu$ M *Ma*NifB, and 0.3  $\mu$ M SAM in a total volume of 0.3 mL. The reaction mixture was incubated at 25 °C for 60 min with intermittent mixing and terminated by filtration through Amicon Ultra 30,000 MWCO centrifugal filters. Subsequently, trifluoroacetic acid (TFA) was added to the reaction mixture at a concentration of 0.14%, followed by an analysis of the resultant sample by a Thermo Scientific Dionex Ultimate 3000 UHPLC system, equipped with an Acclaim 120 C18 column (4.6  $\times$  100 mm, 5- $\mu$ m particle size). The column was equilibrated with 98% buffer A (50 mM KH<sub>2</sub>PO<sub>4</sub>, pH 6.6) and 2% buffer B (100% methanol) before each sample injection (100  $\mu$ L per sample) for at least 5 min. Following sample injection, a linear gradient of 2–60% buffer B was applied to the column for 20 min, followed by an isocratic flow with 60% buffer B for 8 min, and a linear gradient of 60–2% buffer B for 4 min. Throughout the run, the flow rate of buffer was kept at 0.5 mL min<sup>-1</sup>, and the column was kept at 30 °C. The elution of products was monitored by absorption of 254 nm wavelength light.

### 2.2.7 Methanethiol Assay

A published method was adapted for the *Ma*NifB dependent production of methanethiol (13, 18). The procedure involved the removal of excess DT from *Ma*NifB via gel filtration with Sephadex G-25 fine resin that was equilibrated with a buffer containing 25 mM Tris–HCl (pH 8). Subsequently, 40 nmol of *Ma*NifB was mixed with 400 nmol SAM in a total volume of 100  $\mu$ L in a sealed 300- $\mu$ L glass vial, incubated for 30 min at 25 °C, and quenched by 25  $\mu$ L of 1 M HCl.

Acid-quenched samples were then incubated at 60 °C for 15 min to release the volatile methanethiol into the headspace, followed by equilibration of the sample to room temperature for 10 min, and injection of the entire headspace by a gas-tight syringe onto a Restek Rxi-1ms column (30 m, 0.32 mm ID, 4 μm df) (Restek, Bellefonte, PA) for analysis by GC–MS (Thermo-Fisher Scientific Trace 1300 GC connected to a Thermo-Fisher Scientific ISQ QD single quadrupole mass spectrometry). During each GC–MS run, the GC inlet, and oven temperatures were kept at 30 °C, and the mass spectrometry transfer line and ion source were held at 250 °C. Using SIM conditions in electron ionization mode, methanethiol was detected at an  $m/z$  ratio of 47.

## 2.3 Results and Discussion

### 2.3.1 Establishing the 4Fe Nature of Modules on NifB

NifB from *Methanosarcina acetivorans* (*MaNifB*) was previously expressed in *E.coli* and was active after reconstitution with FeS clusters (6). Functional and spectroscopic evidence is consistent with NifB containing three [Fe<sub>4</sub>S<sub>4</sub>] clusters initially, but they have not been directly observed or characterized (6, 10, 11). To investigate the individual cluster-binding modules of *MaNifB*, a series of variants—each carrying one of the three proposed 4Fe modules—were generated. Sequence analysis of *MaNifB* reveals the presence of three groups of highly conserved Cys residues—three Cys residues per group—that could potentially serve as ligands for the SAM-, K1-, and K2-modules of NifB (Fig. 2.1 a, b). Specifically, Cys<sup>50</sup>, Cys<sup>54</sup>, and Cys<sup>57</sup>, which form the canonical CxxxCxxC radical SAM motif, are assigned to the SAM-module; Cys<sup>30</sup>,

Cys<sup>63</sup>, and Cys<sup>129</sup>, which are located toward the N terminus of the primary sequence, are assigned to the K1 module; and Cys<sup>264</sup>, Cys<sup>274</sup>, and Cys<sup>277</sup>, which are positioned toward the C terminus of the primary sequence, are assigned to the K2 module (Fig. 2.1 a, b). Based on the tentative assignment of the Cys residues, each cluster-binding module of *MaNifB* can be studied independently by mutating the Cys ligands of the other two modules to Ala. This approach was used to generate three constructs, each encoding a *MaNifB* variant with either a SAM (designated *MaNifB*<sup>SAM</sup>)-, K1 (designated *MaNifB*<sup>K1</sup>)-, or K2 (designated *MaNifB*<sup>K2</sup>)-module. However, the as-isolated proteins do not contain FeS clusters in full occupancy. This problem was overcome by using a recently developed protocol (12) first to remove the endogenous FeS clusters of the *MaNifB* variants and then reconstitute these proteins with a synthetic [Fe<sub>4</sub>S<sub>4</sub>] compound. Such a reconstitution approach has been successfully applied to identify the source of the 9th sulfur during the cofactor maturation process on *MaNifB* (12) without the interference of Fe/S impurities that are often introduced by the traditional FeCl<sub>3</sub>/Na<sub>2</sub>S-based reconstitution methods. Here this method was used to conclusively determine the [Fe<sub>4</sub>S<sub>4</sub>] identity of the individual modules in *MaNifB*.

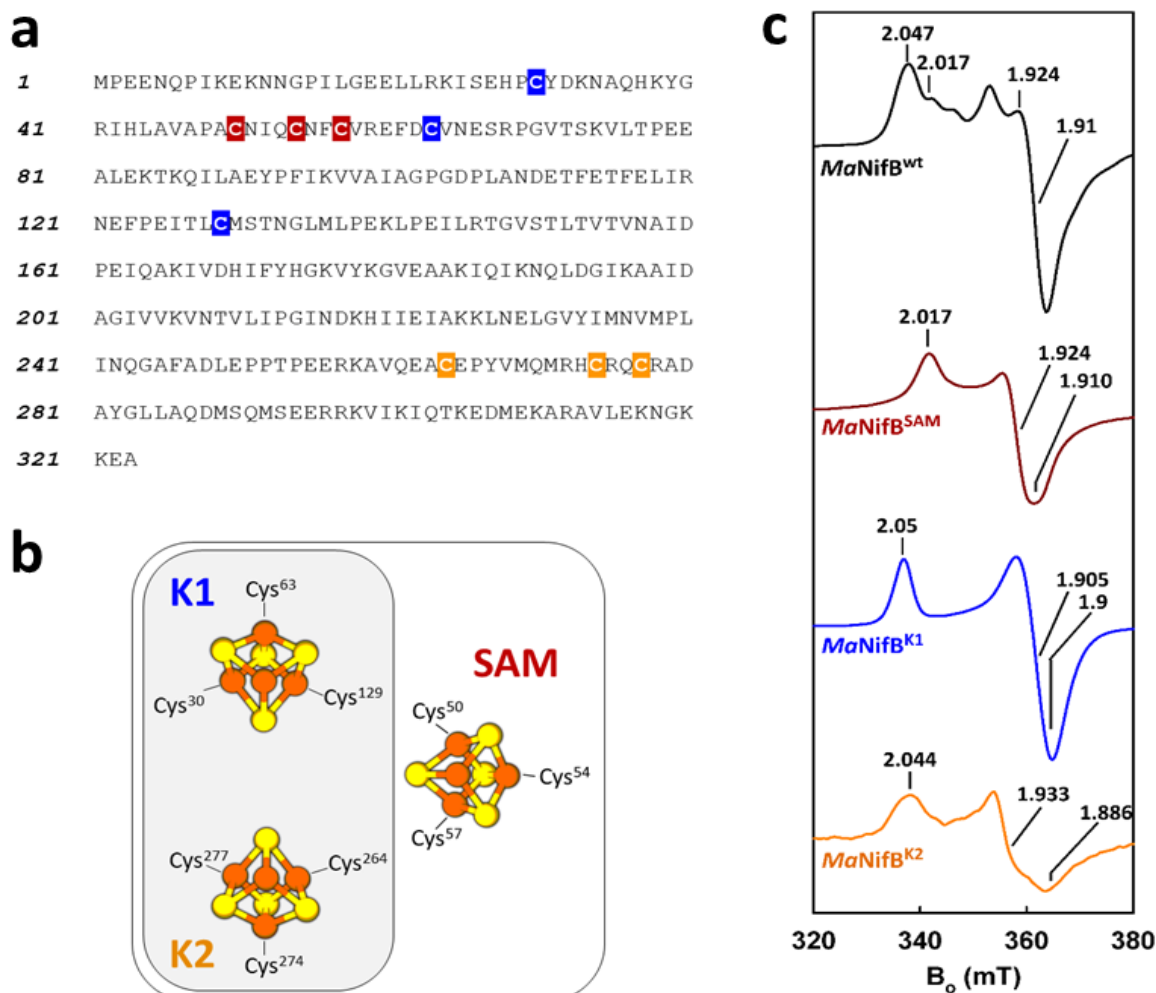


**Figure 2.1 Assignment of three  $[\text{Fe}_4\text{S}_4]$  cluster modules in *MaNifB*.** **a** *MaNifB* primary sequence with conserved Cys residues (6) highlighted. **b** Schematic presentations of the SAM-, K1-, and K2-modules in *MaNifB*. A 3-Cys ligation pattern is proposed for all three modules, with the proposed ligands indicated in each module. **c** EPR spectra of the synthetic  $[\text{Fe}_4\text{S}_4]$  cluster-reconstituted wild-type *MaNifB* (*MaNifB<sup>wt</sup>*, black) and *MaNifB* variants carrying the SAM (*MaNifB<sup>SAM</sup>*, brown), K1 (*MaNifB<sup>K1</sup>*, blue), and K2 (*MaNifB<sup>K2</sup>*, orange) modules, respectively. The spectra were collected as described in Section 2.2.5, and the  $g$  values of each spectrum are indicated. The CW EPR experiment was performed four times. Representative results are shown in **c**. See Table 2.1 for Fe contents.

Indeed, analysis of the Fe content of each protein after in vitro reconstitution indicated successful incorporation of clusters (Table 2.1). Moreover, upon reduction with dithionite, each of the three *MaNifB* variants has an  $S = 1/2$  electron paramagnetic resonance (EPR) signal that is characteristic of a  $[\text{Fe}_4\text{S}_4]^+$  cluster (Fig. 2.1 c).

The spectra of each variant have distinct  $g$  values ( $MaNifB^{SAM}$ :  $g = [2.017\ 1.924\ 1.910]$ ;  $MaNifB^{K1}$ :  $g = [2.050\ 1.905\ 1.900]$ ;  $MaNifB^{K2}$ :  $g = [2.044\ 1.933\ 1.886]$ ) and most of the EPR features of the individual modules are identifiable in the spectrum of the wild-type  $MaNifB$  (Fig. 2.1 c). These observations are exciting, as they provide strong support for the assignment of the respective Cys residues as the ligands of the three modules in  $MaNifB$  while supplying direct proof for the  $[Fe_4S_4]$  identity of the K1- and K2-modules.

Protein	Fe Content	
	(mol Fe mol protein <sup>-1</sup> )	(% Occupancy)
<b><i>MaNifB</i><sup>wt</sup></b>	<b>11.9 ± 1.1</b>	<b>99</b>
<b><i>MaNifB</i><sup>SAM</sup></b>	<b>3.1 ± 0.4</b>	<b>78</b>
<b><i>MaNifB</i><sup>K1</sup></b>	<b>3.9 ± 0.1</b>	<b>98</b>
<b><i>MaNifB</i><sup>K2</sup></b>	<b>2.6 ± 0.4</b>	<b>64</b>

**Table 2.1 Iron content of wild-type *MaNifB* and single module variants.** The amount of protein-bound iron present on  $MaNifB^{wt}$ ,  $MaNifB^{SAM}$ ,  $MaNifB^{K1}$ ,  $MaNifB^{K2}$  was quantified by digestion of protein in acid and analysis by ICP-OES, as described in Section 2.2.4.

### 2.3.2 Defining the Functions of NifB-Associated Modules.

Having established the presence of three distinct  $[Fe_4S_4]$  modules in  $MaNifB$ , the next question to answer is which biosynthetic event occurs on each module. Because our primary interest is in how the SAM-module works with the K1- and K2-modules during the cluster maturation process, two additional  $MaNifB$  variants were first created: one containing the SAM- and K1-modules (designated  $MaNifB^{SAM+K1}$ ) and the other harboring the SAM- and K2-modules (designated  $MaNifB^{SAM+K2}$ ). These variants were expressed in *E. coli*, followed by purification and reconstitution with the synthetic  $[Fe_4S_4]$  compound (Table 2.2).

Protein	Fe Content	
	(mol Fe mol protein <sup>-1</sup> )	(% Occupancy)
<i>MaNifB</i> <sup>SAM+K1</sup>	6.5 ± 0.7	81
<i>MaNifB</i> <sup>SAM+K2</sup>	6.3 ± 0.6	78

**Table 2.2 Iron content of *MaNifB* double module variants.** The amount of protein-bound iron present on *MaNifB*<sup>SAM+K1</sup> and *MaNifB*<sup>SAM+K2</sup> was quantified by digestion of protein in acid and analysis by ICP-OES, as described in Section 2.2.4.

Interestingly, the EPR spectra of neither *MaNifB*<sup>SAM+K1</sup> nor *MaNifB*<sup>SAM+K2</sup> is a simple summation of the individual spectra of the respective cluster modules. In essence, the *MaNifB*<sup>SAM+K2</sup> spectrum resembles the *MaNifB*<sup>SAM</sup> spectrum in line-shape but is somewhat broadened and displayed a new  $g_{app} = 1.92$  feature (Fig. 2.2 a, green trace). Whereas the *MaNifB*<sup>SAM+K1</sup>

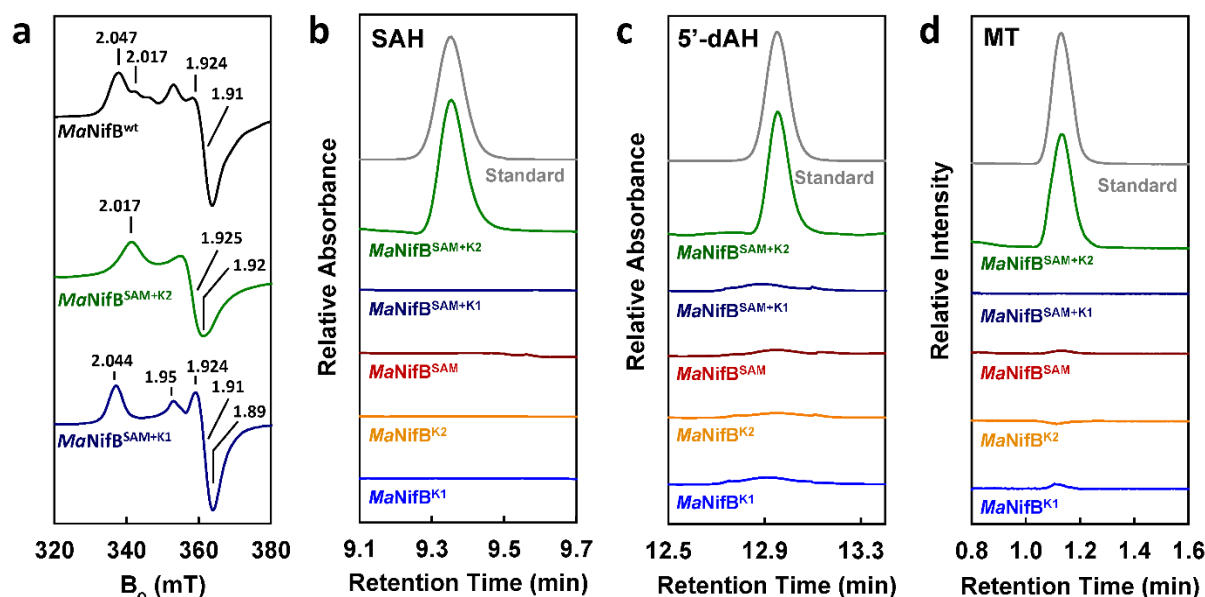


**Figure 2.2 Spectroscopic and functional properties of dual cluster *MaNifB* variants.** **a** EPR spectra of the synthetic [Fe<sub>4</sub>S<sub>4</sub>] cluster-reconstituted wild-type *MaNifB* (*MaNifB*<sup>wt</sup>, black) and *MaNifB* variants carrying SAM plus K2 (*MaNifB*<sup>SAM+K2</sup>, green) and SAM plus K1 (*MaNifB*<sup>SAM+K1</sup>, dark blue) modules, respectively. **b, c** HPLC elution profiles of SAH (**b**) and 5'-dAH (**c**) standards (gray), and those of SAM incubated with *MaNifB* variants carrying K1 (*MaNifB*<sup>K1</sup>, light blue), K2 (*MaNifB*<sup>K2</sup>, orange), SAM (*MaNifB*<sup>SAM</sup>, brown), SAM plus K1 (*MaNifB*<sup>SAM+K1</sup>, dark blue), and SAM plus K2 (*MaNifB*<sup>SAM+K2</sup>, green) modules, respectively. **d** GC analyses of the methanethiol (MT) standard (gray) and acid-quenched incubation mixtures containing SAM and *MaNifB* variants carrying K1 (*MaNifB*<sup>K1</sup>, light blue) and K2 (*MaNifB*<sup>K2</sup>, orange), SAM (*MaNifB*<sup>SAM</sup>, brown), SAM plus K1 (*MaNifB*<sup>SAM+K1</sup>, dark blue), and SAM plus K2 (*MaNifB*<sup>SAM+K2</sup>, green) modules, respectively. The CW EPR (**a**), HPLC (**b, c**), and GC (**d**) experiments were performed three times each. Representative results are shown in the figure. See Table 2.2 for Fe contents of samples.

spectrum resembles the *MaNifB*<sup>K1</sup> spectrum in line-shape but is broadened and also displays a distinct  $g_{\text{app}} = 1.95$  feature (Fig. 2.2 a, blue trace).

For wild-type *MaNifB*<sup>wt</sup>, incubation of with *S*-adenosyl-L-methionine gives two products that can be detected by HPLC: *S*-adenosyl-L-homocysteine (SAH) from the methyl transfer step and 5'-deoxyadenosine (5'-dAH) from reductive homolytic cleavage. The transferred methyl is released as methanethiol (MT) when acid-quenched and can be detected by GC-MS. HPLC of the variants revealed that, like the wild-type *MaNifB*, *MaNifB*<sup>SAM+K2</sup> is capable of cleaving SAM into *S*-adenosyl-L-homocysteine (SAH) and 5'-deoxyadenosine (5'-dAH); in contrast, *MaNifB*<sup>SAM+K1</sup> did not produce either product (Fig. 2.2 b, c). Methanethiol is also only detected upon acid quenching an incubation mixture of *MaNifB*<sup>SAM+K2</sup> and SAM, but not with *MaNifB*<sup>SAM+K1</sup> and SAM. (Fig. 2.2 d). The single cluster mutants did not show activity in either assay (Fig. 2.2, b,c,d). These observations suggest that the K2-module serves at the location for methyl attachment. Furthermore, the results indicate that the presence of both SAM- and K2-modules is the prerequisite for both SAM-related reactions to occur. The K2-module serves as the final location for methyl attachment and the SAM-module supplying a 5'-dA• radical for hydrogen abstraction of the K2-associated methyl group.

## 2.4 Summary and Conclusion

While details of the various biosynthetic events on NifB await further investigation, the current study conclusively establishes the presence of three [Fe<sub>4</sub>S<sub>4</sub>] units on NifB. It also provides useful insights into the coordination and function of each module in the process of K- to L-cluster

transformation, taking advantage of the synthetic  $[\text{Fe}_4\text{S}_4]$ -cluster-based reconstitution approach that can be applied to the functional analyses of a wide range of other FeS enzymes. The series of variants carrying different combinations of the three modules of NifB could also be used to uncouple the various steps of the cluster transformation process.

Another interesting point to note is the absence of SAH formation in the presence of the K2 module alone. This observation could be accounted for by the lack of a nearby SAM-module that renders the K2-cluster in the correct oxidation state for methyl attachment. There is also no 5'-dAH formation in the presence of only the SAM-module. This could be explained by a lack of a K2-bound methyl group that can undergo hydrogen atom abstraction by a 5'-dA• radical. A previous study has shown that methyl transfer does not occur when NifB is oxidized or reduced by a weak reductant, suggesting that the K-cluster needs to be poised in a particular redox state that renders its associated sulfides more nucleophilic for methyl transfer via an  $\text{S}\text{N}_2$ -type nucleophilic substitution (13). It is possible, therefore, that the K2 module needs the presence of at least the SAM-module to be able to accept the methyl group, a scenario highlighting the importance of cross-talk between the cluster modules during the cluster transformation process. Additionally, because the amounts of SAH and 5'-dAH formed in the absence of the K1 module are much lower than those in the presence of the K1 module, further coordination between all three cluster modules must be necessary to maximize the efficiency of cluster transformation.

The cluster transformation process requires structural rearrangements to allow the formation of an L-cluster and the subsequent transfer of the L-cluster from NifB onto the next biosynthetic apparatus, NifEN, along the cofactor assembly pathway. The structural rearrangement likely

requires the loss of Cys ligands to the K1- and K2-modules to facilitate L-cluster transfer to NifEN. Advanced spectroscopic and structural investigations are underway to reveal the unique radical SAM chemistry underscoring the complex biosynthetic mechanism of the nitrogenase cofactor.

## 2.5 Acknowledgments

The National Institutes of Health – National Institute of General Medical Sciences generously provided funding for this under award number GM67626 to Dr. Markus W. Ribbe and Dr. Yilin Hu.

I am grateful to Springer Nature for publishing the results described in this chapter (17) and allowing me to reuse portions in my dissertation.

Special thanks to Dr. Kazuki Tanifuji, who developed the cluster reconstitution method that made this work possible. I would also like to thank Dr. Caleb Hiller, Dr. Chi Chung Lee, and Dr. Martin T. Stiebritz, for their contributions to this research project.

## 2.6 References

1. Lancaster KM, Roemelt M, Ettenhuber P, Hu Y, Ribbe MW, Neese F, Bergmann U, DeBeer S. 2011. X-ray Emission Spectroscopy Evidences a Central Carbon in the Nitrogenase Iron-Molybdenum Cofactor. *Science* 334:974–977.
2. Spatzal T, Aksoyoglu M, Zhang L, Andrade SLA, Schleicher E, Weber S, Rees DC, Einsle O. 2011. Evidence for interstitial carbon in nitrogenase FeMo cofactor. *Science* 334:940.

3. Wiig JA, Hu Y, Lee CC, Ribbe MW. 2012. Radical SAM-Dependent Carbon Insertion into the Nitrogenase M-Cluster. *Science* 337:1672–1675.
4. Frey PA, Hegeman AD, Ruzicka FJ. 2008. The Radical SAM Superfamily. *Crit Rev Biochem Mol Biol* 43:63–88.
5. Broderick JB, Duffus BR, Duschene KS, Shepard EM. 2014. Radical S-Adenosylmethionine Enzymes. *Chemical Reviews* 114:4229.
6. Fay AW, Wiig JA, Lee CC, Hu Y. 2015. Identification and characterization of functional homologs of nitrogenase cofactor biosynthesis protein NifB from methanogens. *PNAS* 112:14829–14833.
7. Sickerman NS, Rettberg LA, Lee CC, Hu Y, Ribbe MW. 2017. Cluster assembly in nitrogenase. *Essays Biochem* 61:271–279.
8. Shah VK, Allen JR, Spangler NJ, Ludden PW. 1994. *In vitro* synthesis of the iron-molybdenum cofactor of nitrogenase. Purification and characterization of NifB cofactor, the product of NIFB protein. *J Biol Chem* 269:1154–1158.
9. Hu Y, Ribbe MW. 2016. Biosynthesis of the Metalloclusters of Nitrogenases. *Annual Review of Biochemistry* 85:455–483.
10. Wiig JA, Hu Y, Ribbe MW. 2011. NifEN-B complex of *Azotobacter vinelandii* is fully functional in nitrogenase FeMo cofactor assembly. *Proc Natl Acad Sci USA* 108:8623–8627.
11. Wilcoxon J, Arragain S, Scandurra AA, Jimenez-Vicente E, Echavarri-Erasun C, Pollmann S, Britt RD, Rubio LM. 2016. Electron Paramagnetic Resonance Characterization of Three Iron–Sulfur Clusters Present in the Nitrogenase Cofactor Maturase NifB from *Methanocaldococcus infernus*. *J Am Chem Soc.* 138:7468-71
12. Tanifuji K, Lee CC, Sickerman NS, Tatsumi K, Ohki Y, Hu Y, Ribbe MW. 2018. Tracing the ‘9th Sulfur’ of the Nitrogenase Cofactor via a Semi-Synthetic Approach. *Nat Chem* 10:568–572.
13. Wiig JA, Hu Y, Ribbe MW. 2015. Refining the pathway of carbide insertion into the nitrogenase M-cluster. *Nat Commun* 6:8034.
14. Allen RM, Chatterjee R, Ludden PW, Shah VK. 1995. Incorporation of Iron and Sulfur from NifB Cofactor into the Iron-Molybdenum Cofactor of Dinitrogenase. *J Biol Chem* 270:26890–26896.
15. George SJ, Igarashi RY, Xiao Y, Hernandez JA, Demuez M, Zhao D, Yoda Y, Ludden PW, Rubio LM, Cramer SP. 2008. EXAFS and NRVs Reveal that NifB-co, a FeMo-co Precursor, Comprises a 6Fe Core with an Interstitial Light Atom. *J Am Chem Soc* 130:5673–5680.

16. Guo Y, Echavarri-Erasun C, Demuez M, Jiménez-Vicente E, Bominaar EL, Rubio LM. 2016. The Nitrogenase FeMo-Cofactor Precursor Formed by NifB Protein: A Diamagnetic Cluster Containing Eight Iron Atoms. *Angew Chem Int Ed Engl* 55:12764–12767.
17. Rettberg LA, Wilcoxon J, Lee CC, Stiebritz MT, Tanifuji K, Britt RD, Hu Y. 2018. Probing the coordination and function of Fe<sub>4</sub>S<sub>4</sub> modules in nitrogenase assembly protein NifB. *Nature Communications* 9:1–8.
18. Landgraf BJ, Arcinas AJ, Lee K-H, Booker SJ. 2013. Identification of an Intermediate Methyl Carrier in the Radical SAM Methylthiotransferases, RimO and MiaB. *J Am Chem Soc* 135:15404–15416.

## **Chapter 3: Investigation of an Essential Nitrogen Ligand on NifB**

### 3.1 Introduction

In the previous chapter, three sets of Cys ligands—three Cys per set—for the three [Fe<sub>4</sub>S<sub>4</sub>] clusters in *Methanosarcina acetivorans* NifB (designated *MaNifB*) were identified, namely, the SAM- cluster (Cys<sup>50</sup>, Cys<sup>54</sup>, and Cys<sup>57</sup>), the K1-cluster (Cys<sup>30</sup>, Cys<sup>63</sup>, and Cys<sup>129</sup>) and the K2-cluster (Cys<sup>264</sup>, Cys<sup>274</sup>, and Cys<sup>277</sup>)(1). Further, the coexistence of SAM- and K2-clusters was established as a prerequisite for methyl transfer and hydrogen abstraction to occur and pinpointed the K2-cluster as the site for methyl attachment and the subsequent hydrogen abstraction from the methyl group by a 5'-dA• radical (1). Cysteine thiolates are the most common ligands to FeS clusters are cysteine thiolates, but some proteins use N or O ligands from amino acids (2). Pulse EPR techniques can probe these ligands to EPR active centers.

Here, we used pulse EPR techniques to detect a nitrogen atom that is the fourth ligand for the K1-cluster. This ligand is lost upon coupling between the K1- and K2-clusters into an L-cluster (1). This observation suggests an important role of the His/nitrogen ligand in generating the L-cluster, by either providing a release mechanism for the L-cluster onto the next biosynthetic apparatus or participating in the further deprotonation/dehydrogenation of the carbon radical to give rise to a central carbide.

We followed up with a combination of targeted mutagenesis of conserved His residues and pulse EPR spectroscopy to show that His<sup>43</sup> is the specific nitrogen ligand for the K1-cluster of *MaNifB*. The biochemical and EPR analyses demonstrate the essential role of His<sup>43</sup> in the formation of the nitrogenase cofactor core structure, although substitution of this residue with

Ala does not impact early steps of carbide insertion leading to the initial hydrogen atom abstraction of the K2-associated methyl group.

Moreover, XAS and EXAFS analyses reveal a shortened distance between the K1- and K2-clusters upon substitution of His<sup>43</sup> with Ala, and further processing of these clusters into an intermediate between the K- and L-clusters upon incubation with SAM. These results point a role of histidine-43 in structurally assisting the correct coupling between K1 and K2 and concurrently facilitating carbide formation via deprotonation of the initial carbon radical.

## 3.2 Materials and Methods

### 3.2.1 General Information

Unless otherwise specified, all chemicals were purchased from Sigma-Aldrich (St. Louis, MO) and Thermo-Fisher Scientific (Waltham, MA), and all experiments with proteins were performed under an Ar atmosphere using Schlenk techniques and/or in a glove box operating at <3 ppm O<sub>2</sub>.

### 3.2.2 Cell Growth and Protein Purification

*E. coli* strains expressing His-tagged *MaNifB*<sup>wt</sup> (strain YM114EE), *MaNifB*<sup>H28A</sup> (strain YM242EE), *MaNifB*<sup>H43A</sup> (strain YM244EE), *MaNifB*<sup>H219A</sup> (strain YM246EE), *MaNifB*<sup>K1</sup> (strain YM165EE) and *MaNifB*<sup>K1-H43A</sup> (strain YM307EE) were grown in 10-L batches in Difco LB medium containing 100 mg L<sup>-1</sup> ampicillin (BD Biosciences) in a BIOFLO 415 fermenter (New Brunswick Scientific) at 37

°C, with 200 rpm agitation and 10 L min<sup>-1</sup> airflow. When OD<sub>600</sub> reached 0.5, the temperature was lowered to 25 °C before the expression of the wildtype and variant *MaNifB* proteins was induced by the addition of 25 μM IPTG. Protein was expressed for 16 h before cells were harvested by centrifugation using a Thermo Fisher Scientific Legend XTR centrifuge. Subsequently, His-tagged *MaNifB* proteins were purified by immobilized metal affinity chromatography (IMAC) (3, 4).

### 3.2.3 Iron-Sulfur Cluster Reconstitution

As-isolated *MaNifB* contains some FeS-cluster species which must first be removed before reconstitution with synthetic [Fe<sub>4</sub>S<sub>4</sub>] clusters. The purified wildtype or variant *MaNifB* was treated with 20 mM bathophenanthroline disulfonate, an iron chelator, in a buffer containing 2 mM sodium dithionite (DT; Na<sub>2</sub>S<sub>2</sub>O<sub>4</sub>), 50 mM Tris-HCl (pH 8.0) and 500 mM NaCl, followed by incubation at room temperature for 1 h to remove the endogenous FeS clusters associated with the protein. Subsequently, this mixture was diluted with a buffer containing 50 mM Tris-HCl (pH 8.0) and loaded on a Q Sepharose column (GE Healthcare). The column was then washed with a buffer containing 2 mM DT, 50 mM Tris-HCl (pH 8.0) and 50 mM NaCl prior to elution of the *MaNifB* protein with a buffer containing 50 mM Tris-HCl (pH 8.0) and 500 mM NaCl. Dithionite was removed by running protein through a Sephadex G-25 (GE Healthcare) column equilibrated with 50 mM Tris-HCl (pH 8.0) and 10% glycerol. Reconstitution of the wildtype or variant *MaNifB* protein with synthetic [Fe<sub>4</sub>S<sub>4</sub>] clusters (designated [Fe<sub>4</sub>S<sub>4</sub>]<sup>Syn</sup>) (5) was carried out by adding a dimethylformamide (DMF) solution of synthetic [Fe<sub>4</sub>S<sub>4</sub>] cluster dropwise at a molar

ratio of 5:1 to the *MaNifB* protein in a buffer containing 20 mM  $\beta$ -mercaptoethanol and 50 mM Tris-HCl (pH 8.0), with continuous stirring on ice. After incubation on ice for 1 h, the reaction mixture was diluted with a buffer containing 2 mM DT and 50 mM Tris-HCl (pH 8.0) and loaded on a Q Sepharose column. The column was then washed with a buffer containing 2 mM DT, 50 mM Tris-HCl, and 50 mM NaCl prior to elution of the reconstituted *MaNifB* with a buffer containing 2 mM DT, 50 mM Tris-HCl (pH 8.0) and 500 mM NaCl. Reconstituted wildtype and variant *MaNifB* proteins were used in the iron determination, activity assays, EPR analysis, and XAS experiments described below.

### **3.2.4 Iron Determination**

Each protein sample was mixed with 100  $\mu$ L concentrated sulfuric acid ( $\text{H}_2\text{SO}_4$ ), and 100  $\mu$ L concentrated nitric acid ( $\text{HNO}_3$ ), and the mixture was heated at 250  $^\circ\text{C}$  for 30 min. This procedure was repeated until the mixture became colorless, followed by cooling of the mixture to room temperature and dilution of the mixture to a total volume of 10 mL with 2%  $\text{HNO}_3$  prior to sample analysis. The iron concentrations of the wild-type and variant *MaNifB* proteins were determined by inductively coupled plasma optical emission spectroscopy (ICP-OES) analysis using a Thermo Scientific iCAP7000. Calibration curves were created by making standard solutions from dilutions of a 1 mg  $\text{mL}^{-1}$  stock solution of elemental iron (Inorganic Ventures, Christiansburg, VA).

### 3.2.5 M-Cluster Maturation Assay

The cofactor maturation assay contained, in a total volume of 1.0 mL, 25 mM Tris-HCl (pH 8.0), 20 mM DT, 3.5 mg FeS-reconstituted wildtype or variant *MaNifB*, 10 mM SAM, 2 mg  $\Delta$ nifB *Azotobacter vinelandii* (*Av*) NifEN, 1.4 mg NifH, 0.8 mM ATP, 1.6 mM MgCl<sub>2</sub>, 10 mM creatine phosphate, 8 units creatine phosphokinase, 0.3 mM homocitrate, 0.3 mM Na<sub>2</sub>MoO<sub>4</sub> and 0.5 mg  $\Delta$ nifB *Av*NifDK. This mixture was incubated at 30 °C for 30 min before it was examined for C<sub>2</sub>H<sub>2</sub> reduction activity (3, 4).

### 3.2.6 SAM Cleavage Assay

The SAM cleavage assay contained, in a total volume of 0.3 mL, 25 mM Tris-HCl (pH 8.0), 5% glycerol (v/v), 40  $\mu$ M wildtype or variant *MaNifB*, and 0.3 mM SAM. Assays were incubated at 25 °C for 60 min with intermittent mixing before they were terminated by filtration through Amicon Ultra 30,000 MWCO centrifugal filters. Samples were then supplemented by trifluoroacetic acid (TFA) to a concentration of 0.14% before being analyzed by a Thermo Scientific Dionex Ultimate 3000 UHPLC system equipped with an Acclaim 120 C18 column (4.6  $\times$  100 mm, 5- $\mu$ m particle size). The flow rate of buffer was 0.5 mL min<sup>-1</sup>, and the column was kept at 30 °C. The column was equilibrated with 98% buffer A (50 mM KH<sub>2</sub>PO<sub>4</sub>, pH 6.6) and 2% buffer B (100% methanol) before each injection of a 100- $\mu$ L sample. After sample injection, a linear gradient of 2–60% buffer B was applied over 20 min, followed by 8 min of isocratic flow with 60% buffer B and a linear gradient of 60–2% buffer B over 4 min. The elution of products was

monitored at a UV wavelength of 254 nm. After each run, the column was equilibrated for 5 min with 2% buffer B before the injection of the next sample.

### 3.2.7 Methanethiol Assay

Detection of *MaNifB*-dependent production of methanethiol was performed (4). First, excess DT was removed from wildtype and variant *MaNifB* via gel filtration with Sephadex G-25 fine resin that was equilibrated with a buffer containing 25 mM Tris-HCl (pH 8.0). Immediately following the removal of excess reductant, 40 nmol of *MaNifB* was added to a sealed 300- $\mu$ L glass vial that contained 400 nmol SAM in a total volume of 100  $\mu$ L. These 100- $\mu$ L reactions were then incubated for 30 min at 25 °C before being quenched by 25  $\mu$ L of 1 M HCl. To observe the formation of the volatile methanethiol, the acid-quenched samples were incubated at 60 °C for 15 min and equilibrated to room temperature for 10 min before the entire headspace was injected by a gas-tight syringe onto a GC–MS (Thermo-Fisher Scientific Trace 1300 GC connected to a Thermo-Fisher Scientific ISQ QD single quadrupole mass spectrometry) with a Restek Rxi-1ms column (30 m, 0.32 mm ID, 4.0  $\mu$ m df). The GC inlet and oven temperatures were maintained at 30 °C, while the mass spectrometry transfer line and ion source were maintained at 250 °C. Total ion chromatograms were generated under SIM conditions in electron ionization mode, and methanethiol was detected at an  $m/z$  ratio of 47. The base peaks were selected based on the characterization of standard samples (Sigma-Aldrich) under full scan conditions and comparison to those reported in the National Institute of Standards and Technology database.

### 3.2.8 Continuous-Wave Electron Paramagnetic Resonance (CW-EPR) Analysis

Sample preparation was carried out in a Vacuum Atmospheres glove box with less than 1 ppm O<sub>2</sub> and flash-frozen in liquid nitrogen before analysis. The dithionite-reduced samples were prepared by incubating 50 μM wildtype or variant *MaNifB* with 40 mM SAM for 15 min, followed by re-isolation of *MaNifB* into a buffer containing 50 mM Tris-HCl (pH 8.0), 500 mM NaCl, and 2 mM sodium dithionite (DT). The indigo disulfonate (IDS)-oxidized samples were prepared by incubating the re-isolated *MaNifB* with excess IDS for 5 min, followed by removal of excess IDS using a Sephadex G-25 desalting column. The DT-reduced or IDS-oxidized *MaNifB* sample was then concentrated to 15 mg mL<sup>-1</sup>, followed by the transfer of the sample into EPR tubes. The samples were then flash-frozen and stored in liquid nitrogen. CW-EPR spectra were recorded by an ESP 300 E<sub>z</sub> spectrophotometer (Bruker) interfaced with an ESR-9002 liquid-helium continuous-flow cryostat (Oxford Instruments) using a microwave power of 5 mW (IDS-oxidized samples) or 50 mW (DT-reduced samples), a gain of 5 × 10<sup>4</sup>, a modulation frequency of 100 kHz, and a modulation amplitude of 5 G. Five scans were recorded for each sample in perpendicular mode at 20 K (IDS-oxidized samples) or 10 K (DT-reduced samples) using a microwave frequency of 9.62 GHz.

### 3.2.9 Pulse EPR Analysis

For pulse EPR analysis, reaction mixtures were transferred into 4 mm (X-band)- or 2 mm (Q-band)-diameter tubes, flash-frozen as above, and stored in liquid nitrogen after freezing. All pulse EPR studies were carried out at the UC Davis CalEPR center, using a Bruker EleXsys E580

pulse EPR spectrometer equipped with an Oxford-CF935 liquid-helium cryostat and an ITC-503 temperature controller. Pulse data were collected using a Bruker MS5 probe (X-band) or an R.A. Isaacson-designed cylindrical TE011 resonator (Q-band) (6) adapted for pulse EPR in an Oxford Instruments CF935 cryostat. Two-pulse field swept (2PFS) EPR spectra were collected using the sequence  $\pi/2$ - $\tau$ - $\pi$ - $\tau$ -echo, stepping the field after each point. Three-pulse ESEEM spectra were collected using the pulse sequence  $\pi/2$ - $\tau$ - $\pi/2$ - $T$ - $\pi/2$ - $\tau$ -echo, where the delay time,  $T$ , was increased by 16 ns steps. ESEEM spectra were recorded at 10 K,  $\tau = 128$ –144 ns (values chosen to minimize proton modulations to the spectra),  $\pi/2 = 12$  ns, and a microwave frequency of 9.2465 GHz (*MaNifB<sup>L</sup>*) or 9.3366 GHz (all other samples). Spectra were collected near the  $g_2$  value (spectra maxima) for each of the samples (*MaNifB<sup>wt</sup>*: 343 mT; *MaNifB<sup>K1</sup>*: 343 mT, and *MaNifB<sup>K2</sup>*: 344 mT, and *MaNifB<sup>L</sup>*: 340 mT). Hyperfine sub-level-correlation (HYSCORE) spectroscopy was performed using the pulse sequence:  $\pi/2$ - $\tau$ - $\pi/2$ - $T_1$ - $\pi$ - $T_2$ - $\pi/2$ - $\tau$ -echo<sup>48</sup>. In the HYSCORE experiment,  $T_1$  and  $T_2$  were incremented by 20 ns steps to produce a two-dimensional spectrum. HYSCORE spectra were recorded at 10 K,  $\tau = 128$ –132 ns, and  $\pi/2 = 12$  ns. Spectral processing and simulations were performed using the EasySpin 4.0 toolbox or EasySpin 5.2.27 toolbox in Matlab R2017b49, or R2019a, respectively. All spin quantification was carried out using the program SpinCount50. Variable power EPR spectra were collected for *MaNifBSAM*, *MaNifB<sup>K1</sup>*, and *MaNifB<sup>K2</sup>* at 20 K to determine the extent of saturation. All *MaNifB* samples were found to have a linear response to the microwave power across all values tested. Samples of Cu(II) EDTA between 0.1 mM and 0.5 mM were used as standards for the  $S = 1/2$  signals observed for *MaNifB* variants, at microwave powers between 0.5 and 1 mW. The slope of each spectrum was baseline corrected using the program tools in SpinCount. The double

integral was measured across the  $S = 1/2$  signal for each spectrum. The integrations were compared between the Cu(II)EDTA standard and the *MaNifB* samples to determine the spin concentration.

### 3.2.10 X-ray Absorption Spectroscopy (XAS) Analysis

The XAS samples were prepared the same way as the EPR samples (see above). The sample concentrations were  $50 \text{ mg mL}^{-1}$ . Fe K-edge X-ray absorption spectra were collected on SSRL beamline 7-3 using a 30-element solid-state Ge detector (Canberra) with a SPEAR3 storage ring current of  $\sim 500 \text{ mA}$  at an energy of  $3.0 \text{ GeV}$ . The BL7-3 optics consists of a flat, bent, harmonic rejection vertically collimating Rh-coated Si M0 mirror and liquid nitrogen cooled double crystal Si(220) monochromator. A total of 7 and 6 scans, respectively, were collected for *MaNifB*<sup>H43A</sup> before and after incubation with SAM (designated *MaNifB*<sup>H43A</sup> and *MaNifB*<sup>H43A</sup>/SAM). All scans were taken between 6882 and 8000 eV at  $\sim 10 \text{ K}$  using an Oxford Instruments CF1208 continuous flow liquid-helium cryostat using a closed-cycle cooled He gas loop. An iron foil was placed in the beam pathway prior to the ionization chamber  $I_0$  and scanned concomitantly for energy calibration, with the first inflection point of the edge assigned to 7112.0 eV. A Soller slit with a  $3 \mu\text{m}$  Mn filter was used to increase the signal-to-noise ratio of the spectra.

Photoreduction was monitored by scanning the same spot on the sample twice and comparing the first derivative peaks associated with the edge energy during data collection. The detector channels from the scans were examined, calibrated, and averaged using EXAFSPAK (7) and then processed for EXAFS analysis using PYSPLINE (8) to extract  $\chi(k)$ . PYSPLINE was used to subtract a

second-order background from the entire range of data and subsequently generate a spline function to model background absorption through the EXAFS region. A four-region spline was chosen with 2, 3, 3 order polynomials over the post edge region, and the data were normalized to have an edge jump of 1.0 at 7130 eV. Following a modified data analysis protocol (9), the Fe K-edge EXAFS data for the clusters associated with  $MaNiF^{H43A}$  and  $MaNiF^{H43A}/SAM$  were generated by subtracting the k-weighted EXAFS data,  $\chi(k)$ , of  $MaNiF^{SAM}$  (an  $MaNiF$  variant carrying only the SAM-cluster (1)) from the  $\chi(k)$  of the samples in a 1:2 ratio on the basis of the proportionate iron quantity for each cluster species (i.e., 4 Fe for the SAM-cluster and 8 Fe for the K-clusters). Theoretical phase and amplitude parameters for a given absorber–scatterer pair were calculated using FEFF 8.40 (10) and subsequently applied to the nonlinear least-squares Opt fitting program of the EXAFSPAK package during curve fitting. Parameters for each species were calculated using an appropriate model derived from either the crystal structure of the M-cluster in  $NiFDK$  (PDB code 3U7Q) (11), where the Mo atom was exchanged for an Fe atom or from the  $[Fe_4S_4]$  cluster in  $NiFH$  (PDB code 1G5P) (12) because there are no available crystal structures of  $MaNiF$ . In all analyses, the coordination number of a given shell (N) was a fixed parameter and was varied iteratively in integer steps, whereas the bond lengths (R) and mean-square deviation ( $\sigma^2$ ) could freely float. The estimated uncertainties in R,  $\sigma^2$ , and N are 0.02 Å,  $0.1 \times 10^{-3} \text{ \AA}^2$ , and 20%, respectively. The amplitude reduction factor  $S_0$  was fixed at 1.0 for the Fe K-edge data, whereas the edge-shift parameter  $\Delta E_0$  could float as a single value for all shells. Thus, in any given fit, the number of floating parameters was typically equal to  $2 \times$  the number of shells + 1. The goodness of fit (GOF) parameters were calculated as follows:

$$F = \sqrt{\sum k^6 (\chi_{exp} - \chi_{exp})^2} \quad (1)$$

$$F = \sqrt{\sum k^6 (\chi_{exp} - \chi_{exp})^2 / \sum k^6 (\chi_{exp})^2} \quad (2)$$

The Fe K-edge data were analyzed with a k range of 2–11.2 Å<sup>-1</sup> (ΔR = 0.17 Å) to allow comparison between previously reported data (13), although the data could be analyzed with higher resolution with a k range of 2–14 Å<sup>-1</sup> for *MaNifB*<sup>H43A</sup> and *MaNifB*<sup>H43A</sup>/SAM. The pre-edge analysis was performed on the Fe K-edge fluorescence data normalized to have an edge jump of 1.0 at 7130 eV in PYSPLINE. The pre-edge features were fit as described elsewhere (14) between 7108 and 7117 eV using the Fityk (15) program with pseudo-Voigt functions composed of 50:50 Gaussian/ Lorentzian functions.

### 3.3 Results and Discussion

#### 3.3.1 Observation of N Coordination to K1-Cluster

Additional ligands were probed by pulse EPR. The ligation patterns of the K1- and K2-modules were further explored by pulse EPR spectroscopy, using the one-dimensional electron spin echo envelope modulation (ESEEM) and two-dimensional hyperfine sub-level correlation (HYSCORE) pulse EPR techniques. The presence of nitrogen coupling—previously reported for a NifB homolog from a different methanogenic organism (16)—was examined in *MaNifB*<sup>K1</sup> and *MaNifB*<sup>K2</sup> to assign the nitrogen ligand to a specific cluster module. Interestingly, the three-

pulse ESEEM data of *MaNifB*<sup>wt</sup> and *MaNifB*<sup>K1</sup> reveal modulations from nitrogen coupled to the K1-cluster (Fig. 3.1 a, blue trace). HYSCORE spectra were collected at each of the principal *g* values for the K1 module to enable reliable interpretation of the <sup>14</sup>N hyperfine and quadrupole couplings (Fig. 3.1 b). The experimental data are simulated exceedingly well with a <sup>14</sup>N hyperfine coupling tensor (in MHz) of **A** = [2.9 2.9 5.6] and a nuclear quadrupole coupling of  $e^2Qq/h = -2.1$  MHz and  $\eta = 0.4$  (Fig. 3.1 c).

For a nitrogen directly coordinated to a FeS cluster, an isotopic hyperfine of **A**<sub>iso</sub> = 3–7 MHz and a dipolar coupling of T = 0.9–1 MHz are expected. In contrast, a nitrogen that is near but not coordinated to the cluster, such as a backbone amide, would have an **A**<sub>iso</sub> ~1 MHz. The data suggest the nitrogen measured (**A**<sub>iso</sub><sup>K1</sup> = 3.8 MHz, TK1 = 0.9 MHz) is directly coordinated to the K1 module (17–26). Next, the nuclear quadrupole coupling ( $e^2Qq/h$ ) values of <sup>14</sup>N nuclei were compared, which report on the electric field gradient of the <sup>14</sup>N nucleus and are sensitive to the environment of the nitrogen that is directly bound to an Fe center. While there are numerous EPR measured hyperfine, and quadrupole couplings from nitrogenous ligands to Fe sites, a majority of them are from histidine ligated sites, including those found in the various Rieske-type [Fe<sub>2</sub>S<sub>2</sub>] clusters ( $e^2Qq/h = 1.9$ – $3.5$  MHz) where the cluster contains two His ligands, in the mitoNEET [Fe<sub>2</sub>S<sub>2</sub>] clusters ( $e^2Qq/h = -2.47$  MHz) which contain only a single His ligand, and in myoglobin ( $e^2Qq/h = -2.24$  MHz) where the His ligand is axial to the porphyrin-bound Fe center (18, 19, 21–23, 23–25, 27). The only reported hyperfine, and quadrupole coupling from a non-histidine ligand is found in the radical SAM enzyme BioB, where Arg<sup>260</sup> is coordinated to a [Fe<sub>2</sub>S<sub>2</sub>] cluster ( $e^2Qq/h = 2.6$ – $2.8$  MHz)<sup>29</sup>. The quadrupole coupling that was measured ( $e^2Qq/h = -2.1$  MHz) is lower than the reported value for Arg and is in the range of values for a His

coordinated cluster; therefore, the fourth ligand was assigned to the K1 module as histidine.  $^{14}\text{N}$  coupling to the K2-cluster (in *MaNifB*<sup>K2</sup>) and the L-cluster (in *MaNifB*<sup>L</sup>, or SAM-treated *MaNifB*<sup>wt</sup>, wherein the K1- and K2-modules are fused into an 8Fe L-cluster upon addition of SAM) was not detected by the same EPR techniques (Fig. 3.1 a, red and green traces). However, the observed absence of nitrogen coupling to the K2 module cannot be used to determine if the fourth Fe site of this cluster is open, is occupied by a coordinated water, or is ligated by an amino acid such as Asp or Glu. The absence of nitrogen ligation to the L-cluster, on the other hand, is particularly interesting, as it suggests a conformational rearrangement upon coupling of the K1- and K2-modules into an 8Fe L-cluster.

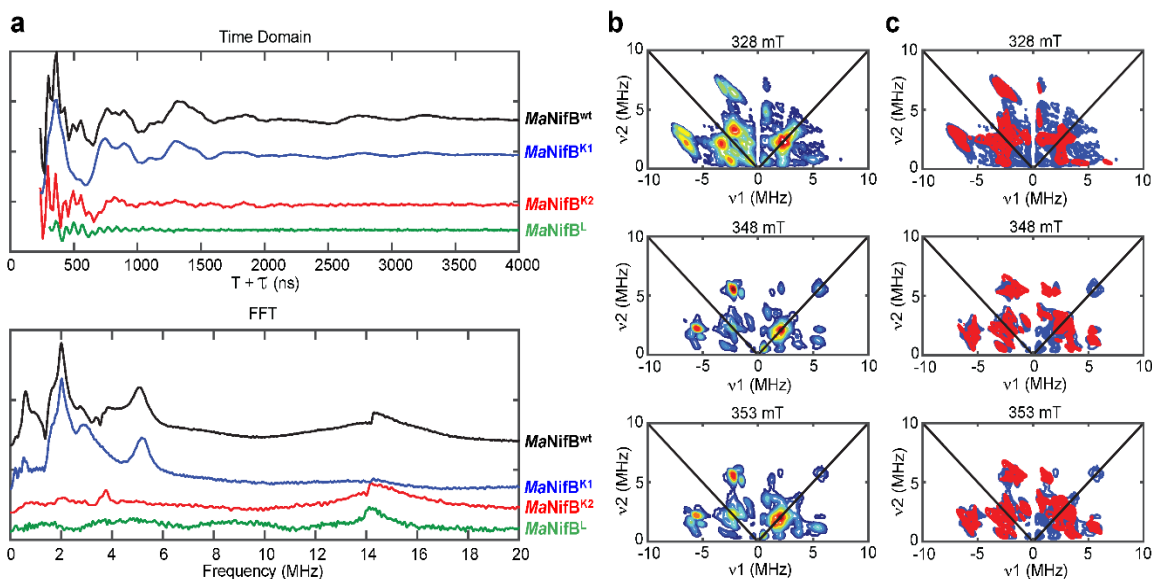


**Figure 3.1 Pulse EPR analysis of *MaNifB*.** **a** Three-pulse ESEEM spectra of dithionite-reduced *MaNifB*<sup>wt</sup> (black), *MaNifB*<sup>K1</sup> (blue), *MaNifB*<sup>K2</sup> (red), and *MaNifB*<sup>L</sup> (green). The time-domain spectra of *MaNifB*<sup>wt</sup> and *MaNifB*<sup>K1</sup> have modulations from <sup>14</sup>N that appear as peaks in the fast Fourier transformed (FFT) spectra between 1 and 8 MHz. The sharp modulations between 250 and 500 ns in the time domain and the resulting broad peak near 14 MHz in the FFT are from nearby weakly coupled protons. **b** HYSORE spectra of the dithionite-reduced *MaNifB*<sup>K1</sup> taken at 328, 348, and 353 mT. **c** The HYSORE data (blue) can be simulated (red) with a single <sup>14</sup>N nucleus, with a hyperfine coupling tensor **A** (in MHz) = [2.9 2.9 5.6] and a quadrupole coupling of  $e^2Qq/h = -2.1$  MHz and  $\eta = 0.4$ . Three-pulse ESEEM spectra were recorded at 10 K,  $\tau = 128$ –144 ns (values chosen to minimize proton modulations to the spectra),  $\pi/2 = 12$  ns, and a microwave frequency of 9.3366 GHz (*MaNifB*<sup>wt</sup>, *MaNifB*<sup>K1</sup>, *MaNifB*<sup>K2</sup>) or 9.2465 GHz (*MaNifB*<sup>L</sup>). Spectra were collected near the  $g_2$  value (spectra maxima) for each of the samples (*MaNifB*<sup>wt</sup>: 343 mT; *MaNifB*<sup>K1</sup>: 343 mT, and *MaNifB*<sup>K2</sup>: 344 mT, and *MaNifB*<sup>L</sup>: 340 mT). *MaNifB*<sup>K1</sup> HYSORE spectra were recorded at 10 K,  $\tau = 128$ –132 ns, and  $\pi/2 = 12$  ns.

### 3.3.2 Identification of an Essential Nitrogen Ligand

Sequence analysis of *MaNifB* revealed the presence of three highly conserved His residues, His<sup>28</sup>, His<sup>43</sup>, and His<sup>219</sup>, which could potentially serve as the nitrogen ligand for the K1-cluster on *MaNifB* ((Fig. 3.2). Based on this analysis, three *MaNifB* variants were heterologously expressed in *Escherichia coli*, designated *MaNifB*<sup>H28A</sup>, *MaNifB*<sup>H43A</sup>, and *MaNifB*<sup>H219A</sup>, respectively, each variant has one of the conserved His residues substituted with Ala.

**1** MPEENQPIKEKNNGPILGEELLRKISEHPCYDKNAQHKYG  
**41** RILAVAPACNIQCNFVREFDCVNESRPGVTSKVLTPEE  
**81** ALEKTKQILAEYPFYIKVVAIAGPGDPLANDETFETFELIR  
**121** NEFPEITLCMSTNGLMLPEKLPEILRTGVSTLTVTVNAID  
**161** PEIQAKIVDHI FYHGKVYKGV EAAKI QIKNQLDGIKAAID  
**201** AGIVVKVNTVLI PGINDKH IIEIAKKLNELGVYIMNV MPL  
**241** INQGAFADLEPPTPEERKAVQEAEPYVMQMRHCRQCRAD  
**281** AYGLLAQDMSQMSEERRKVIKIQT KEDMEKARAVLEKNGK  
**321** KEA

**Figure 3.2 The primary sequence of *MaNifB*.**

Conserved His residues from 45 diazotrophic organisms (4) are highlighted in gray. The Cys residues that ligate to the K1- (blue), K2- (orange), and SAM-modules (red) are also highlighted.

Upon FeS reconstitution, *MaNifB*<sup>H28A</sup>, *MaNifB*<sup>H43A</sup>, and *MaNifB*<sup>H219A</sup> have Fe contents comparable to that of *MaNifB*<sup>wt</sup>, indicating that each contains three [Fe<sub>4</sub>S<sub>4</sub>] clusters (i.e., the SAM-, K1- and K2-clusters) per protein (Fig. 3.3 a). Each variant also has a composite S = ½ CW-EPR signal in perpendicular mode when treated with dithionite (Fig. 3.3 b). Thus, a loss of the His ligand does not seem to impact the ability of *MaNifB* to ligate any of the three [Fe<sub>4</sub>S<sub>4</sub>] clusters, likely due to the 3-Cys coordination of these clusters that is sufficient to secure them in place.

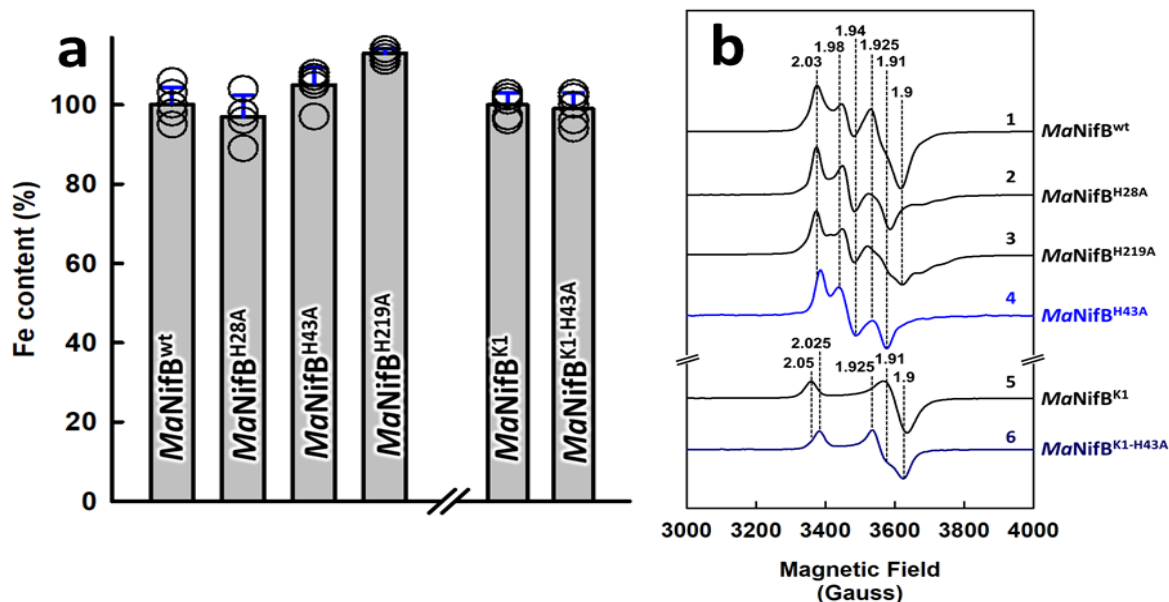


**Figure 3.3** Iron content and EPR spectra of dithionite-reduced *MaNifB* proteins. **a**

The Fe contents of *MaNifB*<sup>wt</sup> (11.9 + 1.1 mol Fe/mol protein) and *MaNifB*<sup>K1</sup> (3.9 + 0.1 mol Fe/mol protein) are set to 100% and compared with the Fe contents of their respective variant forms. The metal analysis was performed five times independently (n=5 independent samples), and data are shown as mean + S.D. Experimental details for iron determination are described in Section 3.2.4. **b** Shown are the CW-EPR spectra of *MaNifB*<sup>wt</sup> (1), *MaNifB*<sup>H28A</sup> (2), *MaNifB*<sup>H219A</sup> (3), *MaNifB*<sup>H43A</sup> (4), *MaNifB*<sup>K1</sup> (5) and *MaNifB*<sup>K1-H43A</sup> (6) in the dithionite-reduced state. The EPR analysis was performed three times independently (n=3 independent samples), and representative results are shown. All protein samples have a concentration of 15 m L<sup>-1</sup>. The spectra were recorded at 50 mW and 10 K. The g values are indicated (dashed vertical lines)

Three-pulse electron spin echo envelope modulation (3P-ESEEM) was again used to assess whether a nitrogen ligand is still present in these *MaNifB* variants. *MaNifB*<sup>wt</sup> shows deep modulations in the time domain of the ESEEM spectrum (Fig. 3.4 a, trace 1) and corresponding intensity between 0 and 6 MHz in the FFT (Fig. 3.4 b, trace 1), which were previously assigned to the hyperfine and quadrupole couplings of a cluster-ligated <sup>14</sup>N nucleus (1). Similar modulations and intensities are present in the ESEEM spectrum and FFT of *MaNifB*<sup>K1</sup>, a variant carrying only the K1-cluster but no SAM- and K2-clusters (because of substitutions of the Cys ligands of the SAM- and K2-clusters with Ala (1)), affirming the previous assignment of the nitrogen ligand to the K1-cluster (Fig. 3.4 a, b, trace 5). While similarly deep modulations and intensities are observed in the ESEEM spectra and FFTs of *MaNifB*<sup>H28A</sup> and *MaNifB*<sup>H219A</sup> (Fig. 3.4

a, b, traces 2, 3), these features are clearly absent from the ESEEM spectrum and FFT of *MaNifB*<sup>H43A</sup> (Fig. 3.4 a, b, trace 4), suggesting His<sup>43</sup> as the nitrogen ligand for the K1-cluster. To seek further support for this assignment, *MaNifB*<sup>K1-H43A</sup>— another *MaNifB* variant carrying only the Cys ligands of K1 along with the substitution of His<sup>43</sup> with Ala—was heterologously expressed in *E. coli*. The purified *MaNifB*<sup>K1-H43A</sup> demonstrates the same subunit composition as *MaNifB*<sup>K1</sup>, as well as the same Fe content that is consistent with the presence of one [Fe<sub>4</sub>S<sub>4</sub>] cluster (i.e., the K1-cluster) per protein upon FeS reconstitution (Fig. 3.3 a). However, contrary to *MaNifB*<sup>K1</sup> (Fig. 3.4 a, b, trace 5), *MaNifB*<sup>K1-H43A</sup> does not show deep modulations and intensities in its ESEEM spectrum and FFT (Fig. 3.4 a, b, trace 6), firmly establishing His<sup>43</sup> as the nitrogen ligand that specifically coordinates the K1- cluster.

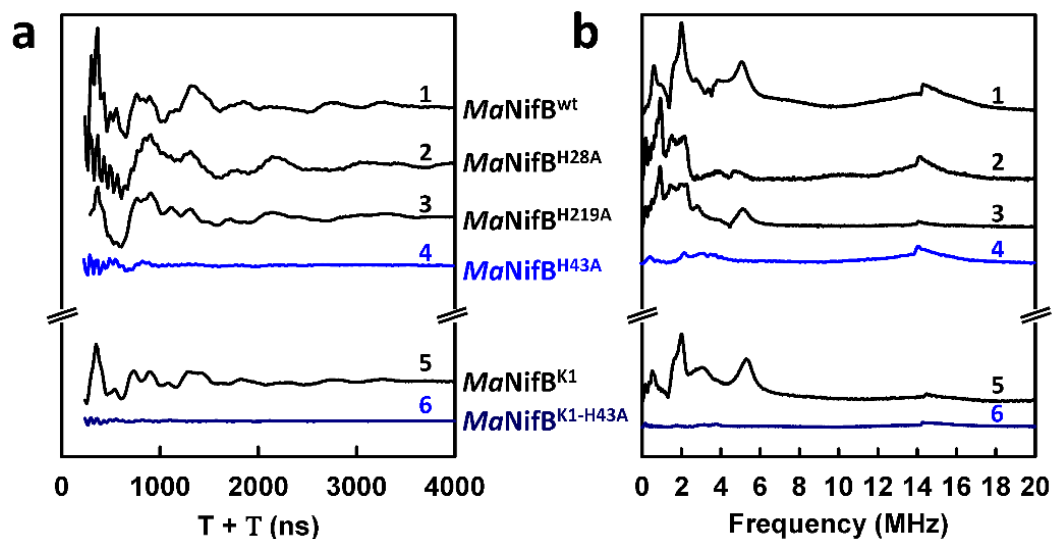


**Figure 3.4** Three-pulse ESEEM spectra of dithionite-reduced *MaNifB* proteins. **a** Time-domain and **(b)** fast Fourier transformed (FFT) spectra of *MaNifB*<sup>wt</sup> (1), *MaNifB*<sup>H28A</sup> (2), *MaNifB*<sup>H219A</sup> (3), *MaNifB*<sup>H43A</sup> (4), *MaNifB*<sup>K1</sup> (5) and *MaNifB*<sup>K1-H43A</sup> (6). The time-domain spectra of the His-ligand containing samples (i.e., 1, 2, 3, and 5) have modulations from <sup>14</sup>N that appear as peaks in the fast Fourier transformed (FFT) spectra between 1 and 6 MHz. The sharp modulations between 250 and 500 ns in the time domain and the resulting broad peak near 14 MHz in the FFT are from nearby weakly coupled protons. The ESEEM spectra were recorded at 10 K,  $\tau = 128\text{--}144$  ns,  $\pi/2 = 12$  ns, and 9.3366 GHz. The experiment was performed three times independently ( $n = 3$  independent samples), and representative results are shown in the figure. All protein samples have a concentration of 15 mg mL<sup>-1</sup>.

### 3.3.3 Function of His<sup>43</sup> in L-Cluster Maturation

Continuous-wave (CW) EPR analysis provided the first insights into the function of His<sup>43</sup> in the cofactor core assembly process. Consistent with the coupling and rearrangement of the K1- and K2-clusters into an L-cluster, the L-cluster-specific,  $g = 1.94$  signal (3–5) is observed in the spectra of *MaNifB*<sup>wt</sup>, *MaNifB*<sup>H28A</sup>, and *MaNifB*<sup>H219A</sup> upon incubation of these proteins with SAM (Fig. 3.5 a, traces 1–3). In contrast, the  $g = 1.94$  signal is absent from the spectrum of *MaNifB*<sup>H43A</sup> following the same treatment, suggesting a lack of K- to L-cluster transformation on this protein after incubation with SAM (Fig. 3.5 a, trace 4). In support of this assignment, the SAM-treated *MaNifB*<sup>wt</sup>, *MaNifB*<sup>H28A</sup>, and *MaNifB*<sup>H219A</sup> can be used as M-cluster sources for the subsequent reconstitution and activation of apo-NifDK in an in vitro assay. In contrast, the SAM-treated *MaNifB*<sup>H43A</sup> cannot support the reconstitution and activation of apo-NifDK in the same assay (Fig. 3.5 b). Interestingly, the activity of *MaNifB*<sup>H28A</sup> in this assay is ~41% less than *MaNifB*<sup>wt</sup>, suggesting a possible involvement of His28 in the K- to L-cluster conversion. H<sup>28</sup> is close to one of the Cys ligands (Cys<sup>30</sup>) of the K1-cluster in the primary sequence (Fig. 3.2) and, consequently, the tertiary structure of NifB. More importantly, the abolished activity of *MaNifB*<sup>H43A</sup> in the K- to L-cluster transformation points to a critical role of His<sup>43</sup> in coupling the K1- and K2- clusters into an 8Fe L-cluster.

To further explore the role of His<sup>43</sup> in this process, high-performance liquid chromatography (HPLC) was performed to examine the products generated upon incubation of *MaNifB*<sup>H43A</sup> with SAM. Like *MaNifB*<sup>wt</sup>, *MaNifB*<sup>H28A</sup>, and *MaNifB*<sup>H219A</sup>, and *MaNifB*<sup>H43A</sup> can all cleave SAM into S-adenosyl-L-homocysteine (SAH) and 5'-deoxyadenosine (5'-dAH) (Fig. 3.6 a,b, traces 1-4). Also, as observed in the cases of *MaNifB*<sup>wt</sup>, *MaNifB*<sup>H28A</sup>, and *MaNifB*<sup>H219A</sup> (Fig. 3.6 c, traces 1–3), the formation of methanethiol is detected upon acid quench of an incubation mixture of *MaNifB*<sup>H43A</sup> and SAM (Fig. 3.6 c, trace 4). This observation is not particularly surprising because previous results demonstrated that SAH, 5'-dAH, and methanethiol could be generated if both

SAM- and K2-clusters are present, even in the absence of the K1-cluster. The fact that substitution of the K1-specific ligand, His<sup>43</sup>, with Ala does not impact the reactivities associated with the

SAM- and K2-clusters is consistent with this observation and places the perturbation of the K- to L-cluster conversion by this substitution after the hydrogen atom abstraction from the K2-associated methyl group.

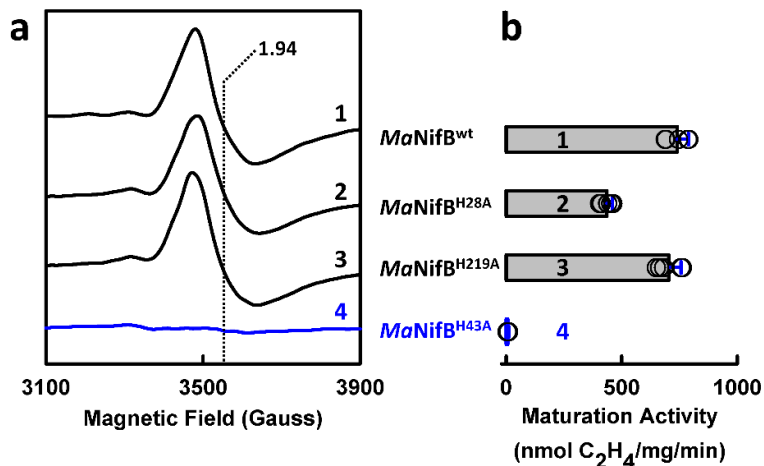


**Figure 3.5 Conversion of L-cluster to M-cluster on *MaNifB* proteins.** **a** EPR spectra of IDS-oxidized *MaNifB*<sup>wt</sup> (1), *MaNifB*<sup>H28A</sup> (2), *MaNifB*<sup>H219A</sup> (3), and *MaNifB*<sup>H43A</sup> (4) upon addition of SAM. The formation of the L-cluster was monitored by the appearance of an L-cluster-specific  $S = 1/2$  signal at  $g = 1.94$  (dashed vertical line). All protein samples have a concentration of  $15 \text{ mg mL}^{-1}$ . The EPR spectra were recorded at 5 mW and 20 K. **b** M-cluster maturation activity of *MaNifB*<sup>wt</sup> (1), *MaNifB*<sup>H28A</sup> (2), *MaNifB*<sup>H219A</sup> (3), and *MaNifB*<sup>H43A</sup> (4). The activity of M-cluster maturation was determined based on the C<sub>2</sub>H<sub>2</sub>-reducing activity of reconstituted NifDK, using SAM-treated *MaNifB* proteins as the M-cluster sources. The EPR analysis was performed three times independently ( $n = 3$  independent samples), and representative results are shown in (a). The maturation assay was performed five times independently ( $n = 5$  independent samples), and data are presented as mean  $\pm$  S.D. (b). See Section 3.2.5 for the detailed composition of maturation assays.

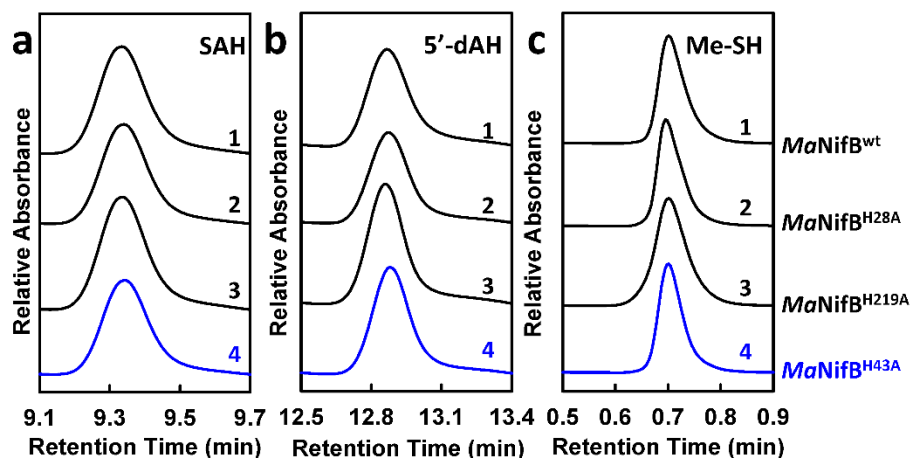


**Figure 3.6 Functional properties of *MaNifB* proteins.** **a, b** HPLC elution profiles of SAH (a) and 5'-dAH (b) upon incubation of SAM with *MaNifB*<sup>wt</sup> (1), *MaNifB*<sup>H28A</sup> (2), *MaNifB*<sup>H219A</sup> (3), and *MaNifB*<sup>H43A</sup> (4). **c** GC analyses of methanethiol (Me-SH) formation upon acid quenching of incubation mixtures containing SAM and *MaNifB*<sup>wt</sup> (1), *MaNifB*<sup>H28A</sup> (2), *MaNifB*<sup>H219A</sup> (3), and *MaNifB*<sup>H43A</sup> (4). All products were identified using standards (28, 29). The HPLC (a, b) and GC (c) experiments were each performed three times independently (n = 3 independent samples), and representative results are shown in the figure. The protein and SAM concentrations are 0.4 mM and 4 mM, respectively, in (a, b); and 40  $\mu$ M and 0.3 mM, respectively, in (c). See Section 3.2.6 and 3.2.7 for detailed compositions of these assays.

### 3.3.4 Roles of His<sup>43</sup> in Cluster Transformation

X-ray absorption spectroscopy (XAS)/extended x-ray absorption fine structure (EXAFS) analysis provided further insights into the role of His<sup>43</sup> in L-cluster maturation. XAS/EXAFS analysis has proven to be a valuable tool for obtaining structural information of the cluster species related to the function and assembly of nitrogenase. Previous studies of the wildtype and variant *MaNifB* proteins have established XAS/EXAFS parameters that can be used in combination with the EPR and biochemical data to conclusively assign cluster species and monitor cluster transformation in this protein.

The x-ray absorption near-edge structure (XANES) data reveal a K-edge energy for *MaNifB*<sup>H43A</sup> similar to that for *MaNifB*<sup>wt</sup> before or after incubation with SAM (Fig. 3.7 a), suggesting a similar

sulfur-rich environment in all these protein species (13). The pre-edge feature of  $\text{MaNifB}^{\text{H43A}}$  is also similar in intensity to that of  $\text{MaNifB}^{\text{wt}}$  before incubation with SAM; however, its amplitude does not increase as much as that of  $\text{MaNifB}^{\text{wt}}$  upon incubation with SAM (Table 3.1), suggesting that the transition metal center in SAM-treated  $\text{MaNifB}^{\text{H43A}}$  (designated  $\text{MaNifB}^{\text{H43A}}/\text{SAM}$ ) is less distorted away from centrosymmetry (14, 30) than that in SAM-treated  $\text{MaNifB}^{\text{wt}}$  (designated  $\text{MaNifB}^{\text{wt}}/\text{SAM}$ ). Consistent with this observation, the smoothed second derivative of the pre-edge data of  $\text{MaNifB}^{\text{wt}}/\text{SAM}$  transitions from a single inverted peak at  $\sim 7112.6$  eV to two inverted peaks at  $\sim 7112.6$  eV and  $\sim 7114.5$  eV, respectively (Fig. 3.7 b). Such a change has been attributed to the conversion of the K-cluster (with typical tetrahedral Fe-site geometries (9)) to an L-cluster (with an unusual intermediate geometry between tetrahedral and trigonal pyramidal (9)) in  $\text{MaNifB}^{\text{wt}}$  upon incubation with SAM (13). In the case of  $\text{MaNifB}^{\text{H43A}}$ , while a similar peak at  $\sim 7112.6$  eV is observed in the second derivative before and after incubation with SAM, the line-shapes of these plots beyond 7113 eV are different than those of the corresponding  $\text{MaNifB}^{\text{wt}}$  species (Fig. 3.7 b). More importantly, the second peak at  $\sim 7114.5$  eV is absent from the plot of  $\text{MaNifB}^{\text{H43A}}/\text{SAM}$ , although  $\text{MaNifB}^{\text{H43A}}/\text{SAM}$  seems to undergo a transition analogous to that of  $\text{MaNifB}^{\text{wt}}/\text{SAM}$  on the basis of the similar line-shapes of their second derivative plots (Fig. 3.7 b).

Extended X-ray absorption fine structure (EXAFS) analysis of the Fe K-edges of  $\text{MaNifB}^{\text{H43A}}$  provided important insights into the structural metrics of its associated cluster species. Prior to SAM treatment,  $\text{MaNifB}^{\text{H43A}}$  and  $\text{MaNifB}^{\text{wt}}$  display two similar features at  $R + \Delta \sim 1.7$  and  $2.4 \text{ \AA}$ , respectively, in the Fourier transforms (FT; Fig. 3.7 c) of their EXAFS data (Fig. 3.7 d), although the feature of  $\text{MaNifB}^{\text{H43A}}$  at  $R + \Delta \sim 2.4 \text{ \AA}$  is much more prominent than that of  $\text{MaNifB}^{\text{wt}}$ . For

*MaNifB*<sup>H43A</sup>, these FT features can be best fit with Fe–S and Fe···Fe scatterers at 2.29 and 2.71 Å, respectively; whereas for *MaNifB*<sup>wt</sup>, they are best fit with Fe–S scatterers at 2.29 Å and Fe···Fe scatterers at 2.51 and 2.69 Å, respectively (Table 3.1). Upon incubation with SAM, *MaNifB*<sup>H43A</sup>/SAM and *MaNifB*<sup>wt</sup>/SAM seemingly undergo similar changes, both showing extra FT features at  $R + \Delta \sim 3.0$  and  $\sim 3.5$  Å; yet, while *MaNifB*<sup>wt</sup>/SAM displays a substantially increased intensity and a clear shift of its FT feature at  $R + \Delta \sim 2.4$  Å, the corresponding FT feature of *MaNifB*<sup>H43A</sup>/SAM remains mostly unchanged (Fig. 3.7 c). The differences between the two SAM-treated *MaNifB* species are clearly illustrated in the best fits of their EXAFS data: *MaNifB*<sup>H43A</sup>/SAM is best modeled with two types of Fe–S scatterers at 2.27 and 3.88 Å, respectively, and one type of Fe···Fe scatterers at 2.69 Å; whereas *MaNifB*<sup>wt</sup>/SAM is best modeled with one type of Fe–S scatterers at 2.23 Å and two types of Fe···Fe scatterers at 2.64 and 3.70 Å, respectively (Table 3.1). Most notably, the long-range Fe···Fe distance at 3.70 Å, which originates from the intercube scattering between the six carbide-coordinated Fe atoms at the cofactor core (9), is present only in *MaNifB*<sup>wt</sup>/SAM but absent from *MaNifB*<sup>H43A</sup>/SAM. This observation suggests that unlike *MaNifB*<sup>wt</sup>, *MaNifB*<sup>H43A</sup> does not enable the formation of an L-cluster with a  $\mu_6$ -coordinated central carbide in place upon incubation with SAM. In support of this argument, *MaNifB*<sup>H43A</sup> carries clusters with short-range Fe···Fe distances that are characteristic of the [Fe<sub>4</sub>S<sub>4</sub>] clusters before and after incubation with SAM (Table 3.1). However, modeling of the cluster species on *MaNifB*<sup>H43A</sup>/SAM, contrary to that of the cluster species on *MaNifB*<sup>H43A</sup>, requires the inclusion of an extra Fe–S distance at 3.88 Å (Table 3.1) that corresponds to the distance from sulfide to a Fe at the opposite vertex of a [Fe<sub>4</sub>S<sub>4</sub>] cluster. The appearance of such a distance is consistent with an increased order of the two K-cluster units

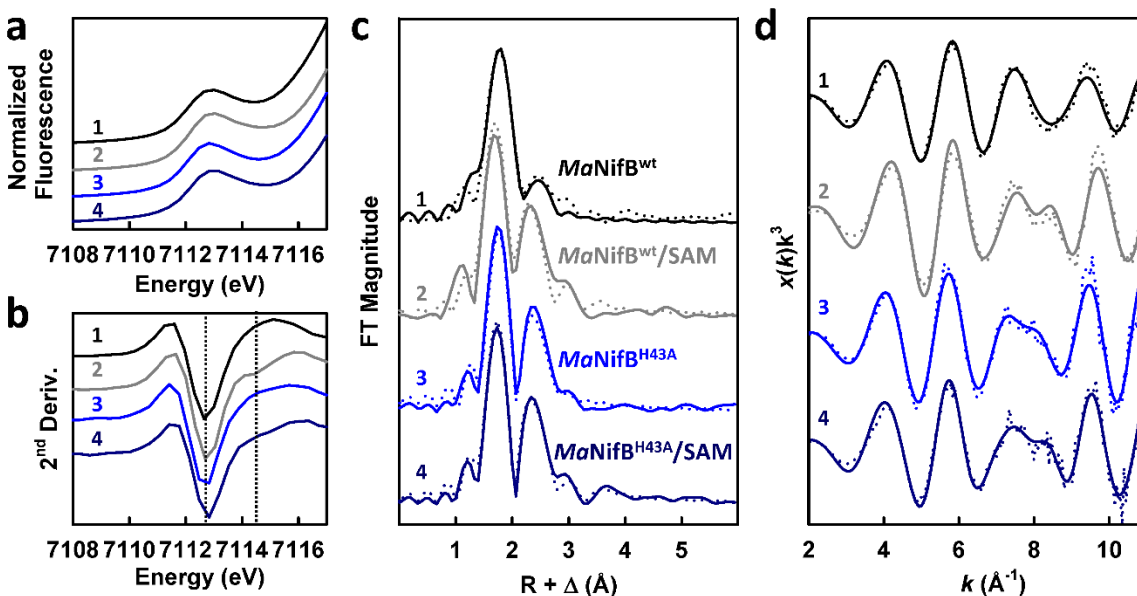


**Figure 3.7 Fe K-edge XAS analysis of *MaNifB* proteins.** **a** Pre-edge regions of the normalized fluorescence spectra and **(b)** smoothed second derivatives of the pre-edge regions, **(c)** Fourier transforms of the EXAFS data (dotted) and the best fits of data (solid), and **(d)**  $k^3$ -weighted EXAFS data (dotted) and the best fits of data (solid). Spectra are shown for *MaNifB*<sup>wt</sup> before (1) and after (2, designated *MaNifB*<sup>wt</sup>/SAM) incubation with SAM, and *MaNifB*<sup>H43A</sup> before (3) and after (4, designated *MaNifB*<sup>H43A</sup>/SAM) incubation with SAM. Note that *MaNifB*<sup>wt</sup> carries the K-cluster (a [Fe<sub>4</sub>S<sub>4</sub>] cluster pair), whereas *MaNifB*<sup>wt</sup>/SAM carries the L-cluster ([Fe<sub>8</sub>S<sub>9</sub>C]). The peaks at ~7112.6 eV and ~7114.5 eV of the pre-edge regions are indicated by dashed vertical lines to illustrate the transition from a single peak at ~7112.6 eV to two peaks at ~7112.6 eV and ~7114.5 eV in the spectrum of *MaNifB*<sup>wt</sup> (**b**, 1 vs. **b**, 2), which corresponds to the conversion of the K-cluster to an L-cluster upon incubation of *MaNifB*<sup>wt</sup> with SAM. Such a change is not observed in the case of *MaNifB*<sup>H43A</sup> following the same treatment with SAM (**b**, 3 vs. **a**, 4). The XAS analysis was performed three times independently ( $n = 3$  independent samples), and representative results are shown in the figure. All protein samples have a concentration of 50 mg mL<sup>-1</sup>. All scans were taken at ~10 K. See Table 3.1 for more details of EXAFS fits.

(i.e., K1 and K2), or further processing of these [Fe<sub>4</sub>S<sub>4</sub>] units into a cluster intermediate between the K- and L-clusters on *MaNifB*<sup>H43A</sup>/SAM; more importantly, it highlights an overall homogeneity of the cluster species on *MaNifB*<sup>H43A</sup>/SAM, as this Fe–S distance can only be observed when the clusters are well-ordered and, therefore, uniform in nature. Overall, the mean squared deviations ( $\sigma^2$ ) of the S, and Fe scatterers are rather small ( $<5 \times 10^{-3} \text{ \AA}^2$ ; Table 3.1), which further supports the homogeneity of the cluster species in the *MaNifB* proteins. Three most likely configurations can be proposed for this cluster intermediate: (i) a partial [Fe<sub>4</sub>S<sub>3</sub>] cluster pair bridged by two sulfide atoms (S<sup>2-</sup>) and a carbon (CH<sub>x</sub>) species, (ii) a face-on

[Fe<sub>4</sub>S<sub>4</sub>] cluster pair bridged by a CH<sub>x</sub> species, and (iii) a vertex-on [Fe<sub>4</sub>S<sub>4</sub>] cluster pair bridged by a CH<sub>x</sub> species, all of which lack the characteristic cofactor core structure that is defined by an interstitial carbide coordinated with six Fe atoms. Given the homogeneity of the cluster species on *MaNifB*<sup>H43A</sup>/SAM, it is likely that one of these proposed models will be identified through future structural characterization of this protein.

Protein	Fe–S			Fe•••Fe			Fe•••Fe		
	N	R(Å)	σ <sup>2</sup> (10 <sup>-3</sup> )	N	R(Å)	σ <sup>2</sup> (10 <sup>-3</sup> )	N	R(Å)	σ <sup>2</sup> (10 <sup>-3</sup> )
<i>MaNifB</i> <sup>wt</sup>	3.8	2.29	8.19	1	2.51	5.82	1.5	2.69	4.35
<i>MaNifB</i> <sup>wt</sup> /SAM	3.1	2.23	4.23	3.5	2.64	7.87	1.5	3.70	7.89
<i>MaNifB</i> <sup>H43A</sup>	3	2.29	2.98	2	2.71	4.02	–	–	–
<i>MaNifB</i> <sup>H43A</sup> /SAM	3	2.27	4.18	2	2.69	4.19	–	–	–
	1	3.88	1.53	–	–	–	–	–	–

**Table 3.1 Best fits of the Fe K-edge EXAFS data.** *N* is the coordination number of neighboring scattering atoms, *R* is distance from absorbing to scattering atoms, and σ<sup>2</sup> is the mean-square disorder of distance. Data is fit between *k* = 2–11.2 Å<sup>-1</sup>. Data for *MaNifB*<sup>wt</sup> and *MaNifB*<sup>wt</sup>/SAM are taken from a previous study (13).

### 3.4 Summary and Conclusion

We have identified His<sup>43</sup> as the source of a nitrogen ligand to the K1-cluster of *MaNifB* that is essential for K- to L-cluster transformation. [Fe<sub>4</sub>S<sub>4</sub>] clusters can be sensitive to degradation, especially when there is a non-Cys-ligated, open Fe site. Therefore, it is advantageous to have a ligand (like the histidine ligand for the K1-cluster), which releases from the [Fe<sub>4</sub>S<sub>4</sub>] cluster module to facilitate the formation of the more stable [Fe<sub>8</sub>S<sub>9</sub>C] L-cluster.

Formation of a cluster intermediate on the SAM-treated MaNifB<sup>H43A</sup> that is distinct from both the K- and L-clusters implies that His<sup>43</sup> serves as a critical structural element and possibly a reaction component during the process of cofactor core formation on MaNifB. The increased intensity of the FT feature of MaNifB<sup>H43A</sup> at  $R + \Delta \sim 2.4 \text{ \AA}$  relative to that in MaNifB<sup>wt</sup> before incubation with SAM points to a stronger Fe...Fe scattering that results from a closer distance between the two [Fe<sub>4</sub>S<sub>4</sub>] units of the K-cluster in MaNifB<sup>H43A</sup> than those in MaNifB<sup>wt</sup>. Such a change in either the distance, orientation, or both, of the K1-cluster relative to the K2-cluster, apparently prevents MaNifB<sup>H43A</sup> from initiating proper coupling between the two K-cluster units. The His<sup>43</sup> ligand, therefore, could play a steric role in keeping the two K-cluster units at the correct distance and orientation to each other by either pulling the K1-cluster away from the K2-cluster via its ligand capacity or directly separating the K1- and K2-clusters with its bulky imidazole ring. Additionally, given the observation of a loss of the nitrogen ligand upon conversion of the K-cluster to an L-cluster on MaNifB, His<sup>43</sup> may lose its coordination to the K1-cluster via protonation, thereby freeing up K1 for the subsequent coupling with K2 into an L-cluster, and facilitating the release of the completed L-cluster to the next biosynthetic apparatus for further maturation. As such, His<sup>43</sup> likely functions as a molecular switch via reversible protonation and deprotonation events, securing the cluster in place in its deprotonated state while giving the cluster certain structural flexibility in its protonated state to accommodate the different states required for cluster conversion. A similarly labile nitrogen ligand is also found in mitoNEET, where protonation of a His ligand to a [Fe<sub>2</sub>S<sub>2</sub>] cluster permits the transfer of the cluster to downstream acceptor proteins (16, 31).

In light of this proposal, it is interesting to consider a coupling of the function of His<sup>43</sup> as a molecular switch with another role of this residue in cofactor core formation, one that is involved in the further deprotonation/dehydrogenation of the initial methylene radical to yield the interstitial carbide at the center of the L-cluster. The observation that the two K-cluster units in SAM-treated MaNifB<sup>H43A</sup> become more aligned with each other but remain largely separate FeS cubanes in character is consistent with an interruption of the carbide formation/insertion process that is required for the coupling/rearrangement of K1 and K2 into the geometry of a cofactor core. Consequently, the cluster is rendered in an unfinished state with the carbon intermediate (CH<sub>x</sub>) not fully deprotonated or dehydrogenated and attached to one or both of the K-cluster units. It is important to note that, other than His<sup>43</sup>, additional residues may also be involved in processing the carbon intermediate to an interstitial carbide, as substitution of His<sup>28</sup> with Ala apparently reduces the efficiency of L-cluster formation on NifB by 41%. A proton relay mechanism involving multiple histidine (or equivalent) residues may be employed in this case to facilitate efficient deprotonation/dehydrogenation of the initial methylene radical to eventually yield a carbide in the center of the L-cluster. While the role of His<sup>43</sup> and other relevant players in the cofactor core formation process is yet to be elucidated, the results of this study provide an important framework for further investigations into the unique radical chemistry underlying the formation of the core structure of the nitrogenase cofactor. Knowledge obtained from these studies will contribute to a better understanding of the mechanism of nitrogenase and shed important light on the mechanisms of analogous biological systems.

### 3.5 Acknowledgments

The National Institutes of Health – National Institute of General Medical Sciences generously provided funding for this work under award number GM67626 to Markus W. Ribbe and Yilin Hu. Additional funding from this agency was provided under award number 1R35GM126961-01 to Dr. R. David Britt.

I am grateful to our collaborators, Dr. R. David Britt and Dr. Jarett Wilcoxon, at UC-Davis for contributing crucial pulse EPR results to this project.

I would also like to thank Dr. Andrew Jasniewski for processing and analyzing the XAS data.

I am grateful to Springer Nature for publishing the results described in this chapter (1, 32) and allowing me to reuse portions in my dissertation.

### 3.6 References

1. Rettberg LA, Wilcoxon J, Lee CC, Stiebritz MT, Tanifuji K, Britt RD, Hu Y. 2018. Probing the coordination and function of Fe<sub>4</sub>S<sub>4</sub> modules in nitrogenase assembly protein NifB. *Nature Communications* 9:1–8.
2. Qi W, Cowan JA. 2011. Structural, Mechanistic and Coordination Chemistry of Relevance to the Biosynthesis of Iron-Sulfur and Related Iron Cofactors. *Coord Chem Rev* 255:688–699.
3. Wiig JA, Hu Y, Ribbe MW. 2011. NifEN-B complex of *Azotobacter vinelandii* is fully functional in nitrogenase FeMo cofactor assembly. *Proc Natl Acad Sci USA* 108:8623–8627.
4. Fay AW, Wiig JA, Lee CC, Hu Y. 2015. Identification and characterization of functional homologs of nitrogenase cofactor biosynthesis protein NifB from methanogens. *Proc Natl Acad Sci USA* 112:14829–14833.

5. Tanifuji K, Lee CC, Sickerman NS, Tatsumi K, Ohki Y, Hu Y, Ribbe MW. 2018. Tracing the '9th Sulfur' of the Nitrogenase Cofactor via a Semi-Synthetic Approach. *Nat Chem* 10:568–572.
6. Flores M. 2003. Probing hydrogen bonding to quinone anion radicals by 1H and 2H ENDOR spectroscopy at 35 GHz. *J Chem Phys* 294.
7. George, G. N. in EXAFSPAK: A Suite of Computer Programs for Analysis of X-ray Absorption Spectra, <https://www-ssrl.slac.stanford.edu/exafspak.html> (Stanford Synchrotron Radiation Laboratory, Stanford Linear Accelerator Center: Menlo Park, CA, 1990).
8. Tenderholt A, Hedman B, Hodgson KO. 2007. PySpline: a modern, cross-platform program for the processing of raw averaged XAS edge and EXAFS data. *AIP Conf Proc* 882.
9. Corbett MC. 2006. Structural insights into a protein-bound iron-molybdenum cofactor precursor. *Proc Natl Acad Sci USA* 103.
10. Ankudinov AL, Ravel B, Rehr JJ, Conradson SD. 1998. Real-space multiple-scattering calculation and interpretation of X-ray-absorption near-edge structure. *Phys Rev B* 58.
11. Spatzal T, Aksoyoglu M, Zhang L, Andrade SLA, Schleicher E, Weber S, Rees DC, Einsle O. 2011. Evidence for interstitial carbon in nitrogenase FeMo cofactor. *Science* 334:940.
12. Strop P, Takahara PM, Chiu H-J, Angove HC, Burgess BK, Rees DC. 2001. Crystal Structure of the All-Ferrous [4Fe-4S]0 Form of the Nitrogenase Iron Protein from *Azotobacter vinelandii*. *Biochemistry* 40:651–656.
13. Jasniewski AJ. 2019. Spectroscopic characterization of an eight-iron nitrogenase cofactor precursor that lacks the '9th sulfur.' *Angew Chem Int Ed Engl* 58.
14. Westre TE, Kennepohl P, DeWitt JG, Hedman B, Hodgson KO, Solomon EI. 1997. A Multiplet Analysis of Fe K-Edge 1s → 3d Pre-Edge Features of Iron Complexes. *J Am Chem Soc* 119:6297–6314.
15. Wojdyr M. 2010. Fityk: a general-purpose peak fitting program. *J Appl Crystallogr* 43.
16. Tamir S, Paddock ML, Darash-Yahana-Baram M, Holt SH, Sohn YS, Agranat L, Michaeli D, Stofleth JT, Lipper CH, Morcos F, Cabantchik IZ, Onuchic JN, Jennings PA, Mittler R, Nechushtai R. 2015. Structure-function analysis of NEET proteins uncovers their role as key regulators of iron and ROS homeostasis in health and disease. *Biochim Biophys Acta* 1853:1294–1315.
17. Taylor AM, Stoll S, Britt RD, Jarrett JT. 2011. Reduction of the [2Fe-2S] Cluster Accompanies Formation of the Intermediate 9-Mercaptodethiobiotin in *Escherichia coli* Biotin Synthase. *Biochemistry* 50:7953–7963.

18. Dicus MM, Conlan A, Nechushtai R, Jennings PA, Paddock ML, Britt RD, Stoll S. 2010. The Binding of Histidine in the (Cys)<sub>3</sub>(His)<sub>1</sub>-coordinated [2Fe-2S] Cluster of Human mitoNEET. *J Am Chem Soc* 132:2037.
19. Gurbiel RJ, Doan PE, Gassner GT, Macke TJ, Case DA, Ohnishi T, Fee JA, Ballou DP, Hoffman BM. 1996. Active site structure of Rieske-type proteins: electron nuclear double resonance studies of isotopically labeled phthalate dioxygenase from *Pseudomonas cepacia* and Rieske protein from *Rhodobacter capsulatus* and molecular modeling studies of a Rieske center. *Biochemistry* 35:7834–7845.
20. Britt RD, Sauer K, Klein MP, Knaff DB, Kriauciunas A, Yu CA, Yu L, Malkin R. 1991. Electron spin echo envelope modulation spectroscopy supports the suggested coordination of two histidine ligands to the Rieske Fe-S centers of the cytochrome b<sub>6</sub>f complex of spinach and the cytochrome bc<sub>1</sub> complexes of *Rhodospirillum rubrum*, *Rhodobacter sphaeroides* R-26, and bovine heart mitochondria. *Biochemistry* 30:1892–1901.
21. Shergill JK, Joannou CL, Mason JR, Cammack R. 1995. Coordination of the Rieske-type [2Fe-2S] cluster of the terminal iron-sulfur protein of *Pseudomonas putida* benzene 1,2-dioxygenase, studied by one- and two-dimensional electron spin-echo envelope modulation spectroscopy. *Biochemistry* 34:16533–16542.
22. Riedel A, Fetzner S, Rampp M, Lingens F, Liebl U, Zimmermann JL, Nitschke W. 1995. EPR, electron spin echo envelope modulation, and electron nuclear double resonance studies of the 2Fe<sub>2</sub>S centers of the 2-halobenzoate 1,2-dioxygenase from *Burkholderia (Pseudomonas) cepacia* 2CBS. *J Biol Chem* 270:30869–30873.
23. Dikanov SA, Tsvetkov Y. 1992. Electron Spin Echo Envelope Modulation (ESEEM) Spectroscopy. CRC Press.
24. Gurbiel RJ, Batie CJ, Sivaraja M, True AE, Fee JA, Hoffman BM, Ballou DP. 1989. Electron-nuclear double resonance spectroscopy of <sup>15</sup>N-enriched phthalate dioxygenase from *Pseudomonas cepacia* proves that two histidines are coordinated to the [2Fe-2S] Rieske-type clusters. *Biochemistry* 28:4861–4871.
25. Dikanov SA, Shubin AA, Kounosu A, Iwasaki T, SamoiloVA RI. 2004. A comparative, two-dimensional <sup>14</sup>N ESEEM characterization of reduced [2Fe-2S] clusters in hyperthermophilic archaeal high- and low-potential Rieske-type proteins. *J Biol Inorg Chem* 9:753–767.
26. Lees NS, Hänzelmann P, Hernandez HL, Subramanian S, Schindelin H, Johnson MK, Hoffman BM. 2009. ENDOR Spectroscopy Shows Guanine N1 Binds to [4Fe-4S] Cluster II of the S-adenosyl methionine-dependent enzyme MoaA - Mechanistic Implications. *J Am Chem Soc* 131:9184–9185.

27. Scholes CP, Lapidot A, Mascarenhas R, Inubushi T, Isaacson RA, Feher G. 1982. Electron nuclear double resonance (ENDOR) from heme and histidine nitrogens in single crystals of aquometmyoglobin. *J Am Chem Soc* 104:2724–2735.
28. Wiig JA, Hu Y, Lee CC, Ribbe MW. 2012. Radical SAM-Dependent Carbon Insertion into the Nitrogenase M-Cluster. *Science* 337:1672–1675.
29. Wiig JA, Hu Y, Ribbe MW. 2015. Refining the pathway of carbide insertion into the nitrogenase M-cluster. *Nat Commun* 6:8034.
30. Sarangi R. 2013. X-ray absorption near-edge spectroscopy in bioinorganic chemistry: application to M–O<sub>2</sub> systems. *Coord Chem Rev* 257.
31. Karmi O, Marjault H-B, Pesce L, Carloni P, Onuchic JN, Jennings PA, Mittler R, Nechushtai R. 2018. The unique fold and lability of the [2Fe-2S] clusters of NEET proteins mediate their key functions in health and disease. *J Biol Inorg Chem* 23:599–612.
32. Rettberg LA, Wilcoxon J, Jasniewski AJ, Lee CC, Tanifuji K, Hu Y, Britt RD, Ribbe MW. 2020. Identity and function of an essential nitrogen ligand of the nitrogenase cofactor biosynthesis protein NifB. *Nat Commun* 11:1–8.

**Chapter 4: Structure of NifH from *Azotobacter vinelandii* in the  
All-Ferrous State**

## 4.1 Introduction

The Fe protein of nitrogenase catalyzes the ambient reduction of CO<sub>2</sub> when its cluster is present in the all-ferrous, [Fe<sub>4</sub>S<sub>4</sub>]<sup>0</sup> oxidation state. Designated AvNifH, the Fe protein of the Mo-nitrogenase from a soil bacterium, *Azotobacter vinelandii*, is a ≈60 kDa homodimer that carries a subunit-bridging [Fe<sub>4</sub>S<sub>4</sub>] cluster and a nucleotide-binding site within each subunit. The [Fe<sub>4</sub>S<sub>4</sub>] cluster of AvNifH can assume three oxidation states: 0, +1 and +2;(1–7) however, it is believed that AvNifH undergoes a one-electron reduction cycle between the [Fe<sub>4</sub>S<sub>4</sub>]<sup>+</sup> and [Fe<sub>4</sub>S<sub>4</sub>]<sup>2+</sup> oxidation states to transfer electrons to its catalytic partner during catalysis.

Recently, AvNifH was shown to act as an independent reductase and catalyze the ambient reduction of CO<sub>2</sub> to CO either in an in vitro assay where an artificial electron source is supplied, or in an AvNifH-expressing cell culture where an in vivo electron donor(s) is present

(1). Interestingly, AvNifH is only capable of catalytic turnover of CO<sub>2</sub> when a strong reductant, europium(II) diethylenetriaminepentaacetic acid (Eu<sup>II</sup>-DTPA;  $E^{0'} = -1.14$  V at pH 8), renders its cluster in the all-ferrous, [Fe<sub>4</sub>S<sub>4</sub>]<sup>0</sup> state (1). Likewise, the Fe protein from *Methanosarcina acetivorans* (designated MaNifH), which shares 72 % sequence identity with AvNifH, also reduces CO<sub>2</sub> catalytically when its [Fe<sub>4</sub>S<sub>4</sub>] cluster is present in the all-ferrous state; only in this case, NifH reduces CO<sub>2</sub> past CO into hydrocarbons (2). Structural analysis of the catalytically competent, all-ferrous state of the Fe protein, therefore, is crucial for understanding the unique reactivity of this FeS enzyme toward CO<sub>2</sub>.

In this chapter, we probe the unique reactivity of the all-ferrous Fe protein toward CO<sub>2</sub> by a combined structural and theoretical approach (3). Structural comparisons of the *Azotobacter*

*vinelandii* Fe protein in the  $[\text{Fe}_4\text{S}_4]^0$  and  $[\text{Fe}_4\text{S}_4]^+$  states point to a possible asymmetric functionality of a highly conserved Arg pair in  $\text{CO}_2$  binding and reduction. Density functional theory (DFT) calculations provide further support for the asymmetric coordination of O by the “proximal” Arg and binding of C to a unique Fe atom of the all-ferrous cluster, followed by the donation of protons by the proximate guanidinium group of Arg that eventually results in the scission of a C–O bond. These results provide essential mechanistic and structural insights into  $\text{CO}_2$  activation by a surface-exposed, scaffold-held  $[\text{Fe}_4\text{S}_4]$  cluster, which may facilitate future development of FeS catalysts for ambient conversion of  $\text{CO}_2$  into useful chemical commodities.

## **4.2 Materials and methods**

### **4.2.1 General Information**

Unless otherwise specified, all chemicals were purchased from Sigma-Aldrich (St. Louis, MO) and Thermo-Fisher Scientific (Waltham, MA). Reagents for protein crystallization were purchased from Hampton Research (Aliso Viejo, CA). All experiments with proteins were performed under an Ar atmosphere using Schlenk techniques or in a glove box operating at <3 ppm  $\text{O}_2$ .

### **4.2.2 Protein Purification and Crystallization**

*Azotobacter vinelandii* strain DJ1141 was grown in a fermenter in 180 L batches, and non-tagged was purified according to published protocols (4, 5). Reagents for protein crystallization

were purchased from Hampton Research and were thoroughly de-aerated by vacuum/Ar-fill cycling before use. All crystals were generated at room temperature in an anaerobic chamber (Coy Laboratory Products), coated with Parabar 10312 oil (Hampton Research) as a cryoprotectant, and flash-frozen in liquid N<sub>2</sub> for data collection. AvNifH was crystallized using a protocol adapted from a previously described procedure (6). Briefly, the purified AvNifH protein was passed through a prepacked Sephadex G25 fine column (GE Healthcare) equilibrated with buffer A [50 mM Tris-HCl (pH 8.0), 450 mM NaCl, and 20% (v/v) glycerol] to remove excess dithionite, and then spin concentrated to 25 mg/mL using Amicon Ultra-4 30 kDa centrifugal filter units (Merck Millipore). Following the addition of a Eu<sup>II</sup>-DTPA solution at a final concentration of 10 mM, the protein solution instantly turned from brown to pink, indicating the reduction of the protein-bound cluster from the +1 state to the all-ferrous, 0 state (7). AvNifH was crystallized using the liquid-liquid diffusion method in glass capillaries by layering 20 μL protein solution and 10 μL precipitant solution (100 mM Tris (pH 8.0), 900 mM NaCl, and 27% (w/v) PEG 4000). Pink crystals grew within one day and were flash-cooled in liquid nitrogen for data collection.

#### **4.2.3 Data Collection and Structure Determination**

The diffraction data of AvNifH crystals were collected at 100 K on beamline 9-2 of Stanford Synchrotron Radiation Lightsource using a wavelength of 0.9856 and a Dectris PILATUS 6M detector. A total of 1600 images were recorded at a distance of 450 mm with an oscillation angle of 0.25° and an exposure time of 0.25 s. The raw data were indexed and processed using

iMosflm and Scala from the CCP4 package (8). Molecular replacement was performed with Phaser in PHENIX (9) using AvNifH (PDB ID: 1G1M) (6) as a search model. The initial model was further improved by cycles of manual building and refinement using Coot and PHENIX (9–11). The stereochemical quality of the final structure was evaluated by MolProbity (12). All molecular graphics were prepared using PyMol (13). Data collection and refinement statistics are summarized in Table 4.1. The structure of EuII-reduced AvNifH (designated AvNifH<sup>0</sup>, PDB ID: 6O0B) was deposited in the Protein Data Bank (<https://www.wwpdb.org>).

#### 4.2.4 CO<sub>2</sub> Reduction Activity Analyses

The in vitro CO<sub>2</sub>-reduction assays were carried out in 9.4 mL assay vial. Each assay reaction contained, in a total volume of 1.0 mL, 500 mM Tris-HCl (pH 10.0), 0.5 mg AvNifH, and 50 mM Ti<sup>III</sup>-citrate or Eu<sup>II</sup>-DTPA. The headspace of each assay contained 100% CO<sub>2</sub> (reactions) or 100% Ar (controls). The assays were assembled without the protein and the reductant, repeatedly flushed and exchanged with CO<sub>2</sub>, followed by equilibration for 30 min until pH stabilized at ~8.0. The reaction was initiated upon the addition of AvNifH, followed immediately by the addition of Ti<sup>III</sup>-citrate or Eu<sup>II</sup>-DTPA and incubation with continuous shaking at 30°C for 300 min until the reaction was complete. Following quenching of each assay by 100 μL of 30% trichloroacetic acid, the headspace sample was examined for the production of CO as described previously (2).

#### 4.2.5 Density Functional Theory (DFT) Calculations

The mechanism of CO<sub>2</sub> coordination and reduction was studied with the DFT programs in the Turbomole package, version 7.0 (14). Atomistic models of the [Fe<sub>4</sub>S<sub>4</sub>] cluster and its immediate protein environment were generated from the AvNifH structure in the all-ferrous, [Fe<sub>4</sub>S<sub>4</sub>] 0 state (PDB ID: 6O0B; this work) or the dithionite-reduced, [Fe<sub>4</sub>S<sub>4</sub>] 1+ state (PDB ID: 1G5P) (15). The coordination of CO<sub>2</sub> was exhaustively screened in various orientations and for a multitude of different oxidation and spin states of the cluster, and no affinity was detected of the Fe atoms of the cluster for the O atoms of CO<sub>2</sub>, as structural optimization inevitably resulted in the dissociation of CO<sub>2</sub> from the cluster. The models were selected as described previously (1) and contained the [Fe<sub>4</sub>S<sub>4</sub>] cluster of AvNifH, as well as C97<sup>A</sup>, C97<sup>B</sup>, C132<sup>A</sup>, C132<sup>B</sup>, R100<sup>A</sup>, R100<sup>B</sup>, F135<sup>A</sup>, F135<sup>B</sup> and the main chain atoms of the residues A98<sup>A</sup>, A98<sup>B</sup>, G99<sup>A</sup>, G99<sup>B</sup>, G133<sup>A</sup> and G133<sup>B</sup> to account for all interactions of the cluster with the protein backbone. N-termini were saturated with acetyl groups according to the crystallographic atom positions. Hydrogen atoms were added to the model with Open Babel (16), assuming protonation of the Arg residues. During structural optimizations, the atoms of the cluster, the side-chain atoms of the cluster-coordinating Cys residues (including C $\alpha$ ), the side-chain atoms of the Arg residues (starting from C $\gamma$ ), the benzene groups of the Phe residues and all hydrogen atoms were allowed to relax spatially. All other atoms were kept structurally frozen. The models were treated as open-shell systems in the unrestricted Kohn-Sham framework. Solvent effects were treated implicitly by the conductor-like solvent screening model (COSMO) (17), assuming a dielectric constant of  $\epsilon=40$ . All structures were optimized with the TPSS functional (18). A def2-TZVP basis set (19, 20) was used for the [Fe<sub>4</sub>S<sub>4</sub>] cluster, the side chain atoms of the Cys residues (including C $\alpha$  atoms),

the atoms of the guanidinium groups and the cluster-bound CO<sub>2</sub> moiety. A def2-SVP basis set was assigned to all remaining atoms to accelerate the calculations. Computational time was further reduced by utilizing the resolution-of-the-identity approximation (20, 21). Antiferromagnetic coupling in the FeS cluster was accounted for by the broken symmetry approach (22–24). Reduction energies were first calculated by assuming the transfer of a free electron with zero kinetic energy. The resulting energies were then corrected with the reported experimental electrode potential of Eu<sup>II</sup>-DTPA ( $E^{0'} = -1.14$  V vs. SHE) following a previously described procedure to obtain approximate redox free energies that better represent the energetics of the system (25, 26). This value was corrected (27) with respect to the Standard Hydrogen Electrode (SHE) by using  $\Delta E$  (SHE) =  $-4.34$  V. The initially obtained reduction energies were transformed into redox free energies by adding the redox free energy of the reductant half-reaction:  $\Delta G^0 = -n F (E^{0'} - \Delta E$  (SHE)) ( $n$ , the number of electrons;  $F$ , Faraday constant) (26, 27). For Eu<sup>II</sup>-DTPA, this value is  $-73.8$  kcal/mol. Protonation energies were calculated by taking the deprotonation energy of Tris-H<sup>+</sup> into account (calculated with TPSS/def2-TZVP, COSMO,  $\epsilon=80$ ).

## 4.3 Results and discussion

### 4.3.1 The Structure of AvNifH in the All-Ferrous State

Crystal structures of the all-ferrous AvNifH have been determined previously at resolutions of 2.25 Å (PDB ID: 1G1M) (6) and 1.95 Å (PDB ID: 6N4J) (28), from protein treated with titanium(III) citrate ( $\text{Ti}^{\text{III}}$ -citrate;  $E^{0'} = -0.79$  V at pH 8), followed by removal of excess  $\text{Ti}^{\text{III}}$ -citrate before crystallization (6). Interestingly, in an in vitro assay of  $\text{CO}_2$  reduction by Fe proteins conducted in the presence of  $\text{Ti}^{\text{III}}$ -citrate shows no activity, contrary to the reactions using  $\text{Eu}^{\text{II}}$ -DTPA (Fig. 4.1), likely due to the interaction between  $\text{CO}_2$  and Ti-derived species (29). To mimic the conditions that enabled  $\text{CO}_2$  reduction by the all-ferrous protein (1, 2) AvNifH was crystallized in the presence of excess  $\text{Eu}^{\text{II}}$ -DTPA and crystals with a characteristic pink color of the all-ferrous,  $[\text{Fe}_4\text{S}_4]^0$  state were obtained. The crystals remained pink during the process of data collection and diffracted to a resolution of 1.6 Å (Table 4.1).

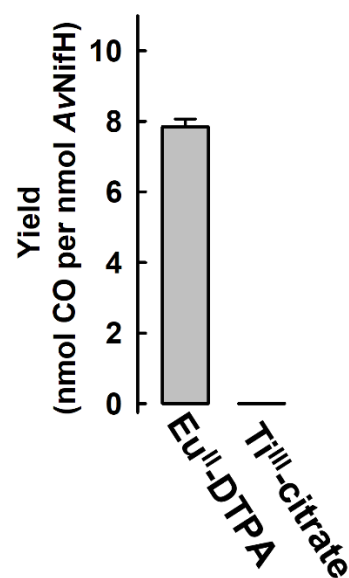


**Figure 4.1**  $\text{CO}_2$  reduction by AvNifH. The amount of CO produced was measured for reactions containing either  $\text{Eu}^{\text{II}}$ -DTPA or  $\text{Ti}^{\text{III}}$ -citrate quantified by GC-FID.

Overall, the  $\text{Eu}^{\text{II}}$ -reduced,  $[\text{Fe}_4\text{S}_4]^0$ -state AvNifH (designated AvNifH<sup>0</sup>, PDB ID: 6O0B) adopts a conformation typical of an Fe protein (Fig. 4.2 a). Each subunit of AvNifH<sup>0</sup> folds as a single  $\alpha/\beta$ -type domain and, together, the two subunits bridge a  $[\text{Fe}_4\text{S}_4]$  cluster at the subunit interface by four Cys ligands: two (Cys97<sup>A</sup>, Cys132<sup>A</sup>) from subunit A and two (Cys97<sup>B</sup>, Cys132<sup>B</sup>) from subunit B (Fig. 4.2 b).

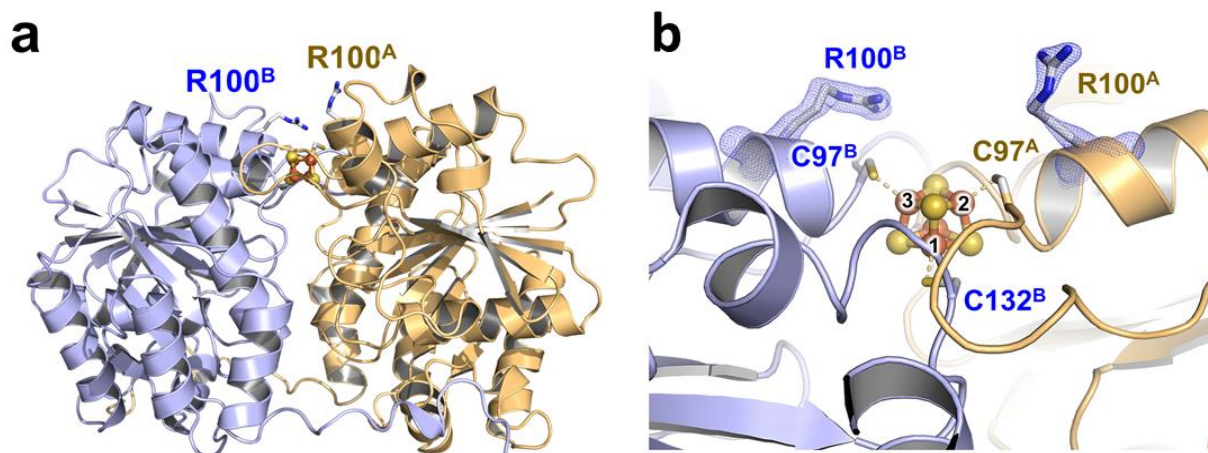


**Figure 4.2 Overall structure of AvNifH<sup>0</sup> and close-up view of the active site.** The Cys ligands and the conserved Arg residues are shown as sticks. The  $[\text{Fe}_4\text{S}_4]$  clusters are shown in ball-and-stick representations. The main chain backbones are shown as cartoons (subunit A, light orange; subunit B, light blue). The atoms are colored as follows: Fe, orange; S, yellow; C, gray; N, dark blue. The electron density ( $2\text{Fo}-\text{Fc}$ ) of the conserved Arg pair (blue meshes) is contoured at  $2.0 \sigma$ .

Despite overall conservation in structure, there are variations between the  $\text{Eu}^{\text{II}}$ -reduced, all-ferrous AvNifH<sup>0</sup> (Fig. 4.3), and the dithionite-reduced,  $[\text{Fe}_4\text{S}_4]^+$ -state AvNifH (designated AvNifH<sup>1</sup>, PDB ID: 1G5P (15)) (Fig. 4.3). Notably, there is a considerably more linear alignment of a pair of helices ( $C^A$  and  $C^B$ ) in AvNifH<sup>0</sup> than their counterparts in AvNifH<sup>1</sup> (Fig. 4.3) and, concomitantly, a significant movement of a highly conserved Arg pair (R100<sup>A</sup> and R100<sup>B</sup>)-located at the tips of helices  $C^A$  and  $C^B$ -toward the center of the surface cavity that houses the  $[\text{Fe}_4\text{S}_4]$  cluster. Strikingly, while R100<sup>A</sup> seems to swing laterally on the surface of the protein and remains distant to the  $[\text{Fe}_4\text{S}_4]$  cluster, R100<sup>B</sup> moves significantly closer to the cluster in the  $\text{Eu}^{\text{II}}$ -reduced protein.

PDB ID	600B
<b>Data Collection</b>	
Space group	<i>P2</i> <sub>1</sub>
Cell dimensions	
A, b, c (Å)	57.05, 93.04, 60.79
$\alpha$ , $\beta$ , $\gamma$ (°)	90.00, 98.87, 90.00
Wavelength (Å)	0.97557
Number of reflections measured	492,239
Number of unique reflections	81,373
Resolution (Å)	38.27 – 1.60 (1.69 – 1.60)
R <sub>pim</sub>	0.046 (1.321)
CC <sub>1/2</sub>	0.995 (0.452)
I/ $\sigma$ (I)	8.0 (1.3)
Completeness (%)	98.6 (98.8)
Multiplicity	6.0 (6.1)
<b>Refinement</b>	
Resolution (Å)	38.27 – 1.60 (1.64 – 1.60)
No. of reflections	81,050
R <sub>work</sub> / R <sub>free</sub>	0.2062 / 0.2185 (0.3054 / 0.2921)
No. of atoms	
Protein	4128
Ligand	8
Solvent	252
B factors (Å <sup>2</sup> )	
Overall	33.48
Protein	33.31
Ligand	19.79
Water	36.58
Ramachandran plot	
Favored (%)	97.36
Allowed (%)	2.64
R.M.S. deviations	
Bond lengths (Å)	0.007
Bond angles (°)	0.81

**Table 4.1 Data collection and refinement statistics for AvNifH<sup>0</sup>.** Values in parentheses represent the highest resolution shell. R<sub>free</sub> was calculated for a test set comprising 2.45 % of all the reflections.

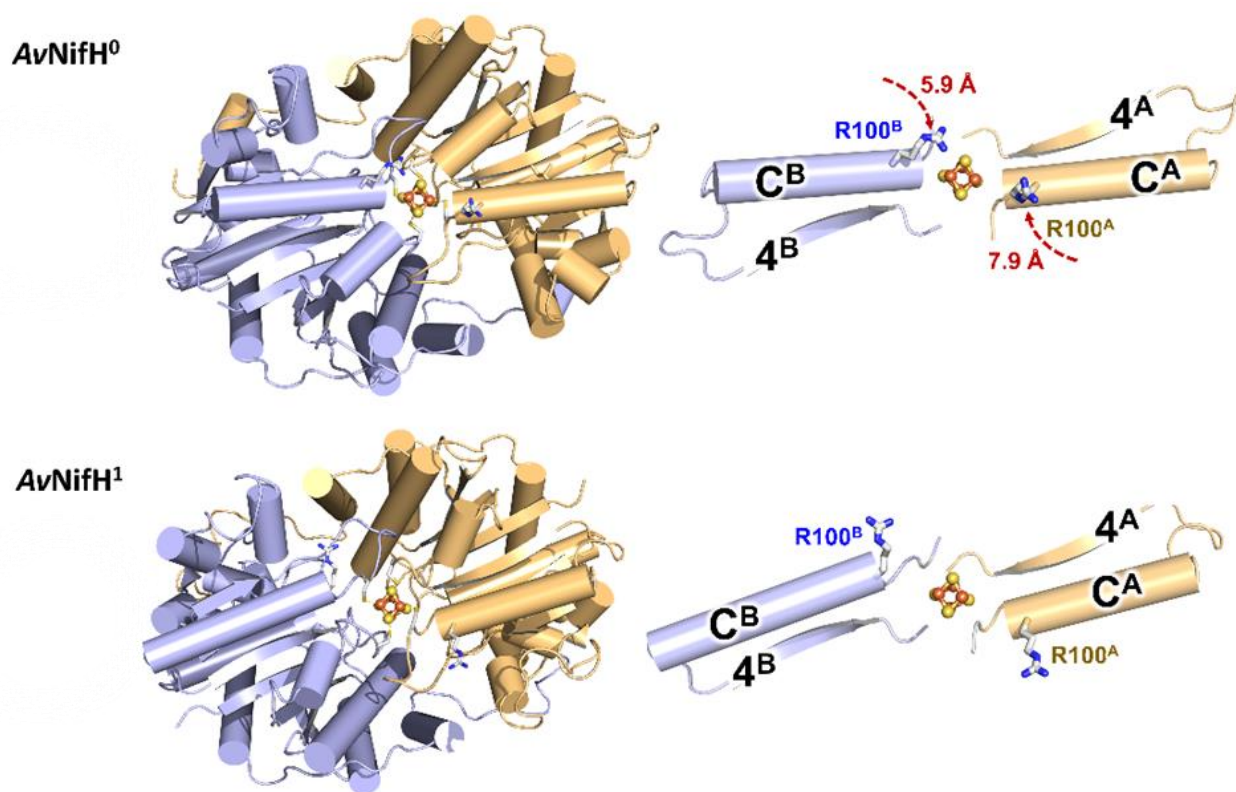


**Figure 4.3 Structural comparison between AvNifH<sup>0</sup> and AvNifH<sup>1</sup>.** Top views of AvNifH<sup>0</sup> (*top left*) and AvNifH<sup>1</sup> (*bottom left*), with the alignments of helices C<sup>B</sup> and C<sup>A</sup> and the positions of the Arg pairs (located at the tips of helices C<sup>B</sup> and C<sup>A</sup>), highlighted (*right*). Dashed red arrows indicate the movements of Arg residues in AvNifH<sup>0</sup> (*top right*) relative to those in AvNifH<sup>1</sup> (*bottom right*). Subunits are shown as ribbons (side view) or cylinders (top view) and colored light orange (subunit A) and light blue (subunit B), respectively. The [Fe<sub>4</sub>S<sub>4</sub>] cluster is shown in ball-and-stick presentation and colored as follows: Fe, orange; S, yellow. The conserved Arg pair (R100<sup>A</sup>, R100<sup>B</sup>) are shown as sticks.

A closer examination reveals that the distance between the side-chain C<sup>γ</sup> of R100<sup>B</sup> and Fe<sup>3</sup> of the cluster is substantially shortened from 10.5 Å (in AvNifH<sup>1</sup>) to 6.3 Å (in AvNifH<sup>0</sup>); in contrast, R100<sup>A</sup> and Fe<sup>2</sup> remain relatively far apart in both structures (Fig. 4.3). It should be noted that the same asymmetric positioning of the Arg pair and the linearized alignment of the C<sup>B</sup> and C<sup>A</sup> helices are also observed in the case of the Ti<sup>III</sup>-citrate-reduced AvNifH<sup>0</sup> (28). The observation of disparate movements of the seemingly equivalent pair of Arg suggests a possible asymmetric

functionality of these residues and suggests the proximal R100<sup>B</sup> in may have a role CO<sub>2</sub> binding and activation.

CO<sub>2</sub> binding and activation was examined further by DFT calculations performed by Dr. Martin Stiebritz. Consistent with the catalytic competence of the all-ferrous AvNifH, when CO<sub>2</sub> was modeled into the structure of the Eu<sup>II</sup>-reduced AvNifH<sup>0</sup>, the CO<sub>2</sub> moiety was observed to adopt a bent, carboxylate-like conformation at an O–C–O angle of 127° (Fig. 4.4 c). Compared to its counterpart in the CO<sub>2</sub>-free structure of AvNifH<sup>0</sup> (Fig. 4.4 a), the [Fe<sub>4</sub>S<sub>4</sub>] cluster in the CO<sub>2</sub>-activated model of AvNifH<sup>0</sup> (designated AvNifH<sup>0C</sup>; Fig. 4.4 c) has its Fe3 atom “lifted” out of the plane and bound to the C atom of CO<sub>2</sub> at a distance of 2.1 Å. Binding of an O atom of CO<sub>2</sub> to the Fe atom of the cluster was excluded by the DFT-based structural optimization that inevitably resulted in the dissociation of CO<sub>2</sub> from the cluster, as well as previous experimental observations that formate was not generated as a product of this reaction (1). The positions of the conserved Arg residues do not significantly change when AvNifH<sup>0</sup> is compared with AvNifH<sup>0C</sup>: the “distal” R100<sup>A</sup> remains distant from both CO<sub>2</sub> and the cluster; whereas the “proximal” R100<sup>B</sup> interacts with one O atom of the CO<sub>2</sub> moiety via hydrogen bonding (Fig. 4.4 c). This observation provides strong theoretical support for an asymmetric functionality of the conserved Arg pair in CO<sub>2</sub> activation. CO<sub>2</sub> capture by a cluster in the 1+ state (Fig. 4.4 b) is explored in Chapter 5.

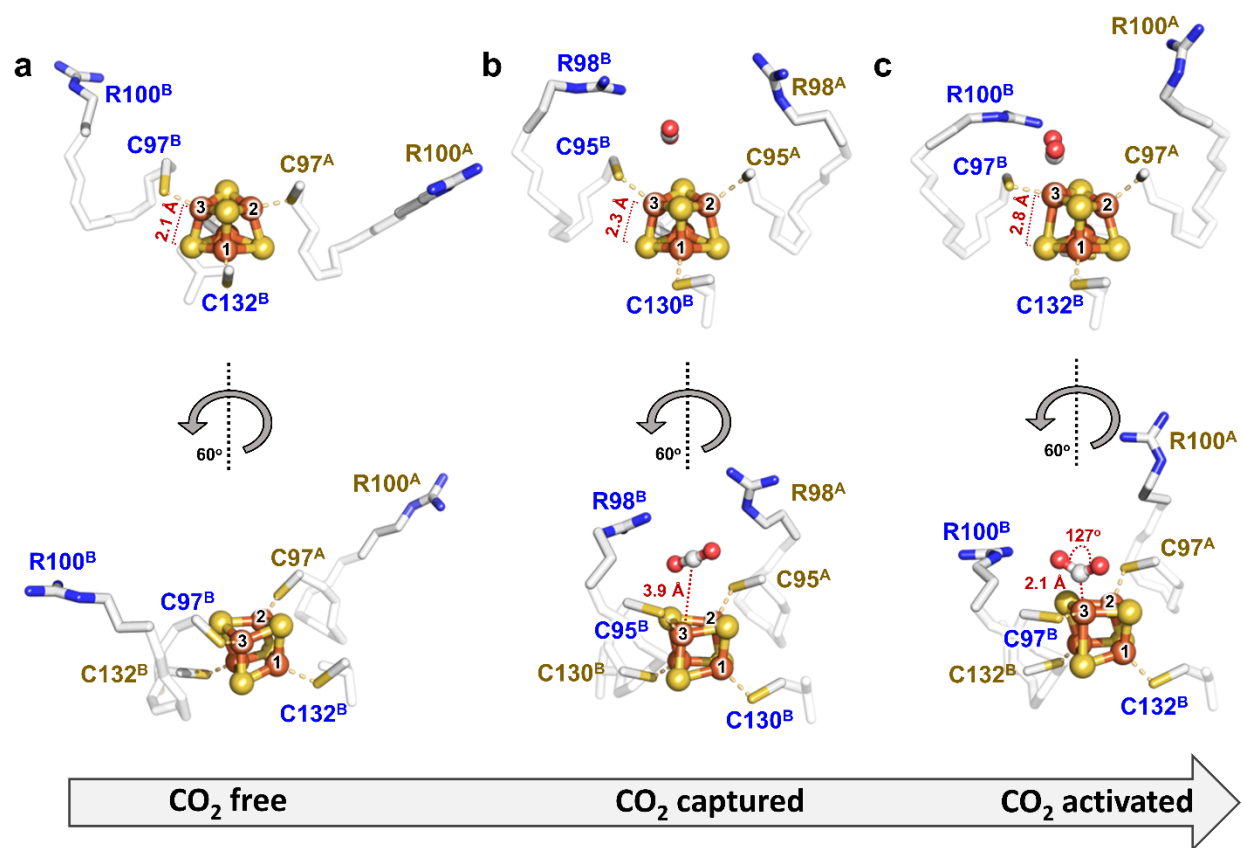


**Figure 4.4** CO<sub>2</sub> capture and activation by NifH proteins. Shown are the active sites of the CO<sub>2</sub>-free (a), CO<sub>2</sub>-captured (b), and CO<sub>2</sub>-activated (c) conformations of the Fe protein, which are represented by AvNifH<sup>1</sup>, MaNifH<sup>1C</sup> (see Chapter 5 for more information), and AvNifH<sup>0C</sup>, respectively. This series of conformations suggest a possible asymmetric movement of the conserved Arg residues that potentially captures CO<sub>2</sub> near the [Fe<sub>4</sub>S<sub>4</sub>] cluster for the subsequent activation of CO<sub>2</sub> via coordination of one O by the “proximal” Arg and binding of C to the Fe3 atom of the all-ferrous cluster. The movement of the “proximal” Arg (R100<sup>B</sup> in AvNifH and R98<sup>B</sup> in MaNifH) and the “distal” Arg (R100<sup>A</sup> in AvNifH and R98<sup>A</sup> in MaNifH), as well as the activation of CO<sub>2</sub> from a linear conformation to a bent, carboxylate-like one, are shown from two angles. The CO<sub>2</sub>-free (a) and CO<sub>2</sub>-captured (b) conformations are derived from crystal structures, whereas the CO<sub>2</sub>-activated conformation (c) is derived from DFT modeling of CO<sub>2</sub> into the crystal structure.

### 4.3.2 Mechanism of from CO<sub>2</sub> Activation from Density Functional Theory Calculations

To tackle events following the binding and activation of CO<sub>2</sub>, we performed DFT calculations to examine the reduction of CO<sub>2</sub> to CO by the all-ferrous AvNifH in the presence of excess reductant (Fig. 4.5). Binding of CO<sub>2</sub> to the [Fe<sub>4</sub>S<sub>4</sub>]<sup>0</sup> cluster of AvNifH, which renders the

CO<sub>2</sub> moiety in an activated carboxylate-like conformation concomitant with a charge redistribution to the O atoms, is weak yet energetically feasible at  $-3.4 \text{ kcal mol}^{-1}$  (Fig. 4.5 a, b, step 1). Subsequently, a proton is transferred from the proximate guanidinium group of R100<sup>B</sup>-positioned at a calculated R-NH<sub>2</sub><sup>+</sup>...CO<sub>2</sub> distance of 1.64 Å-to an oxygen of CO<sub>2</sub>, although the reaction is slightly endothermic due to the basicity of this residue (Fig. 4.5 a, b, step 2). This event is followed by an exothermic re-protonation step of the proximal R100<sup>B</sup> by Tris-H<sup>+</sup> (Fig. 4.5 a, b, step 3), leading to the formation of a cluster-bound CO<sub>2</sub>H intermediate in a series of events that is exothermic overall (Fig. 4.5 a, b, steps 1–3). Endothermic electron transfer (Fig. 4.5 a, b, step 4), facilitated by an excess of reductant, then triggers proton transfer from the proximal R100<sup>B</sup> to the bound CO<sub>2</sub>H intermediate, resulting in the exothermic cleavage C–O(H) bond and dissociation of a water molecule (Fig. 4.5 a, b, step 5). Subsequent re-protonation of the proximal R100<sup>B</sup> is exothermic (Fig. 4.5 a, b, step 6), and this step is followed by endothermic dissociation of CO (Fig. 4.5 a, b, step 7) and regeneration of the all-ferrous cluster in the presence of an excess of reductant. It should be noted that the first protonation event could also occur via direct proton transfer from the buffer (i.e., Tris-H<sup>+</sup>; Fig. 4.5 a, b, step 2); however, this Arg-independent route may not be favored due to a lack of protein-facilitated stabilization of the substrate. Moreover, the proposed role of Arg in proton donation is supported by the site-directed mutagenetic studies of *MdNifH*, (see Chapter 5, or Ref. (30)) which demonstrate a largely intact or significantly decreased CO<sub>2</sub>-reducing activity upon an R→H or R→G mutation that corresponds to the preservation or elimination of the hydrogen bonding ability at the position of the conserved Arg.

## 4.4 Summary and Conclusions

The combined structural and theoretical studies presented herein provide plausible answers to questions such as why the Fe protein is substantially more active in CO<sub>2</sub> reduction in the all-ferrous, [Fe<sub>4</sub>S<sub>4</sub>]<sup>0</sup> state than the dithionite-reduced, [Fe<sub>4</sub>S<sub>4</sub>]<sup>+</sup> state and why this reaction has a low efficiency overall from an energetic perspective (Fig. 4.5). Interestingly, the movement of Arg pair toward the [Fe<sub>4</sub>S<sub>4</sub>] cluster upon reduction to the all-ferrous state parallels the

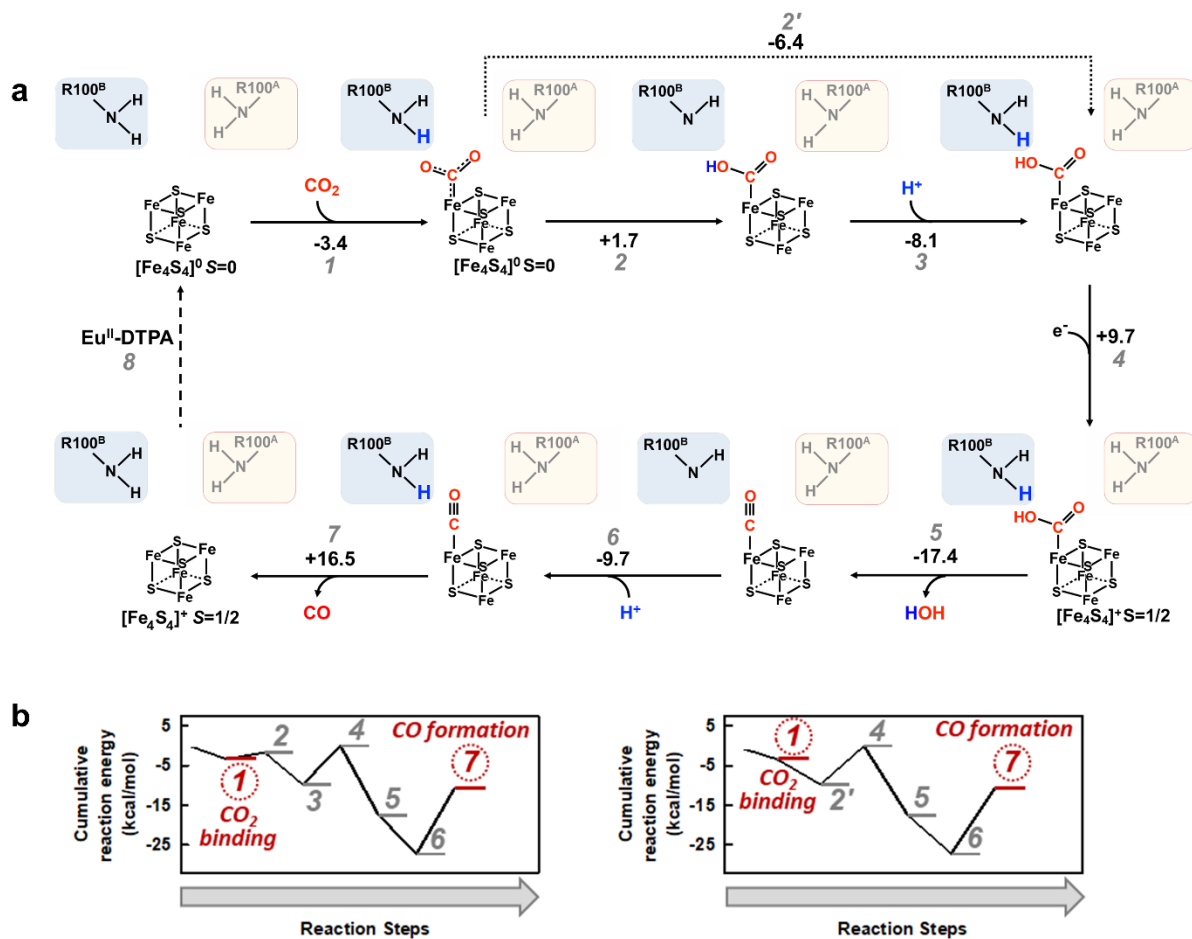


**Figure 4.5** Proposed mechanism of CO<sub>2</sub> mechanism by AvNifH<sup>0</sup>. (a) An energetically plausible pathway derived from DFT calculations (TPSS/def2-SVP/def2-TZVP, COSMO ε=40). (b) Cumulative reaction energies of the proposed pathway of CO<sub>2</sub> activation by AvNifH<sup>0</sup>, with the initial protonation facilitated by R100 (left) or achieved directly via Tris-H<sup>+</sup> in the buffer (right).

movement of a flexible Arg pair in the ADP-bound form of the activator of 2-hydroxyglutaryl-CoA dehydratase upon reduction (31, 32). This parallelism is particularly striking given that the hydratase activator (a ASKHA class ATPase) is the only known example other than the Fe protein (a SIMIBI class ATPase) that has a  $[\text{Fe}_4\text{S}_4]$  cluster capable of adopting the “super-reduced,” all-ferrous state (33). In the case of the all-ferrous Fe protein, while the proposed asymmetric activation of  $\text{CO}_2$  via a “proximal” Arg and a single  $\text{Fe}^3$  site requires further experimental support, a disparate functionality of the conserved Arg pair was observed in the regulation of nitrogenase activity via the ADP ribosylation of only one Arg residue (34), whereas a distinctive Fe site of the all-ferrous  $[\text{Fe}_4\text{S}_4]^0$  cluster was identified earlier by Mössbauer spectroscopy (35). Such a distinction of the apparently equivalent elements in the Fe protein structure seems to be crucial for the activation and reduction of  $\text{CO}_2$ . It may also account for the substantially lower activity of the Fe protein than the Ni-containing carbon monoxide dehydrogenase (Ni-CODH) in  $\text{CO}_2$  reduction, as the latter enzyme uses a real “asymmetric” His/Lys pair (for O coordination) and a real “asymmetric” Fe/Ni pair (as Lewis acid/base) at its active C-cluster site to facilitate the cleavage of a C–O bond (36–39). Further investigations of the mechanism of  $\text{CO}_2$  activation by Fe proteins, combined with comparisons with analogous systems, could shed additional light on the unique reactivity of scaffold held FeS clusters toward  $\text{CO}_2$  and facilitate future development of efficient FeS catalysts for ambient  $\text{CO}_2$  conversion.

## 4.5 Acknowledgments

This work was supported by generous funding through a National Science Foundation CAREER grant, award number CHE-1651398 to Dr. Yilin Hu.

I am extremely grateful to Dr. Martin T. Stiebritz for his important contribution of performing and analyzing the DFT calculations. I would also like to thank Dr. Chi Chung Lee for performing the CO<sub>2</sub> reduction assay. Thank you, Dr. Wonchull Kang, for assisting with structure refinement and deposition.

I am also grateful to Wiley-VCH Verlag GmbH & Co for publishing these results (3) and allowing me to reuse portions in this chapter.

## 4.6 References

1. Rebelein JG, Stiebritz MT, Lee CC, Hu Y. 2017. Activation and reduction of carbon dioxide by nitrogenase iron proteins. *Nat Chem Biol* 13:147–149.
2. Stiebritz MT, Hiller CJ, Sickerman NS, Lee CC, Tanifuji K, Ohki Y, Hu Y. 2018. Ambient conversion of CO<sub>2</sub> to hydrocarbons by biogenic and synthetic [Fe<sub>4</sub>S<sub>4</sub>] clusters. *Nat Catal* 1:444–451.
3. Rettberg LA, Stiebritz MT, Kang W, Lee CC, Ribbe MW, Hu Y. 2019. Structural and Mechanistic Insights into CO<sub>2</sub> Activation by Nitrogenase Iron Protein. *Chem Eur J* 25:13078–13082.
4. Ribbe MW, Hu Y, Guo M, Schmid B, Burgess BK. 2002. The FeMoco-deficient MoFe protein produced by a nifH deletion strain of *Azotobacter vinelandii* shows unusual P-cluster features. *J Biol Chem* 277:23469–23476.
5. Sickerman NS, Hu Y, Ribbe MW. 2017. Chapter Nine - Nitrogenase Assembly: Strategies and Procedures, p. 261–302. In David, SS (ed.), *Method Enzymol*. Academic Press.

6. Strop P, Takahara PM, Chiu H-J, Angove HC, Burgess BK, Rees DC. 2001. Crystal Structure of the All-Ferrous [4Fe-4S]<sub>0</sub> Form of the Nitrogenase Iron Protein from *Azotobacter vinelandii*. *Biochemistry* 40:651–656.
7. Watt GD, Reddy KRN. 1994. Formation of an all ferrous Fe<sub>4</sub>S<sub>4</sub> cluster in the iron protein component of *Azotobacter vinelandii* nitrogenase. *Journal of Inorganic Biochemistry* 53:281–294.
8. Winn MD, Ballard CC, Cowtan KD, Dodson EJ, Emsley P, Evans PR, Keegan RM, Krissinel EB, Leslie AGW, McCoy A, McNicholas SJ, Murshudov GN, Pannu NS, Potterton EA, Powell HR, Read RJ, Vagin A, Wilson KS. 2011. Overview of the CCP4 suite and current developments. 4. *Acta Cryst D* 67:235–242.
9. Adams PD, Afonine PV, Bunkóczi G, Chen VB, Davis IW, Echols N, Headd JJ, Hung L-W, Kapral GJ, Grosse-Kunstleve RW, McCoy AJ, Moriarty NW, Oeffner R, Read RJ, Richardson DC, Richardson JS, Terwilliger TC, Zwart PH. 2010. PHENIX: a comprehensive Python-based system for macromolecular structure solution. *Acta Cryst D* 66:213–221.
10. Afonine PV, Adams PD. 2013. Crystallographic Structure Refinement in a Nutshell, p. 211–219. *In* *Advancing Methods for Biomolecular Crystallography*. Springer, Dordrecht.
11. Emsley P, Lohkamp B, Scott WG, Cowtan K. 2010. Features and development of Coot. *Acta Crystallogr D Biol Crystallogr* 66:486–501.
12. Davis IW, Leaver-Fay A, Chen VB, Block JN, Kapral GJ, Wang X, Murray LW, Arendall WB, Snoeyink J, Richardson JS, Richardson DC. 2007. MolProbity: all-atom contacts and structure validation for proteins and nucleic acids. *Nucleic Acids Res* 35:W375–W383.
13. PyMOL | pymol.org.
14. Ahlrichs R, Bär M, Häser M, Horn H, Kölmel C. 1989. Electronic structure calculations on workstation computers: The program system turbomole. *Chemical Physics Letters* 162:165–169.
15. Schlessman JL, Woo D, Joshua-Tor L, Howard JB, Rees DC. 1998. Conformational variability in structures of the nitrogenase iron proteins from *Azotobacter vinelandii* and *Clostridium pasteurianum* Edited by I. A. Wilson. *Journal of Molecular Biology* 280:669–685.
16. O’Boyle NM, Banck M, James CA, Morley C, Vandermeersch T, Hutchison GR. 2011. Open Babel: An open chemical toolbox. *Journal of Cheminformatics* 3:33.
17. Klamt A, Schüürmann G. 1993. COSMO: a new approach to dielectric screening in solvents with explicit expressions for the screening energy and its gradient. *J Chem Soc, Perkin Trans 2* 799–805.

18. Tao J, Perdew JP, Staroverov VN, Scuseria GE. 2003. Climbing the Density Functional Ladder: Nonempirical Meta--Generalized Gradient Approximation Designed for Molecules and Solids. *Phys Rev Lett* 91:146401.
19. Schäfer A, Huber C, Ahlrichs R. 1994. Fully optimized contracted Gaussian basis sets of triple zeta valence quality for atoms Li to Kr. *J Chem Phys* 100:5829–5835.
20. Weigend F. 2006. Accurate Coulomb-fitting basis sets for H to Rn. *Phys Chem Chem Phys* 8:1057–1065.
21. Eichkorn K, Weigend F, Treutler O, Ahlrichs R. 1997. Auxiliary basis sets for main row atoms and transition metals and their use to approximate Coulomb potentials. *Theor Chem Acta* 97:119–124.
22. Noodleman L. 1981. Valence bond description of antiferromagnetic coupling in transition metal dimers. *J Chem Phys* 74:5737–5743.
23. Noodleman L, Post D, Baerends EJ. 1982. Symmetry breaking and ionization from symmetry equivalent inner shells and lone pairs in X $\alpha$  theory. *Chemical Physics* 64:159–166.
24. Noodleman L, Peng CY, Case DA, Mouesca J-M. 1995. Orbital interactions, electron delocalization and spin coupling in iron-sulfur clusters. *Coordination Chemistry Reviews* 144:199–244.
25. Noodleman L, Han Du W-G, Fee JA, Götz AW, Walker RC. 2014. Linking chemical electron-proton transfer to proton pumping in cytochrome c oxidase: broken-symmetry DFT exploration of intermediates along the catalytic reaction pathway of the iron-copper dinuclear complex. *Inorg Chem* 53:6458–6472.
26. Torres RA, Lovell T, Noodleman L, Case DA. 2003. Density Functional and Reduction Potential Calculations of Fe<sub>4</sub>S<sub>4</sub> Clusters. *J Am Chem Soc* 125:1923–1936.
27. Tissandier MD, Cowen KA, Feng WY, Gundlach E, Cohen MH, Earhart AD, Coe JV, Tuttle TR. 1998. The Proton's Absolute Aqueous Enthalpy and Gibbs Free Energy of Solvation from Cluster-Ion Solvation Data. *J Phys Chem A* 102:7787–7794.
28. Wenke BB, Spatzal T, Rees DC. 2019. Site-Specific Oxidation State Assignments of the Iron Atoms in the [4Fe:4S]<sup>2+/1+/0</sup> States of the Nitrogenase Fe-Protein. *Angewandte Chemie* 131:3934–3937.
29. Dodson LG, Thompson MC, Weber JM. 2018. Interactions of Molecular Titanium Oxides TiO<sub>x</sub> ( x = 1-3) with Carbon Dioxide in Cluster Anions. *J Phys Chem A* 122:6909–6917.

30. Rettberg LA, Kang W, Stiebritz MT, Hiller CJ, Lee CC, Liedtke J, Ribbe MW, Hu Y. 2019. Structural Analysis of a Nitrogenase Iron Protein from *Methanosarcina acetivorans*: Implications for CO<sub>2</sub> Capture by a Surface-Exposed [Fe<sub>4</sub>S<sub>4</sub>] Cluster. *mBio* 10.
31. Locher KP, Hans M, Yeh AP, Schmid B, Buckel W, Rees DC. 2001. Crystal structure of the *Acidaminococcus fermentans* 2-hydroxyglutaryl-CoA dehydratase component A11 Edited by I. A. Wilson. *Journal of Molecular Biology* 307:297–308.
32. Knauer SH, Buckel W, Dobbek H. 2012. On the ATP-Dependent Activation of the Radical Enzyme (R)-2-Hydroxyisocaproyl-CoA Dehydratase. *Biochemistry* 51:6609–6622.
33. Hans M, Buckel W, Bill E. 2008. Spectroscopic evidence for an all-ferrous [4Fe–4S]<sub>0</sub> cluster in the superreduced activator of 2-hydroxyglutaryl-CoA dehydratase from *Acidaminococcus fermentans*. *J Biol Inorg Chem* 13:563–574.
34. Nordlund S, Högbom M. 2013. ADP-ribosylation, a mechanism regulating nitrogenase activity. *The FEBS Journal* 280:3484–3490.
35. Yoo SJ, Angove HC, Burgess BK, Hendrich MP, Münck E. 1999. Mössbauer and Integer-Spin EPR Studies and Spin-Coupling Analysis of the [4Fe-4S]<sub>0</sub> Cluster of the Fe Protein from *Azotobacter vinelandii* Nitrogenase. *J Am Chem Soc* 121:2534–2545.
36. Jeoung J-H, Fesseler J, Goetzl S, Dobbek H. 2014. Carbon Monoxide. Toxic Gas and Fuel for Anaerobes and Aerobes: Carbon Monoxide Dehydrogenases, p. 37–69. In Kroneck, PMH, Torres, MES (eds.), *The Metal-Driven Biogeochemistry of Gaseous Compounds in the Environment*. Springer Netherlands, Dordrecht.
37. Fesseler J, Jeoung J-H, Dobbek H. 2015. How the [NiFe<sub>4</sub>S<sub>4</sub>] Cluster of CO Dehydrogenase Activates CO<sub>2</sub> and NCO<sup>-</sup>. *Angewandte Chemie International Edition* 54:8560–8564.
38. Kung Y, Drennan CL. 2011. A role for nickel–iron cofactors in biological carbon monoxide and carbon dioxide utilization. *Current Opinion in Chemical Biology* 15:276–283.
39. Can M, Armstrong FA, Ragsdale SW. 2014. Structure, function, and mechanism of the nickel metalloenzymes, CO dehydrogenase, and acetyl-CoA synthase. *Chem Rev* 114:4149–4174.

## **Chapter 5: Structure of NifH from *Methanosarcina acetivorans***

## 5.1 Introduction

Iron-sulfur (FeS) proteins utilize a wide array of FeS clusters to play key roles that range from electron transfer and catalysis to structural and regulatory functions in biological systems (1–7). The NifH of nitrogenase is homodimer carrying a subunit-bridging  $[\text{Fe}_4\text{S}_4]$  cluster at the protein surface, and is best known for its function as an obligate electron donor for its catalytic partner during substrate turnover (8, 9). Recently, the NifH protein from a diazotrophic microbe, *Azotobacter vinelandii* (designated AvNifH), was shown to act as a reductase on its own and catalyze the ambient reduction of  $\text{CO}_2$  to CO via redox changes of its  $[\text{Fe}_4\text{S}_4]$  cluster (10). Interestingly, while the cluster of AvNifH is believed to cycle between the  $[\text{Fe}_4\text{S}_4]^{1+}$  (reduced) and  $[\text{Fe}_4\text{S}_4]^{2+}$  (oxidized) states (11–15) for its function as an electron donor in nitrogenase catalysis, catalytic turnover of  $\text{CO}_2$  by AvNifH on its own was observed when a strong reductant, europium(II) diethylenetriaminepentaacetic acid ( $\text{Eu}^{\text{II}}\text{-DTPA}$ ;  $E^{0'}$  = 1.14 V at pH 8.0), poised its cluster in the all-ferrous,  $[\text{Fe}_4\text{S}_4]^0$  state under in vitro conditions (10). Perhaps more interestingly, the Fe protein from a methanogenic microorganism, *Methanosarcina acetivorans* (designated MaNifH), was capable of reducing  $\text{O}_2$  past CO into hydrocarbons under ambient conditions in the presence of  $\text{Eu}^{\text{II}}\text{-DTPA}$ , further illustrating the unique reactivity of the  $[\text{Fe}_4\text{S}_4]$  cluster toward  $\text{CO}_2$  (16, 17). Together, these observations point to the nitrogenase Fe protein as a simple model system for mechanistic investigations of FeS-based  $\text{CO}_2$  activation and reduction.

Of the Fe protein species that have been investigated for their reactivity toward  $\text{CO}_2$ , MaNifH is particularly interesting given its ability to convert  $\text{CO}_2$  to CO and hydrocarbons. Despite its archaeal origin, MaNifH shares a sequence identity of 59% and a sequence similarity of 72%

with AvNifH. Like AvNifH, *MaNifH* is a ~60 kDa homodimer containing an [Fe<sub>4</sub>S<sub>4</sub>] cluster that can adopt three oxidation states: (i) the oxidized state ([Fe<sub>4</sub>S<sub>4</sub>]<sup>2+</sup>), which is generated upon treatment by indigodisulfonate; (ii) the reduced state ([Fe<sub>4</sub>S<sub>4</sub>]<sup>1+</sup>), which is generated upon treatment by dithionite (DT); and (iii) the “super-reduced,” all-ferrous state ([Fe<sub>4</sub>S<sub>4</sub>]<sup>0</sup>), which is generated upon treatment by Eu<sup>II</sup>-DTPA (17). There are differences, however, in the electronic properties of *MaNifH* and *AvNifH*, which are reflected by a stronger *S* = 3/2 contribution to the electron paramagnetic resonance (EPR) spectrum of the reduced *MaNifH* and a decreased intensity of the parallel mode, *g* = 16.4 signal in the EPR spectrum of the super-reduced *MaNifH* (17). These differences, along with the lower reduction potential of the [Fe<sub>4</sub>S<sub>4</sub>]<sup>1+/2+</sup> pair of *MaNifH* (*E*<sup>0</sup> = -395 mV) than that of *AvNifH* ([Fe<sub>4</sub>S<sub>4</sub>]<sup>1+/2+</sup>: *E*<sup>0</sup> = -301 mV) (16), may contribute to the difference in the reactivities of *MaNifH* and *AvNifH* toward CO<sub>2</sub>. The redox dependence of this reaction is further illustrated by a substantially decreased CO<sub>2</sub>-reducing activity of both *MaNifH* and *AvNifH* in the presence of dithionite, a weaker reductant than Eu<sup>II</sup>-DTPA, which renders the clusters of these Fe proteins in the catalytically inefficient [Fe<sub>4</sub>S<sub>4</sub>]<sup>1+</sup> state (10, 16). The significantly decreased activity of Fe protein in a dithionite-driven reaction could prove advantageous for capturing CO<sub>2</sub> in an early stage of CO<sub>2</sub> reduction.

Here, a 2.4-Å crystal structure of the Fe protein from *Methanosarcina acetivorans* (*MaNifH*) (18) is reported, which is generated in the presence of a reductant, dithionite, and an alternative CO<sub>2</sub> source, bicarbonate. Structural analysis of this methanogen Fe protein species suggests that CO<sub>2</sub> is possibly captured in an unactivated, linear conformation near the [Fe<sub>4</sub>S<sub>4</sub>] cluster of *MaNifH* by a conserved arginine (Arg) pair in a concerted and asymmetric manner. Density functional theory calculations and mutational analyses provide further support for the

capture of CO<sub>2</sub> on *MaNifH* while suggesting a possible role of Arg in the initial coordination of CO<sub>2</sub> via hydrogen bonding and electrostatic interactions. These results provide a useful framework for further mechanistic investigations of CO<sub>2</sub> activation by a surface-exposed [Fe<sub>4</sub>S<sub>4</sub>] cluster, which may facilitate future development of FeS catalysts for ambient conversion of CO<sub>2</sub> into valuable chemical commodities.

This work reports the crystal structure of a previously uncharacterized NifH protein from a methanogenic organism, which provides important insights into the structural properties of the less characterized, yet highly interesting archaeal nitrogenase enzymes. Moreover, the structure-derived implications for CO<sub>2</sub> capture by a surface-exposed [Fe<sub>4</sub>S<sub>4</sub>] cluster point to the possibility of developing novel strategies for CO<sub>2</sub> sequestration while providing the initial insights into the unique mechanism of FeS-based CO<sub>2</sub> activation.

## **5.2 Materials and Methods**

### **5.2.1 General Information**

Unless otherwise specified, all chemicals were purchased from Sigma-Aldrich (St. Louis, MO) and Thermo-Fisher Scientific (Waltham, MA). Reagents for protein crystallization were purchased from Hampton Research (Aliso Viejo, CA). All experiments with proteins were performed under an Ar atmosphere using Schlenk techniques or in a glove box operating at <3 ppm O<sub>2</sub>.

### 5.2.2 Protein Purification and Crystallization

All protein purification steps were carried out anaerobically using Schlenk techniques. His-tagged *MaNifH* was purified by immobilized metal affinity as described elsewhere (17, 19). Reagents for protein crystallization were purchased from Hampton Research and were thoroughly deaerated by vacuum/Ar-fill cycling before use. All crystals were generated at room temperature in an anaerobic chamber (Coy Laboratory Products), coated with Parabar 10312 oil (Hampton Research) as a cryo-protectant, and flash-frozen in liquid nitrogen for data collection. *MaNifH* was crystallized at room temperature by a microbatch-under-oil method. The purified *MaNifH* protein was desalted on a G-25 fine column equilibrated with buffer M (10 mM EPPS [pH 8.0], 100 mM NaCl, 10% [vol/vol] glycerol, and 2 mM sodium dithionite [DT]) and then concentrated to 10 mg/ml by Amicon Ultra-4 30-kDa centrifugal filter units. The crystals were grown by combining a mixture of 1  $\mu$ l protein solution and 3  $\mu$ l precipitant solution (2.3 M ammonium sulfate, 7% [w/v] polyethylene glycol 3350 [PEG 3350], 12 mM sodium carbonate, and 2 mM DT) under Al's oil (Hampton Research). The protein solution was brown, indicating that the protein-bound cluster was present in the reduced, +1 state. Brown crystals grew after 2 weeks and were flash-frozen in liquid nitrogen for data collection.

### 5.2.3 Data Collection and Structure Determination

The diffraction data of *MaNifH* crystals were collected at 100 K on beamline 8.2.1 of Advanced Light Source using a wavelength of 0.9774 Å and an ADSC Q315r charge-coupled device (CCD) detector. A total of 501 images were recorded for *MaNifH* at a distance of 450 mm, with an oscillation angle of 0.25° and an exposure time of 0.25 s. The raw data were indexed and

processed using iMosflm and Scala in the CCP4 package (20). Molecular replacement was performed with Phaser in PHENIX (21) using the structure of the *Clostridium pasteurianum* NifH protein (PDB ID 1CP2) (22) as a search model. The initial model was improved by cycles of manual building and refinement using Coot and PHENIX (21, 23, 24). At the end of the refinement cycle, water, carbonate, glycerol, or CO<sub>2</sub> was manually put into the model of *MaNifH* and further refined for 3 cycles using PHENIX. The stereochemical quality of the final structures was evaluated by MolProbity (25). All molecular graphics were prepared using PyMol (26). Data collection and statistics for refinement and ligand modeling are summarized in Table 5.1.

#### **5.2.4 Mutant Strain Construction and Activity Analyses**

Strains expressing R98H and R98G *MaNifH* variants were constructed via site-directed mutagenesis of the wild-type *Methanosarcina acetivorans nifH* sequence carried on a pET14b vector (17), followed by transformation of the resultant plasmids into *Escherichia coli* strain BL21(DE3). The in vitro CO<sub>2</sub>-reduction assays were carried out in 9.4-ml assay vials. Each assay contained, in a total volume of 1.0 ml, 500 mM Tris-HCl (pH 10.0), 0.5 mg Fe protein (wild-type or R98H or R98G variant *MaNifH*), and 100 mM Eu<sup>III</sup>-DTPA. In addition, the headspace of each assay contained 100% CO<sub>2</sub> (for reactions) or 100% Ar (for controls). The assays were assembled without protein and Eu<sup>III</sup>-DTPA and repeatedly flushed and exchanged with CO<sub>2</sub>, followed by equilibration for 30 min until pH stabilized at ~8.0. The reaction was initiated by addition of *MaNifH*, followed immediately by addition of Eu<sup>III</sup>-DTPA and incubation with continuous shaking at 30°C for 300 min until the reaction was complete. Following the quenching of each

assay by 100  $\mu$ l of 30% trichloroacetic acid, the headspace sample was examined for the production of CO and hydrocarbons as described previously (16).

### 5.2.5 EPR Spectroscopy Analyses

The EPR samples were prepared in a Vacuum Atmospheres glove box and flash-frozen in liquid nitrogen before analysis. The DT-reduced samples contained 2 mM DT, 50 mM Tris-HCl (pH 8.0), 500 mM NaCl, and 10% (v/v) glycerol. EPR spectra were recorded by an ESP 300 E<sub>z</sub> spectrophotometer (Bruker) interfaced with an ESR-9002 liquid-helium continuous-flow cryostat (Oxford Instruments) using a microwave power of 50 mW, a gain of  $5 \times 10^4$ , a modulation frequency of 100 kHz, and a modulation amplitude of 5 G. Five scans were recorded for each EPR sample at a temperature of 10 K and a microwave frequency of 9.62 GHz.

### 5.2.6 Density Functional Theory Calculations

The mechanism of CO<sub>2</sub>, carbonate, and bicarbonate coordination was studied with the DFT programs in the Turbomole package, version 7.0 (27). Atomistic models of the [Fe<sub>4</sub>S<sub>4</sub>] cluster and its immediate protein environment were generated from the structure of *Ma*NifH (PDB ID 6NZJ [this work]) in the DT-reduced, [Fe<sub>4</sub>S<sub>4</sub>]<sup>1+</sup> state.

The models were selected as described previously (10) and contained the [Fe<sub>4</sub>S<sub>4</sub>] cluster and C95<sup>A</sup>, C95<sup>B</sup>, C130<sup>A</sup>, C130<sup>B</sup>, R98<sup>A</sup>, R98<sup>B</sup>, F133<sup>A</sup>, F133<sup>B</sup>, and the main-chain atoms of the residues A96<sup>A</sup>, A96<sup>B</sup>, A97<sup>A</sup>, G97<sup>B</sup>, G131<sup>A</sup>, G131<sup>B</sup>, G132<sup>A</sup>, and G132<sup>B</sup> of *Ma*NifH to account for all interactions of the cluster with the protein backbone. N termini were saturated with acetyl

groups according to the crystallographic atom positions. Hydrogen atoms were added to the model with Open Babel (28), assuming protonation of the Arg residues. During structural optimizations, the atoms of the cluster, the side-chain atoms of the cluster-coordinating Cys residues (including C $\alpha$ ), the side-chain atoms of the Arg residues (starting from C $\gamma$ ), the benzene groups of the Phe residues, and all hydrogen atoms were allowed to relax spatially. All other atoms were kept structurally frozen. The models were treated as open-shell systems in the unrestricted Kohn-Sham framework. Solvent effects were treated implicitly by the conductor-like solvent screening model (COSMO) (29), assuming a dielectric constant of  $\epsilon = 40$ . The structures were optimized with the TPSS (Tao-Perdew-Staroverov-Scuseria) functional (30). A def2-TZVP basis set (31, 32) was used for the [Fe<sub>4</sub>S<sub>4</sub>] cluster, the side-chain atoms of the Cys residues (including C $\alpha$  atoms), the atoms of the guanidinium groups, and the cluster-bound CO<sub>2</sub>, carbonate, and bicarbonate moieties. A def2-SVP basis set was assigned to all remaining atoms to accelerate the calculations. Computational time was further reduced by utilizing the resolution-of-the-identity approximation (33, 34). Antiferromagnetic coupling in the FeS cluster was accounted for by the broken symmetry approach (35–37).

## 5.3 Results and discussion

### 5.3.1 Analysis of the Dithionite-Reduced *MaNifH* Structure

*MaNifH* crystallized in the presence of dithionite had a characteristic brown color, consistent with the presence of its [Fe<sub>4</sub>S<sub>4</sub>] cluster in the +1 oxidation state. The  $\sim 2.4$ -Å structure of the dithionite-reduced *MaNifH* (PDB ID 6NZJ) adopts the same overall conformation as all Fe

protein structures reported to date (9, 22, 38, 39), with each of its subunits folded as a single  $\alpha/\beta$ -type domain and its  $[\text{Fe}_4\text{S}_4]$  cluster situated in a surface cavity between the two subunits (Fig. 5.1 A, B). A closer examination of the region surrounding the active site of *Ma*NifH (Fig. 5.1 C) reveals the ligation of the  $[\text{Fe}_4\text{S}_4]$  cluster by four Cys residues: two from subunit A (Cys95<sup>A</sup>, Cys130<sup>A</sup>) and two from subunit B (Cys95<sup>B</sup>, Cys130<sup>B</sup>). Interestingly, the electron density omit map ( $F_o - F_c$ ) contoured at 3  $\sigma$  (Fig. 5.1 C, green mesh) indicates the presence of additional electron density that lies immediately next to the crystallographic symmetry axis, seemingly held by two pairs of conserved Arg residues (R98<sup>A</sup> and R98<sup>B</sup>)—one from each of the two adjacent *Ma*NifH subunit dimers.

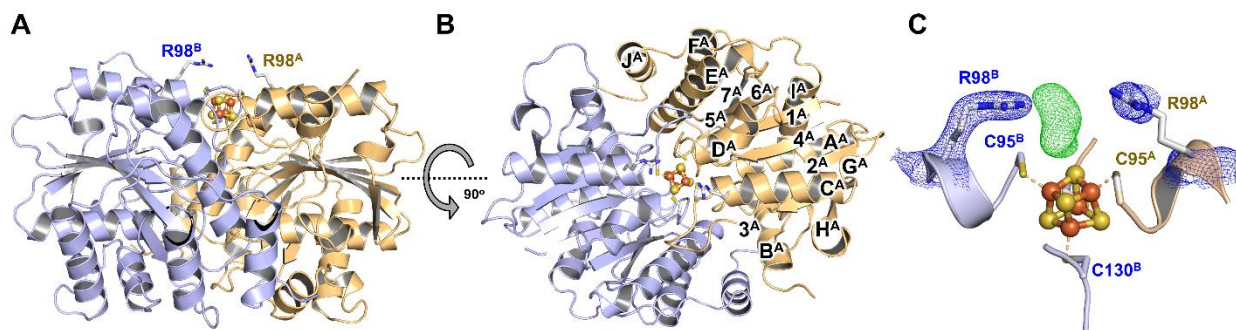


**Figure 5.1 Structure of *Ma*NifH and visualization of additional density.** Side (A) and top (B) views of the 2.4-Å crystal structure of *Ma*NifH. The subunits are shown as ribbons (subunit A, light orange; subunit B, light blue). The  $\alpha$ -helices (AA-JA) and  $\beta$ -sheets (1A-7A) of subunit A are indicated. The  $[\text{Fe}_4\text{S}_4]$  cluster is shown in ball-and-stick presentation (Fe, orange; S, yellow). (C) The electron density ( $2F_o - F_c$ ) of the active site of *Ma*NifH was contoured at 1.5- $\sigma$  level for the conserved Arg pair (blue meshes), and the omit map ( $F_o - F_c$ ) of the additional electron density (green mesh) that is unaccounted for in the structure was contoured at 3.0- $\sigma$  level. The four Cys ligands (C95<sup>A</sup>, C130<sup>A</sup>, C95<sup>B</sup>, C130<sup>B</sup>) and the conserved Arg pair (R98<sup>A</sup>, R98<sup>B</sup>) are shown as sticks.

PDB ID	6NZJ				
<b>Data Collection</b>					
Space group	<b>P6<sub>5</sub>22</b>				
Cell dimensions					
A, b, c (Å)	96.16, 96.16, 320.24				
$\alpha$ , $\beta$ , $\gamma$ (°)	90.0, 90.0, 120.0				
Wavelength (Å)	0.97741				
Number of reflections measured	419,306 (35,917)				
Number of unique reflections	35,959 (3,432)				
Resolution (Å)	83.3 – 2.4 (2.5-2.4)				
R <sub>meas</sub> (%)	11.1 (78.1)				
CC <sub>1/2</sub>	0.999 (0.810)				
I/ $\sigma$ (I)	5.4 (1.0)				
Completeness (%)	100.0 (99.9)				
Multiplicity	11.9 (11.2)				
<b>Refinement</b>					
Resolution (Å)	83.3 -2.4				
No. of reflections	35,369				
R <sub>work</sub> /R <sub>free</sub>	18.31 / 21.80				
No. of atoms					
Protein	3,952				
Ligand	23				
Solvent	172				
B factors (Å <sup>2</sup> )					
Overall	49.01				
Protein	48.95				
Ligand	42.46				
Water	51.34				
Ramachandran plot					
Favored (%)	96.49				
Allowed (%)	3.51				
R.M.S. deviations					
Bond lengths (Å)	0.008				
Bond angles (°)	0.90				
<b>Statistics for the plausible ligands</b>					
	R <sub>work</sub> %	R <sub>free</sub> %	Ligand Occupancy	Ligand B factor (Å <sup>2</sup> )	RSCC
No ligand	18.31	21.80	-	-	-
CO <sub>2</sub>	18.27	21.78	1.00	50.69	0.89
Glycerol	18.22	21.78	0.46	41.82	0.95
Carbonate	18.23	21.84	0.51	45.27	0.095

**Table 5.1 Data collection and refinement statistics for MaNifH.** Values in parentheses represent the highest resolution shell. R<sub>free</sub> was calculated for a test set comprising 5 % of all reflections.

### 5.3.2 Modeling of Extra Electron Density in the Structure of the Dithionite-Reduced *MaNifH*

Given that the additional electron density may originate from the small molecules in the protein preparations or crystallographic solutions, several possible candidates were considered and modeled into this density: water, carbonate, glycerol, and CO<sub>2</sub>, respectively, were modeled into this density. Water is an unlikely contributor to this density, as modeling of one water molecule in the asymmetric unit and another in its symmetry mate results in substantial “leftover” electron density in the  $F_o - F_c$  omit map. Carbonate and glycerol, on the other hand, could be modeled as two molecules—each at ~50% occupancy—at the crystallographic symmetry axis with reasonable *R* factor values (see Table 5.1). Similarly, CO<sub>2</sub> could be modeled with reasonable *R* factor values at the crystallographic symmetry axis; only, in this case, two molecules of CO<sub>2</sub>—each at 100% occupancy—could be assigned to the asymmetric unit and its symmetry mate, respectively (Table 5.1). It should be noted that the modeling of two CO<sub>2</sub> moieties results in some negative electron density; however, the overall crystallographic statistics are reasonable to support this model (Table 5.1) despite the difficulty to conclusively assign this ligand near the crystallographic symmetry axis.

### 5.3.3 DFT Calculations of CO<sub>2</sub> Capture by Dithionite-Reduced *MaNifH*

To seek support for the assignment of CO<sub>2</sub> as the extra electron density in the crystal structure of *MaNifH*, density functional theory (DFT) calculations were then used to analyze the CO<sub>2</sub> affinity of the [Fe<sub>4</sub>S<sub>4</sub>]<sup>1+</sup> cluster in *MaNifH*. Consistent with previous findings for both *AvNifH*-bound and synthetic [Fe<sub>4</sub>S<sub>4</sub>] clusters (10, 16), CO<sub>2</sub> does not interact well with the

[Fe<sub>4</sub>S<sub>4</sub>]<sup>1+</sup> cluster of *MaNifH* and tends to dissociate from the cluster during the course of structural optimization; however, the two highly conserved Arg residues in *MaNifH* (R98<sup>A</sup>, R98<sup>B</sup>) form a cage-like configuration around the CO<sub>2</sub> molecule that assists in trapping it in close proximity to the cluster. Interestingly, the location of the CO<sub>2</sub> moiety in the DFT-optimized model is in good agreement with half of the electron density pattern in the structure of *MaNifH*, except for a slight reorientation of CO<sub>2</sub>. In comparison, DFT optimization reveals protonation of carbonate by R98<sup>B</sup>, followed by coordination of the resulting bicarbonate in a position parallel to the upper surface of the [Fe<sub>4</sub>S<sub>4</sub>] cluster, which is rather distinct from the perpendicular position modeled for carbonate in the crystal structure of *MaNifH*. This observation is important, as it provides theoretical support for the assignment of CO<sub>2</sub> as a potential ligand in the structure of the dithionite-reduced *MaNifH* protein. The fact that the *MaNifH* crystals were generated at a bicarbonate concentration in the same order of magnitude as that used to generate a CO<sub>2</sub>-bound conformation of CO dehydrogenase (40) provides further support for the assignment of CO<sub>2</sub> in the *MaNifH* structure. In this scenario, the CO<sub>2</sub> moiety has its C atom placed at a distance of ~4 Å from the nearest Fe atom (Fe-3) of the [Fe<sub>4</sub>S<sub>4</sub>] cluster, with the NH<sub>2</sub><sup>+</sup> groups of R98<sup>A</sup> and R98<sup>B</sup> assuming the “distal” and “proximal” positions, respectively, to Fe-3 (Fig. 5.2). This observation suggests a possible role of the conserved Arg pair in capturing CO<sub>2</sub> via hydrogen bonding or electrostatic interactions, or a combination of the two, as well as a potentially asymmetric functionality of the two Arg residues in this process.

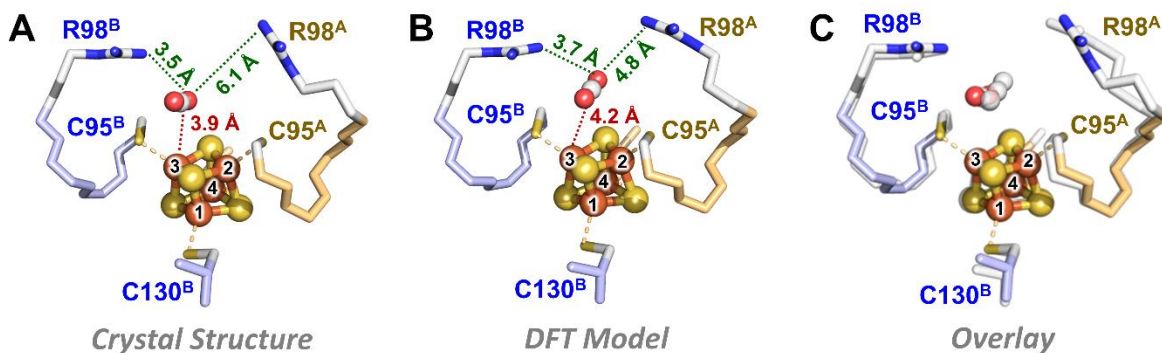


**Figure 5.2 Comparison of *MaNifH* crystal structure and DFT model** Crystal (A) and DFT-optimized (B) structures of *MaNifH* with the extra electron density modeled as CO<sub>2</sub> and (C) an overlay of the two structures. The conserved pair of Arg residues assume “proximal” (R98<sup>B</sup>) and “distal” (R98<sup>A</sup>) positions, respectively, to the CO<sub>2</sub> moiety and the Fe-3 atom of the cluster (A and B), and CO<sub>2</sub> occupies a highly similar position in the crystal structure and the DFT model (C). The [Fe<sub>4</sub>S<sub>4</sub>] cluster and CO<sub>2</sub> moiety are shown in ball-and-stick presentation and colored as follows: Fe, orange; S, yellow; C, gray; O, red. The Cys ligands and the conserved Arg residues are shown as sticks.

### 5.3.4 Examining the Role of the Conserved Arg Pair of *MaNifH* in CO<sub>2</sub> Capture

To test the proposed role of conserved Arg residues in CO<sub>2</sub> capture, site-directed mutagenic analysis was performed and mutated R98 of *MaNifH* to either a His or a Gly. Both R98H and R98G *MaNifH* variants display the same  $S = 1/2$  EPR signal as the wild-type protein, which is indicative of an unperturbed [Fe<sub>4</sub>S<sub>4</sub>] center in the +1 oxidation state (Fig. 5.3 A). However, the R98H variant of *MaNifH* retains ~80% CO<sub>2</sub>-reducing activity, whereas the R98G variant loses ~85% of this activity (Fig. 5.3 B), consistent with the preservation (i.e., the R→H mutation) or elimination (i.e., the R→G mutation) of the hydrogen bonding ability at the position of R98. The somewhat decreased activity of the R98H variant could be explained by a shorter side chain of His and, consequently, reduced efficiency of this residue in hydrogen bonding/proton donation than Arg. Reduced proton donation by His would also account for a shift of the product profile of the R98H variant (hydrocarbon/CO ratio of 1.9) from hydrocarbon formation to CO formation

compared to that of the wild-type *MaNifH* (hydrocarbon/CO ratio of 2.7), as the formation of CO requires fewer protons than that of hydrocarbons.

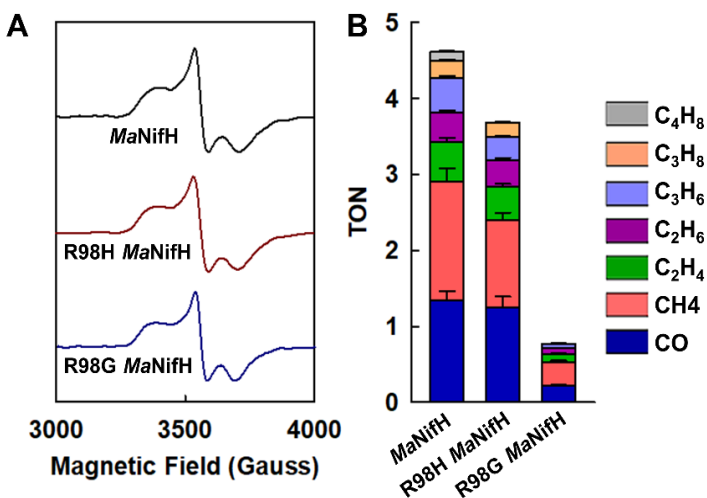


**Figure 5.3 Spectroscopic and catalytic features of the wild-type and variant *MaNifH*.** **A** EPR spectra and **(B)** CO<sub>2</sub>-reducing activities of wild-type and variant *MaNifH*. EPR spectra were collected at 10 K. The wild-type and R98H and R98G variant *MaNifH* are dimers of ~60 kDa and contain  $3.7 \pm 0.1$ ,  $3.9 \pm 0.4$ , and  $3.8 \pm 0.2$  nmol Fe per nmol protein, respectively. Like the wild-type *MaNifH*, the R98H and R98G variants display the same  $[\text{Fe}_4\text{S}_4]^+$  characteristic,  $S = 1/2$  EPR signal in the dithionite-reduced state **A**, yet they display disparate activities in CO<sub>2</sub> reduction **B**. The hydrocarbon/CO ratios (calculated based on total nmol of reduced carbons) of the wild-type *MaNifH* and R98H variant are 2.7 and 1.9, respectively, suggesting a shift from hydrocarbon formation to CO formation in the latter case.

### 5.3.5 Proposal of a Plausible Mechanism for the Initial Capture of CO<sub>2</sub> by *MaNifH*

To obtain further insights into the mechanism of CO<sub>2</sub> capture by nitrogenase Fe proteins, the dithionite-reduced *MaNifH* structure (PDB ID 6NZJ) that is potentially bound with CO<sub>2</sub> (Fig 5.4 B) was compared with a previously reported, dithionite-reduced *AvNifH* structure (PDB ID 1G5P) that is free of CO<sub>2</sub> (22) (Fig 5.4 A). Consistent with a high degree of sequence homology between *MaNifH* and *AvNifH*, the subunits A and B in *MaNifH* show C $\alpha$  deviations of only 0.599 and 0.616 Å, respectively, relative to those in *AvNifH*. Yet, the two subunit chains in *MaNifH* are more similar to each other in terms of secondary structural elements, particularly for the structurally less conserved  $\alpha$ -helical regions. More strikingly, compared to their counterparts in *AvNifH*, there is a distinct difference in the position of the two subunits of *MaNifH* with

respect to each other, which flattens the surface cavity and consequently “pushes” the [Fe<sub>4</sub>S<sub>4</sub>] cluster further toward the surface. A top-view comparison between the two structures also reveals a “linearization” of helices C<sup>A</sup> and C<sup>B</sup> in *Ma*NifH relative to those in *Av*NifH. There is also a substantial swing of the Arg pair, R98<sup>A</sup> and R98<sup>B</sup> (located at the tips of helices C<sup>A</sup> and C<sup>B</sup>), toward the center of the surface cavity. Such a movement of the conserved Arg pair could reflect a concerted action of the “distal” R98<sup>A</sup> and the “proximal” R98<sup>B</sup> in the initial capture of CO<sub>2</sub> in an unactivated, linear conformation near the Fe-3 atom of the [Fe<sub>4</sub>S<sub>4</sub>] cluster (Fig. 5.4 B). Further activation of CO<sub>2</sub> into a bent, carboxylate-like conformation may continue to employ an asymmetric mechanism (see Chapter 4). Previous DFT calculations of CO<sub>2</sub> activation by the catalytically competent, all-ferrous *Av*NifH (10) led to the proposal of binding of an activated CO<sub>2</sub> moiety via coordination of C with Fe-3 of the cluster and coordination of O with the guanidinium group of the “proximal” R100<sup>B</sup> (corresponding to the “proximal” R98<sup>B</sup> in *Ma*NifH), with the latter potentially donating protons for the subsequent C-O bond cleavage.

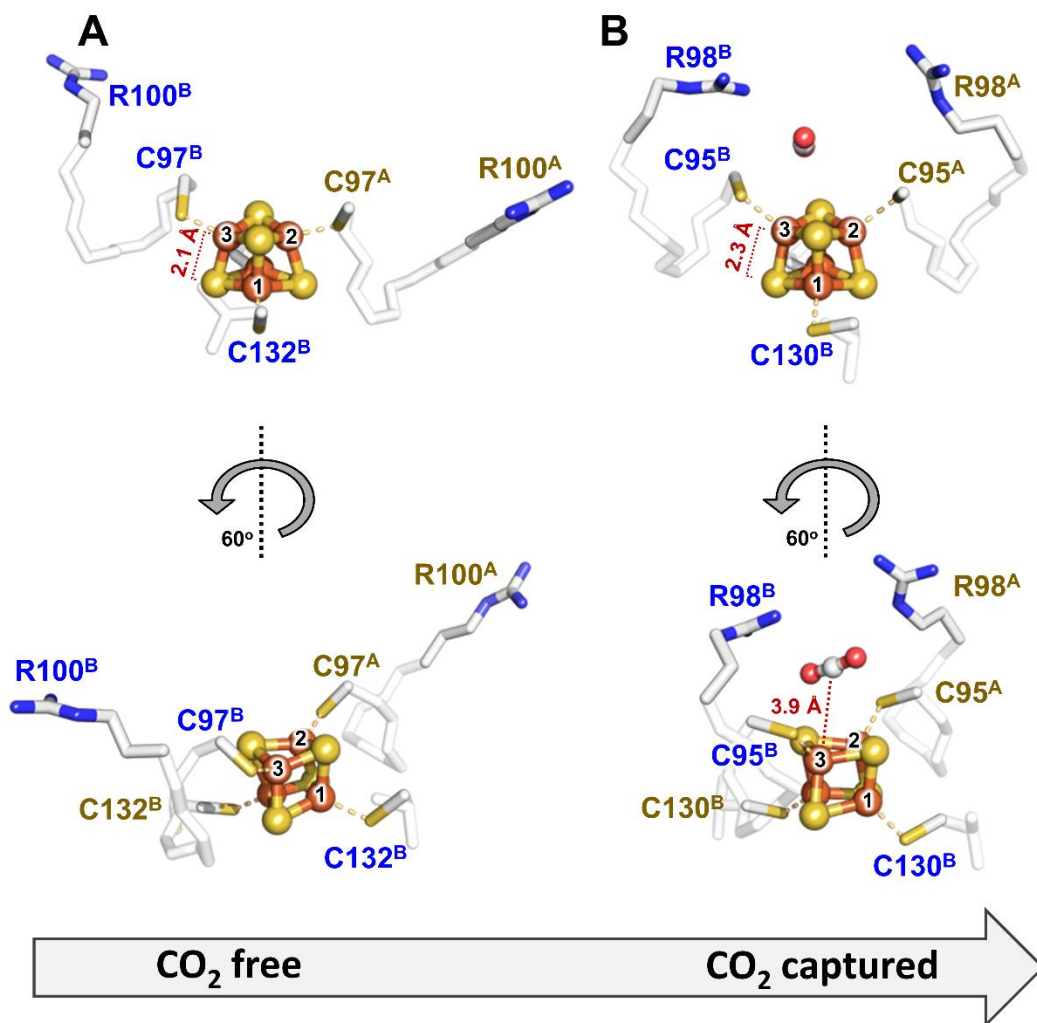


**Figure 5.4 Model for CO<sub>2</sub> capture.** Comparison of the CO<sub>2</sub>-free (A) and CO<sub>2</sub>-captured (B) conformations of Fe protein, showing concerted yet asymmetric movement of a pair of conserved Arg residues that potentially capture CO<sub>2</sub> near the [Fe<sub>4</sub>S<sub>4</sub>] cluster. The CO<sub>2</sub>-free and CO<sub>2</sub>-captured conformations are represented by the homologous *AvNifH* and *MaNifH*, respectively. The movement of the “proximal” Arg (R100<sup>B</sup> in *AvNifH* and the corresponding R98<sup>B</sup> in *MaNifH*) and the “distal” Arg (R100<sup>A</sup> in *AvNifH* and the corresponding R98<sup>A</sup> in *MaNifH*) is shown from two angles

## 5.4 Summary and Conclusion

In light of a plausible asymmetric mechanism of CO<sub>2</sub> activation by Fe protein, it is interesting to consider the mechanism proposed for the Ni-dependent CO dehydrogenase in CO<sub>2</sub> activation, which involves the action of the Fe/Ni atoms of its heterometallic C-cluster ([NiFe<sub>4</sub>S<sub>4</sub>]) as a pair

of Lewis acid/base to facilitate scission of a C-O bond (40–43). In the absence of such a heterometal-based asymmetry, it is plausible that activation of CO<sub>2</sub> by the homometallic [Fe<sub>4</sub>S<sub>4</sub>] cluster would resort to a structure-based asymmetry that enables interactions between O and the guanidinium group of the proximal Arg, as well as binding of C to the nearest Fe-3 atom. It is worth noting that the proposed asymmetric functionality of the conserved Arg pair in CO<sub>2</sub> activation is consistent with the previously established regulatory mechanism of nitrogenase activity through ADP-ribosylation of only one of these conserved Arg residues (44). In contrast, the structure-based suggestion of a single reactive Fe (Fe-3) site for CO<sub>2</sub> activation may have relevance to the unique Fe site that was identified by earlier Mössbauer studies of the all-ferrous Fe protein (45). While the functions of these asymmetric elements await further elucidation, the current study provides a useful framework for investigating the structural basis of Fe protein-based CO<sub>2</sub> capture and activation. Moreover, trapping of CO<sub>2</sub> by a pair of surface-located arginines loosely resembles approaches that employ nitrogen-based ligands, such as metal-organic frameworks (MOFs) with amine or amide groups (46) or protein amyloid fibers comprising lysines in stacked sheets (47), for CO<sub>2</sub> capture and sequestration. The fact that the arginine residues of the Fe protein trap CO<sub>2</sub> in close proximity to the [Fe<sub>4</sub>S<sub>4</sub>] cluster for further processing may provide a conceptual basis for the future development of MOF- or protein-based FeS catalysts that couple the capture of CO<sub>2</sub> with the recycling of this greenhouse gas into useful chemical commodities.

## 5.5 Acknowledgments

This work was supported by generous funding through a National Science Foundation CAREER grant, award number CHE-1651398 to Dr. Yilin Hu.

I am very grateful to Dr. Martin T. Stiebritz for the DFT calculation results and to Dr. Wonchull Kang for his contributions to structure refinement and analysis. Thank you to Dr. Caleb Hiller, Dr. Chi Chung Lee, and Jasper Liedtke for their efforts on this project. I also appreciate the technical assistance provided by Andrew Ma and Zihao Chen.

I am also grateful to the American Society for Microbiology for publishing these results (18) and allowing me to reuse portions for this chapter.

## 5.6 References

1. Beinert H, Holm RH, Münck E. 1997. Iron-Sulfur Clusters: Nature's Modular, Multipurpose Structures. *Science* 277:653–659.
2. Lill R. 2009. Function and biogenesis of iron–sulphur proteins. 7257. *Nature* 460:831–838.
3. Burgess BK, Lowe DJ. 1996. Mechanism of Molybdenum Nitrogenase. *Chem Rev* 96:2983–3012.
4. Schilter D, Camara JM, Huynh MT, Hammes-Schiffer S, Rauchfuss TB. 2016. Hydrogenase Enzymes and Their Synthetic Models: The Role of Metal Hydrides. *Chem Rev* 116:8693–8749.
5. Mühlenhoff U, Hoffmann B, Richter N, Rietzschel N, Spantgar F, Stehling O, Uzarska MA, Lill R. 2015. Compartmentalization of iron between mitochondria and the cytosol and its regulation. *European Journal of Cell Biology* 94:292–308.
6. Mettert EL, Kiley PJ. 2015. Fe–S proteins that regulate gene expression. *Biochimica et Biophysica Acta (BBA) - Molecular Cell Research* 1853:1284–1293.

7. O'Brien E, Holt ME, Thompson MK, Salay LE, Ehlinger AC, Chazin WJ, Barton JK. 2017. The [4Fe4S] cluster of human DNA primase functions as a redox switch using DNA charge transport. *Science* 355.
8. Rees DC, Akif Tezcan F, Haynes CA, Walton MY, Andrade S, Einsle O, Howard JB. 2005. Structural basis of biological nitrogen fixation. *Philos Trans A Math Phys Eng Sci* 363:971–984; discussion 1035-1040.
9. Georgiadis MM, Komiya H, Chakrabarti P, Woo D, Kornuc JJ, Rees DC. 1992. Crystallographic structure of the nitrogenase iron protein from *Azotobacter vinelandii*. *Science* 257:1653–1659.
10. Rebelein JG, Stiebritz MT, Lee CC, Hu Y. 2017. Activation and reduction of carbon dioxide by nitrogenase iron proteins. *Nat Chem Biol* 13:147–149.
11. Watt GD, Reddy KRN. 1994. Formation of an all ferrous Fe<sub>4</sub>S<sub>4</sub> cluster in the iron protein component of *Azotobacter vinelandii* nitrogenase. *Journal of Inorganic Biochemistry* 53:281–294.
12. Angove HC, Yoo SJ, Burgess BK, Münck E. 1997. Mössbauer and EPR Evidence for an All-Ferrous Fe<sub>4</sub>S<sub>4</sub> Cluster with S = 4 in the Fe Protein of Nitrogenase. *J Am Chem Soc* 119:8730–8731.
13. Musgrave KB, Angove HC, Burgess BK, Hedman B, Hodgson KO. 1998. All-Ferrous Titanium(III) Citrate Reduced Fe Protein of Nitrogenase: An XAS Study of Electronic and Metrical Structure. *J Am Chem Soc* 120:5325–5326.
14. Angove HC, Yoo SJ, Münck E, Burgess BK. 1998. An all-ferrous state of the Fe protein of nitrogenase. Interaction with nucleotides and electron transfer to the MoFe protein. *J Biol Chem* 273:26330–26337.
15. Yoo SJ, Angove HC, Burgess BK, Hendrich MP, Münck E. 1999. Mössbauer and Integer-Spin EPR Studies and Spin-Coupling Analysis of the [4Fe-4S]<sub>0</sub> Cluster of the Fe Protein from *Azotobacter vinelandii* Nitrogenase. *J Am Chem Soc* 121:2534–2545.
16. Stiebritz MT, Hiller CJ, Sickerman NS, Lee CC, Tanifuji K, Ohki Y, Hu Y. 2018. Ambient conversion of CO<sub>2</sub> to hydrocarbons by biogenic and synthetic [Fe<sub>4</sub>S<sub>4</sub>] clusters. *Nature Catalysis* 1:444–451.
17. Hiller CJ, Stiebritz MT, Lee CC, Liedtke J, Hu Y. 2017. Tuning Electron Flux through Nitrogenase with Methanogen Iron Protein Homologues. *Chem Eur J* 23:16152–16156.
18. Rettberg LA, Kang W, Stiebritz MT, Hiller CJ, Lee CC, Liedtke J, Ribbe MW, Hu Y. 2019. Structural Analysis of a Nitrogenase Iron Protein from *Methanosarcina acetivorans*: Implications for CO<sub>2</sub> Capture by a Surface-Exposed [Fe<sub>4</sub>S<sub>4</sub>] Cluster. *mBio* 10.

19. Sickerman NS, Hu Y, Ribbe MW. 2017. Chapter Nine - Nitrogenase Assembly: Strategies and Procedures, p. 261–302. In David, SS (ed.), *Methods in Enzymology*. Academic Press.
20. Winn MD, Ballard CC, Cowtan KD, Dodson EJ, Emsley P, Evans PR, Keegan RM, Krissinel EB, Leslie AGW, McCoy A, McNicholas SJ, Murshudov GN, Pannu NS, Potterton EA, Powell HR, Read RJ, Vagin A, Wilson KS. 2011. Overview of the CCP4 suite and current developments. *Acta Cryst D* 67:235–242.
21. Adams PD, Afonine PV, Bunkóczi G, Chen VB, Davis IW, Echols N, Headd JJ, Hung L-W, Kapral GJ, Grosse-Kunstleve RW, McCoy AJ, Moriarty NW, Oeffner R, Read RJ, Richardson DC, Richardson JS, Terwilliger TC, Zwart PH. 2010. PHENIX: a comprehensive Python-based system for macromolecular structure solution. *Acta Cryst D* 66:213–221.
22. Schlessman JL, Woo D, Joshua-Tor L, Howard JB, Rees DC. 1998. Conformational variability in structures of the nitrogenase iron proteins from *Azotobacter vinelandii* and *Clostridium pasteurianum* 11 Edited by I. A. Wilson. *Journal of Molecular Biology* 280:669–685.
23. Afonine PV, Grosse-Kunstleve RW, Echols N, Headd JJ, Moriarty NW, Mustyakimov M, Terwilliger TC, Urzhumtsev A, Zwart PH, Adams PD. 2012. Towards automated crystallographic structure refinement with phenix.refine. *Acta Cryst D* 68:352–367.
24. Emsley P, Lohkamp B, Scott WG, Cowtan K. 2010. Features and development of Coot. *Acta Crystallogr D Biol Crystallogr* 66:486–501.
25. Davis IW, Leaver-Fay A, Chen VB, Block JN, Kapral GJ, Wang X, Murray LW, Arendall WB, Snoeyink J, Richardson JS, Richardson DC. 2007. MolProbity: all-atom contacts and structure validation for proteins and nucleic acids. *Nucleic Acids Res* 35:W375–W383.
26. The PyMOL Molecular Graphics System, Version 2.0.6, Schrödinger, LLC.
27. Ahlrichs R, Bär M, Häser M, Horn H, Kölmel C. 1989. Electronic structure calculations on workstation computers: The program system turbomole. *Chemical Physics Letters* 162:165–169.
28. O’Boyle NM, Banck M, James CA, Morley C, Vandermeersch T, Hutchison GR. 2011. Open Babel: An open chemical toolbox. *Journal of Cheminformatics* 3:33.
29. Klamt A, Schüürmann G. 1993. COSMO: a new approach to dielectric screening in solvents with explicit expressions for the screening energy and its gradient. *J Chem Soc, Perkin Trans 2* 799–805.
30. Tao J, Perdew JP, Staroverov VN, Scuseria GE. 2003. Climbing the Density Functional Ladder: Nonempirical Meta--Generalized Gradient Approximation Designed for Molecules and Solids. *Phys Rev Lett* 91:146401.

31. Schäfer A, Huber C, Ahlrichs R. 1994. Fully optimized contracted Gaussian basis sets of triple zeta valence quality for atoms Li to Kr. *J Chem Phys* 100:5829–5835.
32. Weigend F, Ahlrichs R. 2005. Balanced basis sets of split valence, triple zeta valence and quadruple zeta valence quality for H to Rn: Design and assessment of accuracy. *Phys Chem Chem Phys* 7:3297–3305.
33. Eichkorn K, Weigend F, Treutler O, Ahlrichs R. 1997. Auxiliary basis sets for main row atoms and transition metals and their use to approximate Coulomb potentials. *Theor Chem Acta* 97:119–124.
34. Weigend F. 2006. Accurate Coulomb-fitting basis sets for H to Rn. *Phys Chem Chem Phys* 8:1057–1065.
35. Noodleman L. 1981. Valence bond description of antiferromagnetic coupling in transition metal dimers. *J Chem Phys* 74:5737–5743.
36. Noodleman L, Post D, Baerends EJ. 1982. Symmetry breaking and ionization from symmetry equivalent inner shells and lone pairs in X $\alpha$  theory. *Chemical Physics* 64:159–166.
37. Noodleman L, Peng CY, Case DA, Mouesca J-M. 1995. Orbital interactions, electron delocalization and spin coupling in iron-sulfur clusters. *Coordination Chemistry Reviews* 144:199–244.
38. Strop P, Takahara PM, Chiu H-J, Angove HC, Burgess BK, Rees DC. 2001. Crystal Structure of the All-Ferrous [4Fe-4S]<sub>0</sub> Form of the Nitrogenase Iron Protein from *Azotobacter vinelandii*. *Biochemistry* 40:651–656.
39. Schindelin H, Kisker C, Schlessman JL, Howard JB, Rees DC. 1997. Structure of ADP·AIF 4 – - stabilized nitrogenase complex and its implications for signal transduction. 6631. *Nature* 387:370–376.
40. Jeoung J-H, Fessler J, Goetzl S, Dobbek H. 2014. Carbon Monoxide. Toxic Gas and Fuel for Anaerobes and Aerobes: Carbon Monoxide Dehydrogenases, p. 37–69. In Kroneck, PMH, Torres, MES (eds.), *The Metal-Driven Biogeochemistry of Gaseous Compounds in the Environment*. Springer Netherlands, Dordrecht.
41. Fessler J, Jeoung J-H, Dobbek H. 2015. How the [NiFe<sub>4</sub>S<sub>4</sub>] Cluster of CO Dehydrogenase Activates CO<sub>2</sub> and NCO<sup>-</sup>. *Angewandte Chemie International Edition* 54:8560–8564.
42. Kung Y, Drennan CL. 2011. A role for nickel–iron cofactors in biological carbon monoxide and carbon dioxide utilization. *Current Opinion in Chemical Biology* 15:276–283.

43. Can M, Armstrong FA, Ragsdale SW. 2014. Structure, function, and mechanism of the nickel metalloenzymes, CO dehydrogenase, and acetyl-CoA synthase. *Chem Rev* 114:4149–4174.
44. Nordlund S, Högbom M. 2013. ADP-ribosylation, a mechanism regulating nitrogenase activity. *The FEBS Journal* 280:3484–3490.
45. Yoo SJ, Angove HC, Burgess BK, Münck E, Peterson J. 1998. Magnetic Circular Dichroism Study of the All-Ferrous [4Fe-4S] Cluster of the Fe-Protein of *Azotobacter vinelandii* Nitrogenase. *J Am Chem Soc* 120:9704–9705.
46. Kazemi S, Safarifard V. 2018. Carbon dioxide capture in MOFs: The effect of ligand functionalization. *Polyhedron* 154:236–251.
47. Li D, Furukawa H, Deng H, Liu C, Yaghi OM, Eisenberg DS. 2014. Designed amyloid fibers as materials for selective carbon dioxide capture. *PNAS* 111:191–196.